Ph.D. Dissertation

Doctor of Engineering (Dr.-Ing.)

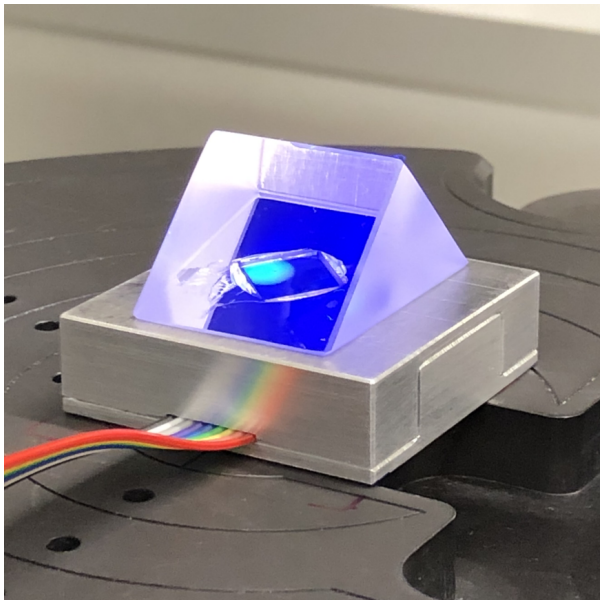

Photoswitchable Plasmon-Exciton Coupling in Photochromic Systems

Bill Brook Shurtleff

October 31, 2020

Kiel, Germany

Bill Brook Shurtleff

Ph.D. Dissertation

submitted to obtain the degree of: Doctor of Engineering (Dr.-Ing.)

Technische Fakultät

Institut für Materialwissenschaft

Christian-Albrechts-Universität zu Kiel (CAU)

Faculty of Engineering

Institute for Materials Science

Kiel University

Kaiserstrasse 2

24143 Kiel

Germany

www.tf.uni-kiel.de

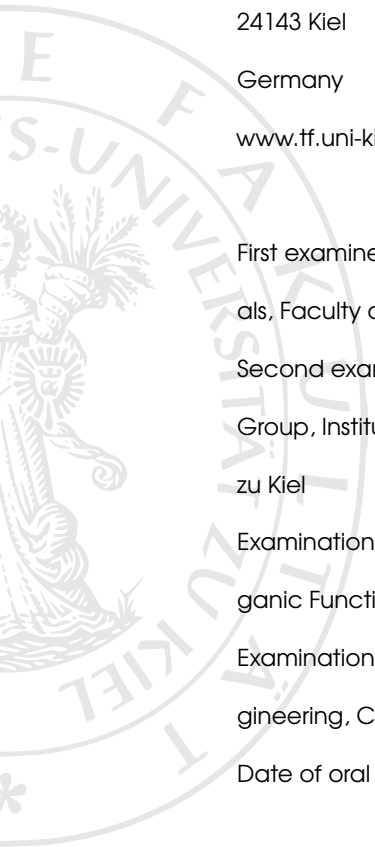

First examiner/Examination Committee member: **Professor Franz Faupel**, Chair for Multicomponent Materials, Faculty of Engineering, Christian-Albrechts-Universität zu Kiel

Second examiner/Examination Committee member: **Professor Michael Bauer**, Chair for Ultrafast Dynamics Group, Institute of Experimental and Applied Physics, Department of Physics, Christian-Albrechts-Universität zu Kiel

Examination Committee member: **University Vice President** and **Professor Eckhard Quandt**, Chair for Inorganic Functional Materials, Faculty of Engineering, Christian-Albrechts-Universität zu Kiel

Examination Committee chair: **Professor Rainer Adelung**, Chair for Functional Nanomaterials, Faculty of Engineering, Christian-Albrechts-Universität zu Kiel

Date of oral defense: **October 29, 2020**

Abstract

The interaction between light and matter is ubiquitous and the phenomenon has been studied by scientists for so long that one could think that science would have all the answers to relevant questions already. Yet how light and matter interact still holds unexplored and interesting territory for science. Of interest to researchers in recent years has been the interaction of light and matter that leads to a coupling of the two in the so-called strong coupling regime. In this dissertation, strong coupling between light and matter will be investigated and made switchable in two different experimental setups. In general, strong coupling between photons and molecular excitons leads to the creation of hybrid modes, different from the original and uncoupled modes, visible as the upper and lower polariton branches of an avoided crossing in the dispersion relation, all measured here with the optical measuring technique of spectroscopic ellipsometry. Results are in very good agreement with electrodynamic modeling. Even in situ measurements of switchable coupling are recorded. The role of the photonic coupling partner will be taken by plasmonic modes, either surface plasmon polaritons excited through the use of a prism in a Kretschmann configuration, or Tamm plasmons, a somewhat newer plasmonic coupling partner gathering interest in research lately and here explored for the first time in the scientific literature with regard to strong coupling with molecular excitons and with regard to being made photoswitchable. The switching is achieved through the excitonic partner, a photochromic molecule that can change conformation, and thus the availability of the excitonic mode, by exposure to UV light. In this way, the light-matter coupling in the sample setups can be switched off and on.

Abstrakt

Die Wechselwirkung zwischen Licht und Materie ist allgegenwärtig und das Phänomen wurde von Wissenschaftlern so lange untersucht, dass man glauben könnte, die Wissenschaft habe bereits alle Antworten auf relevante Fragen. Doch wie Licht und Materie interagieren, ist für die Wissenschaft noch unerforschtes und interessantes Gebiet. Für Forscher war in den letzten Jahren die Wechselwirkung von Licht und Materie von Interesse, die zu einer Kopplung der beiden im sogenannten starken Kopplungsregime führt. In dieser Dissertation wird die starke Kopplung zwischen Licht und Materie untersucht und in zwei verschiedenen Versuchsaufbauten optisch schaltbar gemacht. Im Allgemeinen führt eine starke Kopplung zwischen Photonen und molekularen Exzitonen zur Erzeugung von Hybridmoden, die sich von den ursprünglichen und ungekoppelten Moden unterscheiden und als obere und untere Polaritonenäste einer vermiedenen Kreuzung in der Dispersionsrelation zu sehen sind. Diese werden in dieser Thesis mittels der optischen Messtechnik der spektroskopischen Ellipsometrie vermessen und charakterisiert. Die Ergebnisse stimmen sehr gut mit der elektrodynamischen Modellierung überein. Auch in-situ-Messungen der schaltbaren Kopplung werden aufgezeichnet. Die Rolle des photonischen Kopplungspartners wird von plasmonischen Moden übernommen, entweder von Oberflächenplasmonpolaritonen, die durch die Verwendung eines Prismas in einer Kretschmann-Konfiguration angeregt werden, oder von Tamm-Plasmonen, einem etwas neueren plasmonischen Kopplungspartner, der in letzter Zeit Forschungsinteresse geweckt hat. Hier wird erstmals das Verhalten solcher Plasmonen hinsichtlich starker Kopplung mittels photoschaltbarer molekularer Exzitonen untersucht. Das Umschalten erfolgt durch den exzitonischen Partner, ein photochromes Molekül, das durch Belichtung mit UV-Licht die Konformation und damit die Verfügbarkeit des exzitonis-

chen Modus ändern kann. So kann die Licht-Materie-Kopplung in den Probenaufbauten ein- und ausgeschaltet werden.

Declaration of Authorship

This doctoral dissertation was prepared at the Department of Engineering at Kiel University (Christian-Albrechts-Universität zu Kiel) in fulfillment of the requirements for acquiring the degree of Dr.-Ing in Materials Science and Engineering.

I hereby declare that, apart from my supervisor's guidance, I authored and composed the content and design of this thesis and the respective research independently.

This work complies with the Rules of Good Scientific Practice of the German Research Foundation.

All content and ideas drawn directly or indirectly from external sources are clearly indicated. This thesis has not been published or submitted to any other examining body and all related research items that have been composed and published in peer-review journals are clearly indicated as such.

I declare that no academic degree has been withdrawn from me.

Kiel, Germany, on October 31, 2020

Bill Brook Shurtleff

Contents

List of Figures

List of Tables

CHAPTER 1

Introduction

The fascination with light in the history of science is well documented and associated with such luminaries as Euclid, Newton, Huygens, Young, Maxwell, and Einstein [1]. All manner of experiments have been conducted through the ages to investigate the nature of light and its interaction with matter. From wave to particle theory, school optics to quantum electrodynamic physics, electromagnetic radiation to quantum mechanics, light can be studied in a myriad of ways with numerous and successful theories, but a complete and unified understanding seems to evade us. Even answering questions such as, "Why is the sky blue?" or "Why does the surface of a water puddle with a bit of oil on it shimmer with rainbow colors?" or even "Why are the colors on the wings of some butterflies so brilliant?" can require complex scientific concepts and models to explain. Answering basic and complex questions about light is no trivial matter, but finding the answers is important not only for our understanding of the world but also for potential technologies that arise out of that knowledge. That is why investigations, however nanoscopic, into the interaction of light with matter are still important to this day.

If you were to investigate how light interacts with matter, how would you go about it? If you shine light onto an object, how do you find out how the object is affected, how the light is affected, and how they interacted in the first place? And "to investigate" means to measure something. So, what do you measure? The matter? The light? Both? And then, how do you measure it? And if there is an interaction, can you influence it? Change it? Use it? If so, how?

The light–matter interaction investigated in this PhD thesis deals with how visible light can be used both to excite and probe interactions at an interface between the

electrons of a thin film of a precious metal and a thin layer of polystyrene containing special molecules that are capable of changing shape and color. The charged conduction electrons collectively oscillate in the metal and produce radiation that reaches into the dielectric polystyrene layer, while special molecules of the right shape in the polystyrene can interact with that radiation and, in turn, affect the wave oscillations in the metal layer; they become wedded — a coupling that changes them both.

One of the partners in the couple will be offered by the metal layer, where collective oscillations of the electrons together with their accompanying radiation are called surface plasmon polaritons [2]. Incident light will launch the surface plasmon polaritons, wave oscillations on the fluid-like electronic surface of the metal, whose accompanying electric field will extend into the polystyrene where molecules of spirooxazine have been incorporated, the other partner of the couple. These shape-shiftable molecules can interact with the radiation, but only if the molecules have been switched from the wrong shape to the right shape, a change that also takes the molecules from transparent to colorful. A type of molecule called a spirooxazine is just such a shape-shifting and color-changing chemical species [3], [4]. A form of spirooxazine can be used, for example, in color-changing eyeglasses [5] whose lenses darken when the wearer goes outside into bright sunlight, a behavior caused by the energetic, invisible ultraviolet light from the sun striking the molecules. Similarly, the type of spirooxazines used here (SPO) will change color when exposed to ultraviolet light [6], and with that, the molecules change not only their color and shape but also how they interact with the waves of radiation from the adjacent surface plasmon polaritons. In short, white light is shined on the metal and some wavelengths of color are absorbed, which launches the electron waves across the metal; UV light changes the shape of the spirooxazine molecules and turns them blue, which means they absorb yellow light [1]; the electron wave radiation and the shape-changed molecules couple to form new hybrid modes of oscillation. And although as separate entities the plasmons and the molecules absorb basically one color of light, once the two are coupled, two colors of light are now absorbed, but the two colors are different from each other and different from the colors originally absorbed by the two

partners before they coupled.

On top of it all, the new aspect presented here is that the coupling between the two partners can be turned on and off, like a light switch. As part of the Collaborative Research Center 677 “Function by Switching”, the research presented here is a continuation of previous research in the project and group involving the use of photoswitching for such aspects as photoresponsive optical transparency of conductive metal [7], a photoswitchable superabsorber [6], and evidence of coherent radiation of dipole antennas [8], as well as related investigations such as a perfect absorber [9] and a plasmonic metamaterial antireflection coating [10].

To be more scientifically concrete: control of coupling is investigated between surface plasmon polaritons and excitons of switched photochromic molecules of spirooxazine. Since coupling [11] leads to the production of and Rabi splitting of hybrid modes, to control the coupling is to control the concomitant avoided crossing of the polaritonic branches of the optical system’s dispersion relation. Not only the concentration of spirooxazine and the intensity of UV light determine the degree of coupling, but the duration of UV exposure offers a degree of freedom for such control because it changes the concentration of excitons dynamically. Here, the dynamic splitting of hybrid modes is made visible in video made possible with in situ spectroscopic ellipsometry techniques.

The geometry of the optical systems used to investigate such coupling involves, on the one hand, the classical, if somewhat bulky, Kretschmann setup [2] involving a glass prism, and on the other hand, a dielectric mirror in a setup employing the somewhat recently discovered Tamm plasmons as the surface waves [12], [13].

The samples for the Kretschmann setup will be made on pieces of quartz glass by sputter depositing [14] a thin film layer of either silver or gold to a depth of only about 50 nm (as thick as about 150 atoms lined up in a row). Then, the metal will be covered via spin coating [15] to a thickness of about 35 nm with a layer of polystyrene (PS) that is spiked with the SPO molecules (hereafter, PS-SPO). For the Tamm setup, the PS-SPO layer will be sandwiched between two types of mirrors: a thin film of sputtered-on silver and a self-made distributed Bragg reflector, a type of non-metallic, multilayered,

all-ceramic mirror produced in a vacuum chamber with RF magnetron sputtering [14].

To the author's knowledge, this is the first time that the off/on control of splitting enabled with photoswitchable molecules has been shown in a Kretschmann setup and the dynamic splitting made live in the form of a video. Also for the first time, coupling between Tamm plasmon polaritons and molecular excitons is shown, and on top made switchable, opening the way for future studies about controlling coupling in such a multilayered, thin filmed, compact, straightforward system.

Starting with this work, investigations into the prospects of manipulating plasmon-exciton coupling at the molecular level can develop further with the ability to transition coupling off and on. The hoped-for future applications of such disparate technologies as optical amplification [11], [16] and chemical reaction manipulation [17] gain a new lever of control: a switch. If you can control the coupling on the nanoscale to such a degree and on demand, new technologies will emerge that take advantage of that control. Switch on, switch off.

For reading the thesis, the following general outline should help the reader. The first section will cover theoretical aspects about light, the photoswitchable molecules of SPO, Bragg mirrors, and plasmons (both surface plasmon polaritons and Tamm plasmon polaritons) and will lead to a general understanding of coupling, the basic concept of the transfer matrix method used in computer simulations, and the instrumental technique used for the experiments: spectroscopic ellipsometry. Next, the actual experiments are described, including sample preparation and the setup of the two optical systems for the investigations. The results follow, giving all the data and gathered information from the simulations and experiments, together with the discussion of those results. At the end, the findings of the thesis are recapped with a summary, and suggestions for the future are given in an outlook.

CHAPTER 2

Theory

To begin the discussion of the theoretical understanding needed for these studies, a brief overview is presented here about the necessary elements and how they interrelate.

First, light–matter interactions and their mathematical descriptions will be described. The Fresnel equations [18], [19] tell one how light's amplitude and phase are affected by interaction with a material. The Fresnel equations depend on the dispersion relations of the materials at an interface. Applying the equations to multilayered systems of different materials permits the calculation of the entire optical response, i.e., the system's dispersion relation. The transfer matrix method [19]–[22] combines the Fresnel equations of an optical system to compute an optical response based on the theory of electromagnetic radiation. With the dispersion relations of standalone optical systems, these systems are combined into different possible arrangements that permit the interaction of oscillatory modes. This interaction, known as coupling [11], is at the heart of all optics where light and matter interact.

The understanding and tailoring of this interaction is of central importance. For this, different oscillatory modes are introduced and range from excitons [23] to plasmons [2] to standing waves in periodic 1-D photonic crystals [24]. A special type of mode, called a Tamm plasmon [12], [13], will also be introduced and explained. Additionally, the mechanism of the interactions of such modes and the applicable parameters will be introduced, where as a result of such interactions so-called hybrid modes [11] form. At the core of this study is the optical control of hybrid modes via the off/on switching of the conformation of chromophoric molecules [3]–[5] that enable one to tailor the coupling strength.

2.1 Fresnel Equations

The Fresnel equations [18], adapted here from Fujiwara's textbook on spectroscopic ellipsometry, describe light's change in amplitude and phase at the interface of two materials, i.e., what is transmitted and reflected depending on the polarization of incident light. The corresponding quantities are referred to as amplitude coefficients for each type of polarization (i.e., p- and s-polarization). The equations are given by

$$r_s = \left(\frac{E_{rs}}{E_{is}}\right) = \frac{n_i \cos(\theta_i) - n_t \cos(\theta_t)}{n_i \cos(\theta_i) + n_t \cos(\theta_t)} \tag{2.1}$$

$$r_p = \left(\frac{E_{rp}}{E_{ip}}\right) = \frac{n_t \cos(\theta_i) - n_i \cos(\theta_t)}{n_t \cos(\theta_i) + n_i \cos(\theta_t)} \tag{2.2}$$

$$t_s = \left(\frac{E_{ts}}{E_{is}}\right) = \frac{2n_i \cos(\theta_i)}{n_i \cos(\theta_i) + n_t \cos(\theta_t)} \tag{2.3}$$

$$t_p = \left(\frac{E_{tp}}{E_{ip}}\right) = \frac{2n_i \cos(\theta_i)}{n_t \cos(\theta_i) + n_i \cos(\theta_t)} \tag{2.4}$$

where r is the reflection amplitude coefficient and t is the transmission amplitude coefficient, both with subscripts s or p representing the polarization of the light; E_r is the electric field in the reflected beam, E_i is the electric field in the incident beam, and E_t the transmission beam; θ is the angle of incidence (AOI) as measured from the surface normal and the index of refraction is n, both with subscripts t and i for the transmission material (the layer to be investigated) and the incidence material, e.g., air above the sample. Thus, the Fresnel equations allow the determination of the ratio of the electric field vector on reflection or transmission to the electric field vector of incident light. From the amplitude coefficients, the total reflected intensity R and transmission intensity T can be calculated as follows:

$$R_s = \frac{I_{rs}}{I_{is}} = \left|\frac{E_{rs}}{E_{is}}\right|^2 \tag{2.5}$$

$$R_p = \frac{I_{rp}}{I_{ip}} = \left|\frac{E_{rp}}{E_{ip}}\right|^2 \tag{2.6}$$

$$T_s = \frac{I_{ts}\cos(\theta_t)}{I_{is}\cos(\theta_i)} = \left|\frac{E_{ts}}{E_{is}}\right|^2 \left(\frac{n_t\cos(\theta_t)}{n_i\cos(\theta_i)}\right) \tag{2.7}$$

$$T_p = \frac{I_{tp}\cos(\theta_t)}{I_{ip}\cos(\theta_i)} = \left|\frac{E_{tp}}{E_{ip}}\right|^2 \left(\frac{n_t\cos(\theta_t)}{n_i\cos(\theta_i)}\right) \tag{2.8}$$

where I_r is the reflected light intensity and I_t is the transmitted light intensity, and again subscripts representing p- and s-polarized light. It must be noted that the Fresnel amplitude coefficients r and t hold true even with n replaced by the complex equivalent $\tilde{n}$, to be discussed next.

2.2 Refractive Index

The complex refractive index $\tilde{n}$ [18], [25] is a very commonly used dimensionless quantity that describes the propagation of light in a medium exhibiting absorption. The complex index of refraction, also adapted from Fujiwara's book, for a material is given by:

$$\tilde{n} = n + i\kappa \tag{2.9}$$

where n is commonly referred to as the index of refraction and κ is most usually called the extinction coefficient, although other names exist. κ is related to absorption, which can be seen in Beer's law, which describes intensity attenuation as a function of distance for absorbing materials

$$I(z) = I_0\exp(-\alpha z) \tag{2.10}$$

where α is commonly called the absorption coefficient and modifies the exponential decay of the intensity with increasing z distance traveled through the material (I_0 is the optical intensity at $z = 0$). The imaginary part of the complex index of refraction is directly

proportional to the absorption coefficient via the relation:

$$\alpha = \frac{2\omega}{c}\kappa = \frac{4\pi}{\lambda}\kappa \tag{2.11}$$

where ω is the angular frequency of light, c the speed of light in a vacuum, and λ the vacuum wavelength of light.

2.3 Transfer Matrix Method

The combination of the Fresnel equations as explained above to multilayered systems involving many interfaces can be generalized to a method commonly known as the transfer matrix method [19]–[22]. This method allows for the computation of a system's optical response, i.e., its dispersion relation. All simulations performed in the pursuit of these studies were programmed[1] and conducted in MATLAB. The transfer matrix method gives information on the changes in the propagation of the electric field (or magnetic field) of light in the sample. For this, the method requires thicknesses and refraction indices of each material layer.

The interaction of light with a stack of thin film layers needs to be described mathematically to make predictions of the effect samples have on light. Essentially, propagation through a layer and transmission through an interface of the electric field vector of incident plane wave light on a thin film of a material will be described and includes phase change and attenuation of the light. A standard method for the description of the electric field vector transferred through the film is called the transfer matrix method [19]–[22]. In brief, the electric field vector incident at some angle at the top surface of a layer is transformed through matrix multiplication into the vector exiting at the bottom surface. The matrix transformation maintains the vector magnitude for non-absorbing materials or attenuates it for absorbing materials, and also changes the phase of the

[1] The MATLAB simulations conducted for this thesis were all based on code to a great extent written by a colleague, Ron-Marco Friedrich, whose continued help in teaching the author the techniques and skills involved in MATLAB coding is very greatly appreciated.

vector to some arbitrary angle depending on the thickness and optical properties of the layer. From there, the Fresnel equations are used to determine the coefficients of reflection r and transmission t, as discussed above. Again, r and t can be used in turn to calculate the intensities of reflection R and transmission T, which describe the resultant light intensities after interaction with the layer. Input parameters for the transfer matrix method are the geometry of the stack of layers and the optical response of the individual materials (i.e., complex index of refraction) in the stack. With this, any sort of layered optical system can be simulated. To account for the use of prisms in the upcoming Kretschmann configuration [2], only a change in the AOI and the initial refractive index have to be included.

It must be said that the magnetic field vector could just as easily be used for a description of the propagation of light, but since the goal is later to discuss the relative permittivity, and from that the index of refraction, the electric field with its greater interaction is the natural and logical choice, especially since the materials used here are non-magnetic.

2.4 Ellipsometry

Investigations of the optical responses of optical systems can be performed using spectroscopic ellipsometry [18]. Here, the sample is illuminated using polarized light and the reflected light is analyzed with respect to changes in the intensity of the s- and p-polarizations. The measured intensities of light for varying angles of incidence and wavelengths denote the dispersion relation of the optical system at hand. Furthermore, in situ analysis of optical behavior enables the characterization of time dependent phenomena.

Spectroscopic ellipsometry has several advantages as a measurement technique. First, measurements are non-invasive; the only probe used to interact with the sample is a beam of light, and a fairly dim beam of light at that. In theory, the sample is not changed or damaged during the measurement and can be probed again and again without

measurable change in the optical constants. Second, the phase information is highly sensitive to film thicknesses even less than 10 nm. In addition, no reference beam(s) are required and measurements are relatively quick and easy to perform.

In Figure 2.1 the schematic setup [26] of an ellipsometer in reflection mode is shown. The source contains two lamps that emit light across the spectral range of the instrument (which is also the reason this type of ellipsometry is referred to as "spectroscopic" ellipsometry [18]). From the source, the emitted electromagnetic radiation is randomly polarized. The light then passes through the polarizer, which polarizes the light beam linearly. The linearly polarized light can be considered to consist of a linear combination of two orthogonal electric field vectors, parallel and perpendicular to the plane of incidence. From there, the light passes on to the compensator, which retards one of the orthogonal electric field vectors by $\pi/2$ with respect to the other. The result is circularly polarized light. The circularly polarized light of all wavelengths in the spectral region of the source strikes the sample at the desired AOI, θ_i, and becomes elliptically polarized,

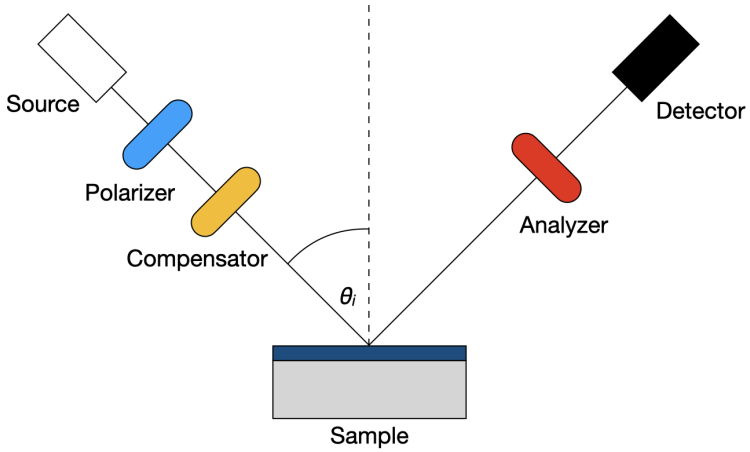

Figure 2.1: Schematic diagram of the essential parts of the spectroscopic ellipsometer used: a light source, a linear polarizer, a compensator to produce circularly polarized light which strikes the sample in reflection mode at the angle of incidence θ_i. On reflection, the polarization state of the now elliptically polarized light is determined in the analyzer, and the light is finally detected with a CCD.

hence the technique's name. The subsequent analyzer in the reflected beam determines the polarization state of the light after having interacted with the sample, and the four-quadrant detector is used for aligning the beam during setup and measuring the reflected beam intensity.

The measured quantities in spectroscopic ellipsometry are Ψ and Δ [18]. They are related with respect to the p- and s-polarization of light amplitude coefficients by

$$\tan(\Psi)e^{i\Delta} = \frac{r_p}{r_s} \tag{2.12}$$

where Ψ represents the amplitude ratio and Δ represents the phase difference between p- and s-polarized light. Because the measurement only involves a ratio of these complex coefficients, calibration of the instrument is not necessary, which makes it a very accurate and reliable measurement technique. Since Ψ and Δ are related to these Fresnel coefficients, the data can be used for estimating the optical constants and other parameters, such as the thickness. To achieve this, non-linear fitting procedures have to be employed with the Levenberg-Marquardt algorithm [26] to obtain a good parameter estimate from an appropriate model. Here, the optical constants and thicknesses of sample layers can be determined through software modeling. Since optical constants, such as n and κ, cannot be directly measured in spectroscopic ellipsometry, an inverse problem must be solved by estimating these parameters. To determine the causes of polarization change in the sample which led to the measured data, a model of the sample must be created.

In this thesis, the CompleteEASE software was used together with the spectroscopic ellipsometer instrument, both from J.A. Woollam Co. [26]. There are many models for the description of the refractive index of a medium. Most non-absorbing dielectrics can directly be modeled with the Cauchy model in the visual region of the spectrum. Cauchy's equation [20], [25], [27], shown in Equation 2.13, is used to model the index of refraction of the sample over the transparent region. In this model, the imaginary part,

κ, is assumed to be 0 over the region of interest.

$$n(\lambda) = A + \frac{B}{\lambda^2} + \frac{C}{\lambda^4} \tag{2.13}$$

The coefficients A, B and C are material constants that are determined in a minimized mean squared error (MSE) calculation [26] in the software during a fitting process. To describe an arbitrary refractive index of a medium, numerical fitting is employed with B-splines that fulfill the Kramers-Kronig relations [25] for physically possible systems (real systems must adhere to the two bidirectional equations that relate the real and imaginary parts of the complex index of refraction). Because a model is needed to fit the data, one needs to gauge the appropriateness of the fit with the MSE.

The MSE is used to evaluate the difference between data obtained experimentally and data generated from a model. If significant deviation from the experimental data is present and thus the MSE is large, another model may need to be chosen or the parameters adjusted if an incorrect local minimum in the fitting procedure is found. Because the fitting procedure is non-linear, there are many local minima, and so an initial good estimate of the parameters is required to find the global minimum. If the MSE is low enough and the visual fit is acceptable, the obtained parameters may be trusted. In fact, the visual comparison between Ψ and Δ data and the model fit is of foremost importance when modeling, followed in importance by the MSE value, because the visual fit may be excellent in the region of interest whereas the MSE value is calculated for the entire wavelength range in view.

Overall, spectroscopic ellipsometry is a versatile and highly sensitive tool for the measurement and description of optical systems. With the obtained data, many important parameters of the optical system can be determined.

2.5 Resonance in Molecular and Optical Systems

In the following section, different types of resonance will be outlined in molecular and optical systems. Included are electronic transitions in molecules (excitons [23], [28]), collective oscillations of electrons at metal-dielectric interfaces (surface plasmon polaritons [2]), standing waves in dielectric periodic systems (Bragg modes [24]) and their alteration from the interaction with metallic mirrors (Tamm plasmon polaritons [12], [13]).

2.5.1 Excitons

The term exciton is often used to describe the hydrogen-like pairing of a hole and an electron in a semiconductor [23]. However, the term exciton can also be used to describe the excited state of an electron in a molecule where an electron is excited from the HOMO level to the LUMO level [28]. An electron is promoted to the LUMO and a corresponding hole with the same spatial frequency is left in the HOMO. The electron and hole are bound in the molecule for a Frenkel exciton, and the energy for electron excitation is a discrete amount.

2.5.2 Surface Plasmon Polaritons

A surface plasmon polariton [2] is a quantized quasiparticle formed at the interface of a conducting metal and an adjacent dielectric, and as such is a type of surface wave. Free electrons in a metal can collectively exhibit plasma oscillations at the interface with quasi-momentum and energy described in a dispersion relation, with quanta of such oscillations termed plasmons. Such collective oscillations propagate at the interface with fluctuations of electron charge density at the metal surface. These charges give rise to electromagnetic fields with both longitudinal and transversal components in the adjacent dielectric. The

amplitude of the electric field decays exponentially with increasing distance from the metal-dielectric interface: it is an evanescent wave that extends into the dielectric layer [29]. This fact makes surface plasmons very sensitive to changes in the refractive index at the interface [30].

To excite surface plasmons [2], incident light can be used under the right conditions, as will be explained in the following. The surface plasmon's transversal electric field component couples with the electric field of incident electromagnetic radiation and results in a system of a coupled plasmon and (polarization-)photon, called a surface plasmon polariton (SPP). It is a "polarization-photon" because for the incident electromagnetic radiation, only p-polarized light has a component normal to the interface and an in-plane component in the direction of SPP propagation which can couple; s-polarized light cannot couple.

For coupling to take place, only light of the right momentum can transfer energy and excite the plasmon [2]. For this, the light line of the dispersion relation must be made to intersect with the dispersion curve of the SPPs of the metal–dielectric interface (Figure 2.2). The SPP's dispersion curve (solid blue line) is below the air light line (also referred to as "outside the light cone", the dashed blue line), thus there is no intersection between the two, and light incident from air onto the metal surface cannot couple into surface plasmons. However, if the light is incident from glass and the AOI is appropriate, the wavelength of the light is reduced, i.e., the in-plane momentum vector (k vector) is lengthened, and brings the glass light line (red dashed line) into intersection with the dispersion curve of the SPP (solid blue line) of the metal–dielectric interface: coupling between the altered incident light and the SPP modes can occur and launch surface plasmons.

Because of the localization of the surface plasmon polaritons at the metal–dielectric interface, changes of the dielectric index of refraction will change the surface plasmons' optical response [30]. Therefore, highly sensitive measurements of changes of the dielectric medium at the interface are possible [30].

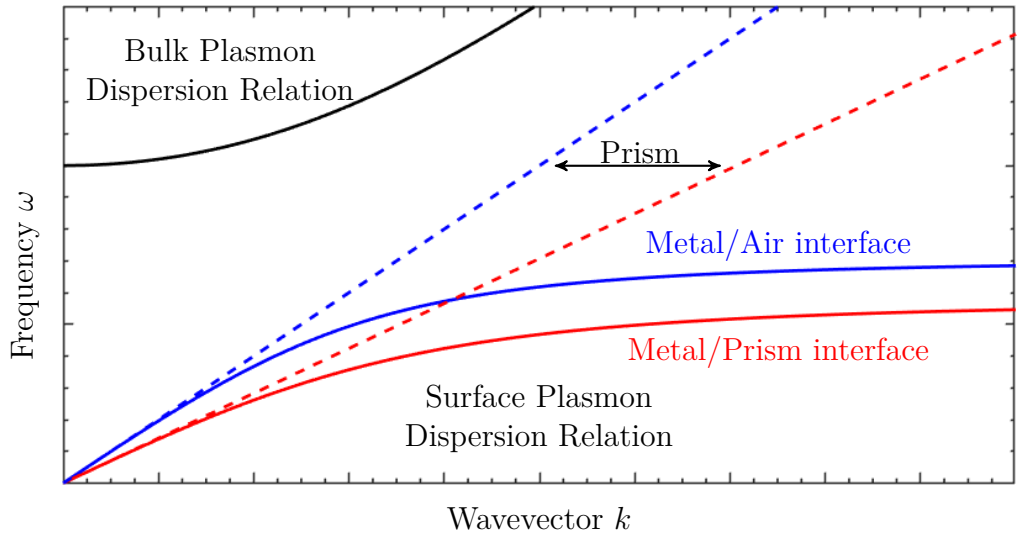

Figure 2.2: Schematic of dispersion relations for SPPs. Each dashed line indicates a light line in a medium (blue for air, red for glass) and the solid lines represent the interfaces that are used in the Kretschmann configuration for the excitation of SPPs. A prism is needed to excite SPPs by matching the momentum to allow energy transfer between the light in prism glass and the metal–air interface SPPs. From MATLAB work for preparation of thesis.

2.5.2.1 Exciting Surface Plasmon Polaritons with the use of Prisms

In the Kretschmann (a.k.a Kretschmann-Raether [31]) configuration, a prism is employed to change the incident light's wavelength (see Figure 3.3) and thus make launching SPPs on the metal possible [2]. Total internal reflection of light impinging at an angle greater than the critical angle of total internal reflection at the base of the prism-plus-metal system results in the excitation of SPPs at the metal–dielectric interface [32]. An evanescent field, generated by the oscillation of charges in the metal, extends into the dielectric layer beyond the physical limits of the metal layer, whose thickness is therefore critical [33]: too thick, and bulk characteristics of the metal will reflect light and allow insufficient evanescent field to reach into the dielectric, thereby limiting or precluding SPPs; too thin, and the mean free path of the oscillating electrons in the metal will be overly impeded, and extra damping will result. To find the proper critical thickness of the metal layer, computer simulations are more than beneficial, they are essential

for optimum results. In these studies, the simulations predict the necessary metal layer thickness to be on the order of a few tens of nanometers; thus, thin film deposition techniques are required and will be described. With a suitable incident material and angle, light of the right frequency will be absorbed and launch SPPs on the metal surface. By measuring the change in light intensity for each frequency reflected from the sample into a detector, absorption of light by the sample can be interpreted as those incident wavelengths that resulted in the launch of SPPs [34].

In addition, a prism efficiently transfers external light from air into glass (and towards the glass–metal interface) by minimizing reflections. According to the Fresnel equations, reflection is weakest from the glass surface when external light strikes the glass face at nearly normal angles, which is true for the prism in this case. In addition, the beam is not spread or refracted appreciably when aberrations in the prism are kept to a minimum by purchasing a high quality prism, thereby ensuring beam integrity.

The next type of resonance in an optical system to be discussed is for standing waves in dielectric periodic systems: Bragg modes.

2.5.3 Bragg Modes

Bragg modes [24] arise from the behavior of light in photonic crystals (i.e., dielectric periodic structures). A common photonic crystal used in optics is a one-dimensional distributed Bragg reflector (DBR) [35], [36], also known as a dielectric mirror: a stack of layers that can be used to reflect light of a certain range of wavelengths at certain angles of incidence (a schematic that includes a DBR is depicted in Figure 2.7). All DBRs in this thesis are 1-D. There can exist a range of wavelengths where light is reflected nearly 100% and which is referred to as the stopband or optical bandgap of the optical system (see Figure 2.3).

The formation of an optical bandgap in a DBR can be compared to the nearly free electron model in solid state physics [37]. In that model, the introduction of the periodic potential of the atomic cores of the crystal leads to the occurrence of standing waves

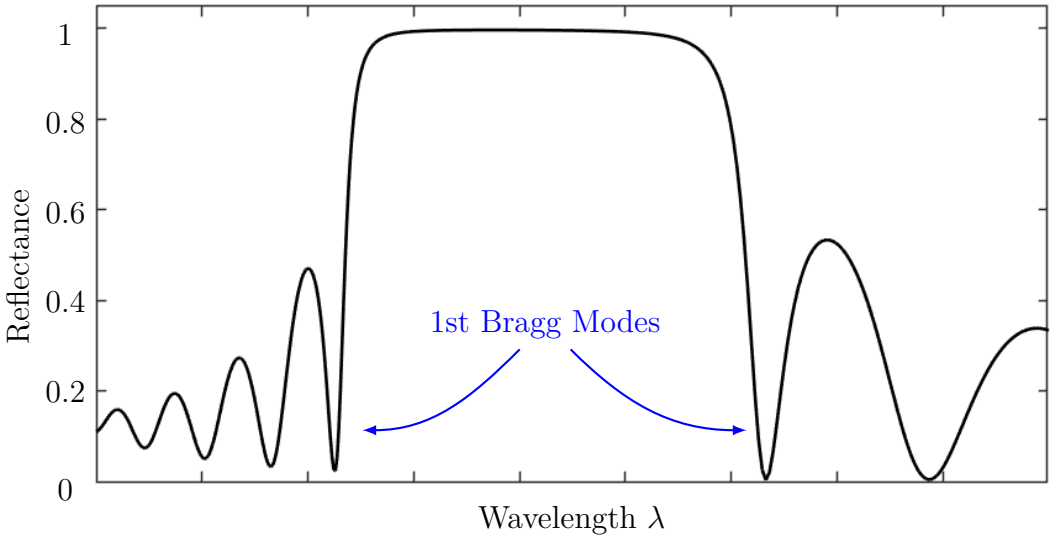

Figure 2.3: Stopband or optical bandgap for a distributed Bragg reflector. The band edge is characterized by optical modes, referred to as Bragg modes. From MATLAB work for preparation of thesis.

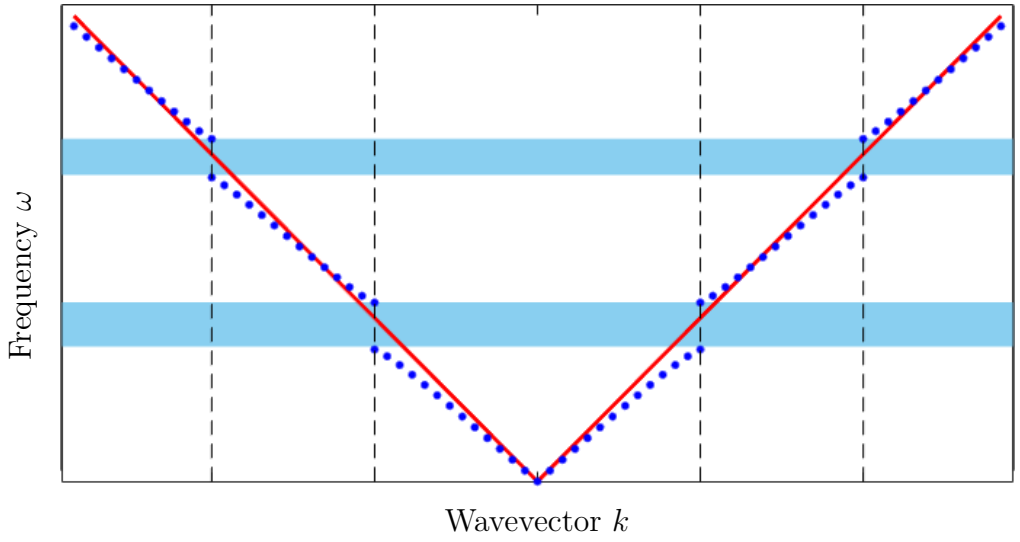

Figure 2.4: Optical dispersion relation. The blue-colored bandgaps form due to the periodicity of the Bragg stack. The red line indicates the dispersion relation of the light line. The blue dots indicate the optical modes in the DBR and are the Bragg modes, which are the standing waves of the system. The first Bragg modes are those just above and below a bandgap. From MATLAB work for preparation of thesis.

at the Brillouin zone boundary, which implies the formation of a bandgap with respect to the energy in the dispersion relation. The same happens for a photonic crystal: the periodicity of the stack leads to standing waves at the stopband edge (see Figure 2.4 for schematic dispersion relation and description). Such standing waves are referred to as Bragg modes. They are composed of a modulation of a standing wave and the periodicity of the indices of the stack, as shown in Figure 2.5. These modes are transmitted through the stack as can be seen in Figure 2.6, where a radiative mode exists at the bottom of the stack as a loss channel. The wavelengths of the optical bandgap have no supported optical modes in the system, which implies the reflection of these wavelengths from the stack. The position of the stopband is dependent on the periodicity of the stack and the layer thicknesses as well as their corresponding refractive indices. The greater the difference between the indices of refraction, the greater the width of the stopband and the greater the reflectance. Stacking more bilayers increases the reflectance of the stopband.

As seen in the Figure 2.3, the wavelengths reflected from a DBR can reach very nearly 100% reflection [24] for those incident wavelengths at the AOI if there are enough bilayers repeated in the stack. Fringes appear to both sides of the stopband with successively decreasing maximum reflectance and lowest reflectance points that were introduced as the Bragg modes.

Another interesting analogy could be drawn here to solid state physics [37] and the formation of the bandgap in the nearly free electron model. In that model near the Brillouin zone boundary, two standing waves form: one wave with maxima at the positions of the positive atomic cores has lower energy, and the other wave with maxima between the positions of the positive atomic cores has higher energy. Similarly here, two standing waves are formed: one wave with maxima in the higher index of refraction layers has lower energy (corresponding to the first Bragg mode at the greater wavelength side of the bandgap), and the other wave with maxima in the lower index of refraction layers has higher energy (first Bragg mode at the lower wavelength side of the bandgap).

The final type of resonance in an optical system to be described will build on the

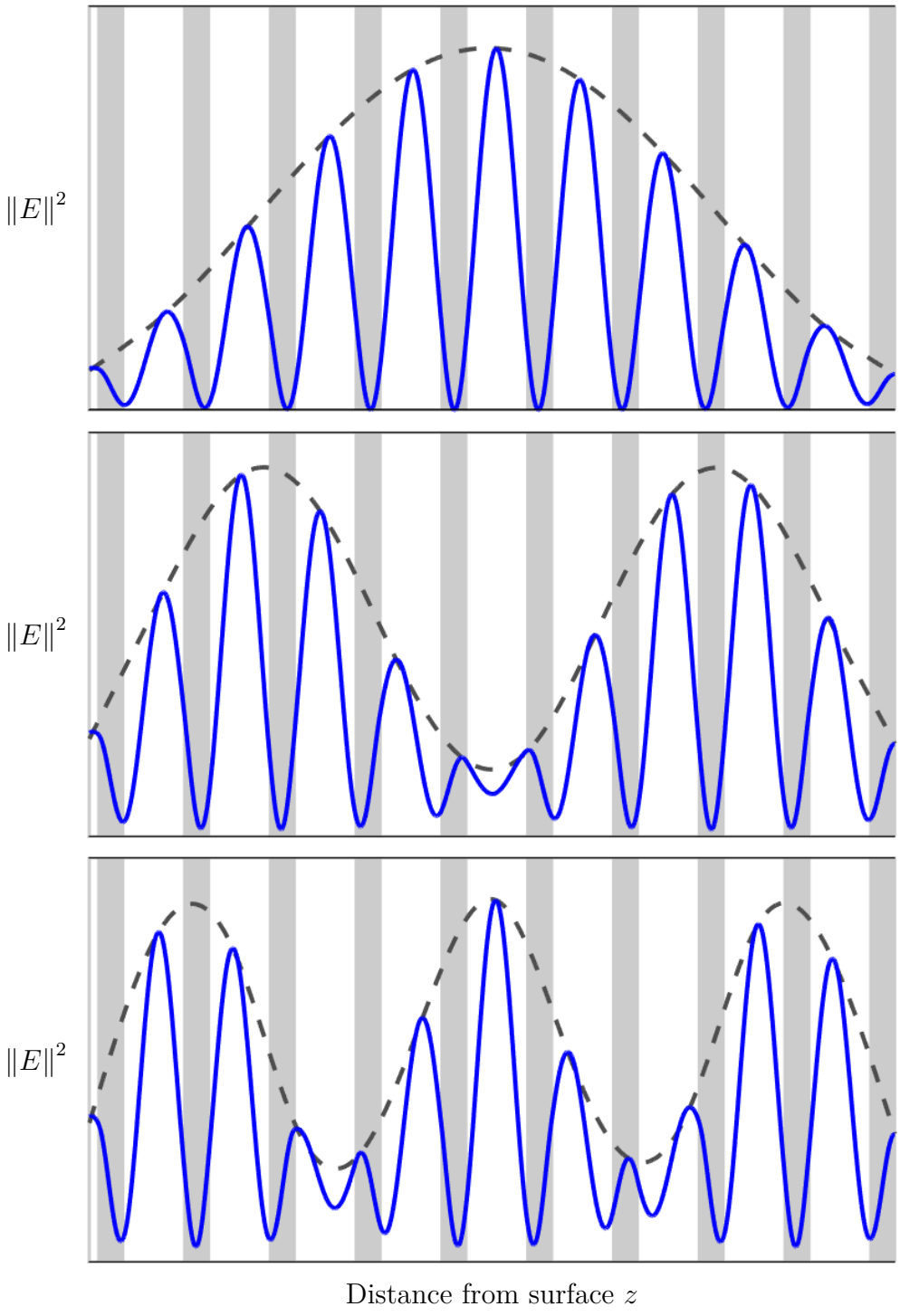

Figure 2.5: Electric field intensity distributions for the first three Bragg modes (from top to bottom, first to third) in a DBR (light grey layers are higher index material). The envelopes are shown to indicate the standing waves in the system. The spatial frequency of the blue curves corresponds to the periodicity of the indices of the system. From MATLAB work for preparation of thesis.

previous material about Bragg modes; specifically, the alteration of such from interaction with metallic mirrors.

2.5.4 Tamm Plasmon Polaritons

Kavokin, et al. [39] predicted in 2005 the existence of what they called Optical Tamm States: lossless interface modes of light formed at the interface between two photonic structures with different periodicities and overlapping band gaps. In effect, light of certain wavelengths is trapped between two dielectric mirrors. Kaliteevski, et al. [40] in 2007 expanded on this idea by replacing one dielectric mirror with a different type of mirror, a metal thin film. Electromagnetic modes are still confined: as usual, confinement at the metal is a result of its negative relative permittivity, i.e., high reflectance, and confinement by the dielectric multilayered stack is due to a photonic stopband. Again, certain wavelengths of light are confined between the two components, however now the light has a zero in-plane wave vector, i.e., it forms a standing wave between the reflectors. Similar to SPPs, the term Tamm plasmons refers to electron oscillations in the metal layer, whereas Tamm plasmon polaritons refers to the coupled system of plasmons and photons (the terms are often used interchangeably in the literature). In contrast to SPPs however, the dispersion relation for Tamm plasmon polaritons is inside the light cone [12] and therefore requires no momentum coupler such as a prism. In addition, whereas SPPs can only be launched by p-polarized light, both p- and s-polarized light can excite Tamm plasmons, albeit with very little difference in their respective dispersion relations [12]. The term “Tamm plasmon” was coined [40] in analogy with Tamm electronic surface states in a semiconductor where the periodicity of the crystal is disrupted by the surface; in Tamm plasmons, the periodicity of the DBR is likewise interrupted by the surface and leads to a ”surface state” of reflected light.

When a thin spacer layer [38], also known as a cavity layer, is introduced between the metal thin film and the dielectric mirror in a Tamm plasmon stack setup (see Figure 2.7), the system can still confine light, albeit only light whose wavelength matches the

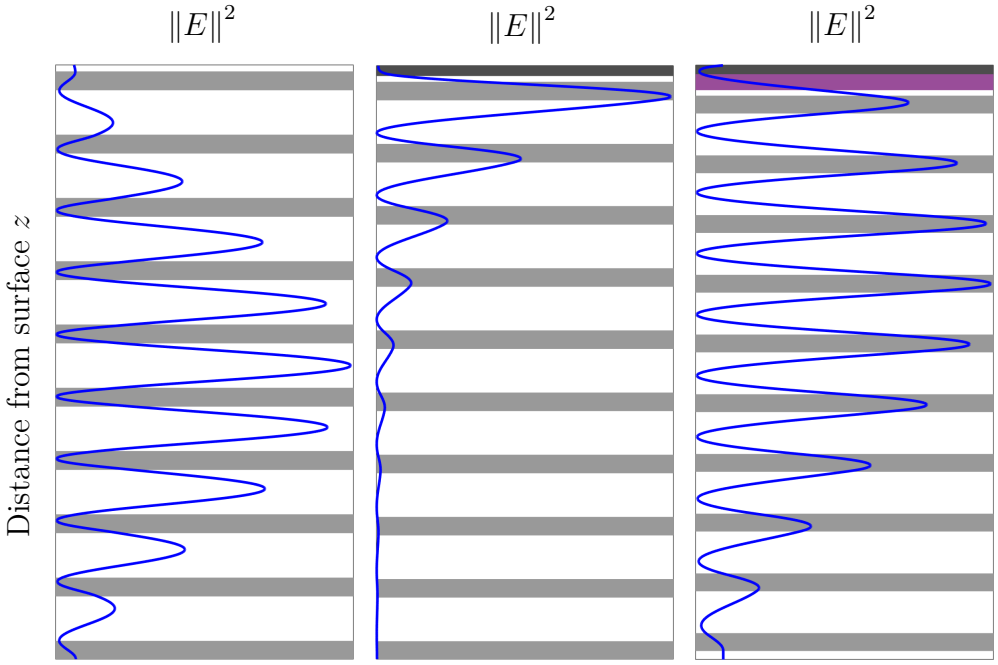

Figure 2.6: Electric field intensity distributions (z-axis) for the optical modes [38] in three different optical systems where incident light strikes from above. **Left**: first Bragg mode in a DBR (bilayers of lower index white and higher index grey); **middle**: Tamm plasmon mode in stack of thin film metal layer (dark grey at top) atop a DBR; **right**: Tamm plasmon in stack of a thin film metal layer (dark grey) on a spacer layer (magenta) atop a DBR. Note: radiative modes as loss channels are possible in both Bragg modes (left) and Tamm setup with spacer layer (right), i.e., light is transmitted out the bottom. From MATLAB work for preparation of thesis.

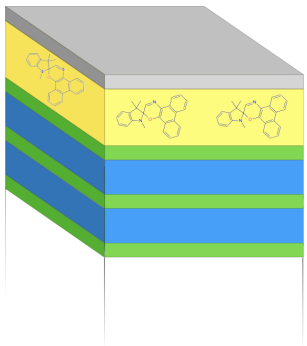

Figure 2.7: Tamm setup consisting of a metal layer (grey) on a spacer layer (yellow) containing excitonic material (molecular skeletal formulas) atop a DBR (green and blue, high index and low index of refraction, respectively).

boundary conditions. This is similar to a Fabry-Pérot interferometer [25], with the difference being that one mirror is a DBR.

A comparison of Bragg modes, Tamm plasmon modes, and modes of Tamm plasmons together with a spacer layer are shown schematically in Figure 2.6. If the cavity layer contains molecular resonators, i.e., excitons, whose excitation energy coincides with the energy of light trapped between the metal and dielectric mirror, coupling could take place between the exciton and the Tamm plasmon polaritons. This will be further discussed in the section below on current literature of Tamm plasmon research.

2.6 Coupling in Optical Systems

The behavior of resonators [11] in optical and molecular systems are similar with respect to the following main concepts: the resonators are able to store energy and they show a certain profile in their frequency response; that is, there exists a certain amplitude and phase behavior with respect to the wavelength (or k vector). As a result of changes in phase and amplitude of these resonators, it is possible for these systems to exchange energy with each other. One mode can give energy to the other and vice versa - coupling takes place. But in order for this energy exchange to happen, the phase relationship between the systems must match, otherwise destructive interference takes place. The result of coupling is the formation of new modes, called hybrid modes, in which this energy exchange takes place.

The behavior of coupling is often described by two coupled oscillators [41], [42] and can be shown in the following system of coupled differential equations

$$ae^{iwt} = \ddot{x}_1 + \gamma_1\dot{x}_1 + \omega_1^2 x_1 + \Omega x_2 \tag{2.14}$$

$$0 = \ddot{x}_2 + \gamma_2\dot{x}_2 + \omega_2^2 x_2 + \Omega x_1 \tag{2.15}$$

where $\ddot{x}_i$ is the inertial term, $\gamma_i\dot{x}_i$ is the term for damping γ_i due to losses, $\omega_i^2 x_i$ is the

term for the restoring force with the natural frequency of oscillation $\omega_i^2 = k_i/m_i$ (k_i spring constant; m_i mass) of each of the two oscillators $i = 1$ or 2. Ω describes the coupling between the coupled oscillators, and the oscillator in Equation 2.14 is driven by an external driving force with frequency ω and amplitude a. Note that the coupling term for oscillator $i = 1$ contains the position x_2 for oscillator 2, and vice versa.

Transforming the two equations above through a Fourier transform, we get

$$F(\omega) = (\omega_1^2 - \omega^2 + i\omega\gamma_1)x_1(\omega) + \Omega x_2(\omega) \tag{2.16}$$

$$0 = (\omega_2^2 - \omega^2 + i\omega\gamma_2)x_2(\omega) + \Omega x_1(\omega) \tag{2.17}$$

which describe oscillators that are perturbed by each other, but now in frequency space. The terms remain the same, albeit the driver is now $F(\omega)$. With the following substitutions

$$P_i = (\omega_i^2 - \omega^2 + i\omega\gamma_i) \tag{2.18}$$

the system of two coupled oscillators can be written in matrix form

$$\begin{pmatrix} P_1 & \Omega \\ \Omega & P_2 \end{pmatrix} \begin{pmatrix} x_1(\omega) \\ x_2(\omega) \end{pmatrix} = \begin{pmatrix} F(\omega) \\ 0 \end{pmatrix}. \tag{2.19}$$

Here, the terms P_1 and P_2 are the polynomials whose coefficients describe the damping and resonance frequency of the oscillators described by x_1 and x_2. The off-diagonal term in the matrix is the coupling Ω. The solution for x_1 and x_2 will yield a quadratic term due to the determinant, and thus, two solutions: these are the hybrid modes in the coupled system. The difference between the hybrid modes at resonance, most often given in terms of energy, is called the normal mode splitting, or Rabi splitting, especially when described in a quantum framework [11], [17]. An analogy can be drawn to the formation of molecular orbitals, where two isolated atomic systems come into proximity with each other and form new orbitals, the hybrid molecular modes.

If some optical modes are dispersive, that is, their optical modes are not linear with respect to the wavelength and AOI, geometries can be chosen such that they may couple with modes that do not show such dispersive behavior, such as excitons. Under these circumstances, the dispersion relation of the coupled system will exhibit hybrid modes by forming two branches whose separation is referred to as an avoided crossing [11]. The dynamic tuning of mode coupling and thus control over the resultant avoided crossing is the paramount topic of this thesis. More on this will be discussed in the upcoming section on current literature.

For coupling in optical systems to take place, proximity is also necessary. For this, different geometries of the optical system will be investigated and different resonator types of optical systems will be combined. The dynamic control of such systems via switchable molecules will be described in the next section.

2.7 Photoswitchable Molecules

The photoswitchable chromophore used in this thesis is 1,3-Dihydro-1,3,3-trimethylspiro [2H-indole-2,3 -[3H]phenanthr[9,10-b](1,4)oxazine] (hereafter, SPO or spirooxazine (PubChem CID: 3754026)). The SPO molecules can be switched from a closed-ring form to an open-ring form on exposure to UV light stimulus [3], [4], [43] (see Figure 2.8). The closed-ring structure is often termed the spiro [43] or the leuco form [5], terminology derived from leuco dyes: those dyes which reversibly change color upon a structural conformation change due to a specific stimulus. The open-ring form is commonly called the merocyanine (MC) form [5], named after a class of dyes with an amide resonance system. Switching conformational form is brought about by exposing the SPO molecules to UV light, hence the term photochromism [44] for this type of structural change of a chemical species due to the absorption of photons. This transformation of the molecule is commonly referred to as "switching." The conjugation of the switched, open-ring molecule is extended in comparison to the closed-ring structure [45], [46]. In general, the absorption of electromagnetic radiation shifts to higher wavelengths/lower energies,

when conjugation is extended in a molecule, and that is also true here. As explained below, absorption wavelengths for the closed-ring, leuco form of the dye lie just beyond the visible region in the ultraviolet, at about 350 nm. After exposure to 365 nm UV light for a sufficient time period, the molecule displays absorption at wavelengths around 590 nm.

Switchable molecules were the subject of interest in the Collaborative Research Center (CRC, or SFB in German for "Sonderforschungsbereich") 677 "Function by Switching", of which the author was a member. The CRC 677 focused on "molecular switches and machines in the field of molecular nanoscience." The switching of molecules refers to the change of conformation induced by a stimulus. Such molecules are often referred to as "dyes" or "chromophores" [44] due to their inherent coloring in one or more conformations.

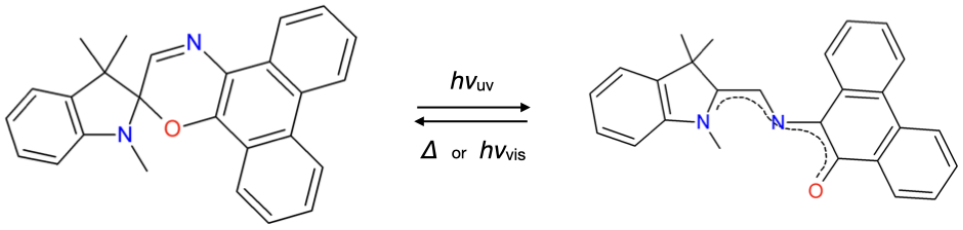

Figure 2.8: Photochromic transformation of SPO [45], [46] from a closed-ring leuco structure (left) to an open-ring merocyanine structure (right). Upon switching of SPO, the molecule becomes more highly polarizable. This is expressed in the resonance behavior that will be seen in the spectra of the optical constants of the molecule. This is accompanied by strong absorption for the electronic transition at the molecule's resonance frequency, which accounts for the visible blue color of the switched molecule. The optical mode is referred to as a photoswitchable molecular exciton.

2.8 Theory for Sample Preparation

Samples were prepared by the author on site. The necessary theoretical information for preparation of samples via sputter chamber deposition and spin coating will be described.

2.8.1 Magnetron Sputtering

The standard technique of physical vapor deposition of thin films with magnetron sputtering was used in this work for DBR production and will be briefly described here.

For production of samples, magnetron sputter deposition [14], [47] was used. It involves placing a sample to be coated in a vacuum chamber where a target of the material to be deposited is bombarded by nonreactive gas ions from a plasma burning above the target. The kinetic bombardment causes ejection (hence, "sputtering") of the material from the target surface and deposition on the sample substrate.

The gas ions are created by collisions of free electrons with working gas atoms in the plasma. Strong magnets are used to confine free electrons in the plasma cloud near the target surface in a ring-shaped volume. Electrons follow helical paths via the Lorentz force due to the magnetic field lines from the strong magnets beneath the target, in effect holding the electrons longer in the torus-like volume above the target. By increasing the residence time of the electrons above the target, the probability increases of electrons colliding with working gas atoms and forming ions for bombardment of the target.

The electrons cause the formation of gaseous ions upon collision with gas molecules (here, argon), which are then accelerated towards the target for sputtering by a bias voltage. The formation of a circular area of erosion (the "racetrack") on the target surface forms over time due to the ring-shaped volume of ion-forming plasma above the target caused by the arrangement of the permanent magnets under the target.

DC magnetron sputtering [14], [47] is well suited for conducting targets, i.e., the Ag and Au used here. However, non-conducting, dielectric targets would charge up rapidly and prevent further sputtering.

To make dielectric sputtering possible, the polarity of a voltage bias supplied to a capacitor connected to the target alternates typically at the frequency of 13.56 MHz, a radio frequency (RF). Hence, the technique is called RF magnetron sputtering [14].

Electrons can follow the oscillating voltage but ions cannot. In effect, the target becomes net negatively charged ("self-biasing"). The capacitor prevents de-charging of the target, which remains net negatively charged. The positive argon ions continue to

bombard the negative target, causing sputtering of the dielectric.

In this way, charging of the target is avoided and the impedance of the circuit is lowered enough to allow ignition of the plasma.

RF sputtering requires not only an RF power source but also a matching network [47] (a.k.a. matching box), a system of capacitors and inductors that match the impedance between the power supply and the sputter system so as to maximize power transfer to the system and minimize reflected power from the system.

RF magnetron sputtering has the benefits of lower working pressures, higher film purity, and higher deposition rates.

2.8.2 Spin Coating

One requirement for the experiments in this thesis is to deposit polymer layers, on the order of a few tens of nanometers, that include varying concentrations of switching molecules. One of the standard techniques for such deposition is spin coating.

The basic principle [15] is to dissolve the polymer under consideration in a suitable solvent and to pipette an appropriate amount of this solution onto a substrate. The solvent evaporates and the remaining polymer forms a film. To ensure thickness homogeneity and to speed up the process of evaporation, the substrate is rotated around a centered axis normal to its surface. Solvent and polymer (and switching molecules) are then under centrifugal force. The force balance between centrifugal force and viscous drag of the solution results in a thickness of the polymer layer that can be adjusted by the rotational speed for a given viscosity of the solution. The latter mainly depends on the polymer concentration in the solvent. One drawback to this approach is that the resultant layer is not necessarily completely free of solvent, and sometimes the residual solvent must be removed by further annealing. The advantages to the method are that the technique is well established and the equipment is available in the Faupel group.

2.9 State-of-the-art Literature on Plasmon-Emitter Coupling

To couch the findings of this thesis into the wider scientific research on light-matter strong coupling, two quantum models will be described, followed by an overview of pertinent literature. Since the often used theories of the Jaynes-Cummings model and the extension of such to the Tavis-Cummings model will later be referred to, a brief description of the models will be given here. Considering that only the resultant equations of the Rabi splitting and coupling constant will play a role in the final discussion, the reader is encouraged to consult quality quantum optics or nanophotonics textbooks [48], [49] for details of the models.

In the subject of cavity quantum electrodynamics (cQED), the Jaynes-Cummings model [11], [17] is a quantum description of light-matter interactions and describes a coupled system of a single quantum two-level emitter, a single mode of an optical cavity quantized electromagnetic field, and the interaction of the two. From the sum of these three, the Jaynes-Cummings Hamiltonian is written, where the interaction part includes the coupling strength g between the photon and the emitter. The solution for the eigenstates reveals that they are a superposition of the emitter ground state plus one more cavity photon and the emitter excited state less one cavity photon. From the eigenvalue solutions, the energy splitting between the hybrid states at resonance can be calculated to give the Rabi splitting (actually called the vacuum Rabi splitting in the case of an excited state emitter placed in a cavity with no photons, where vacuum fluctuations provide the cavity mode). The model can be extended from one emitter to N emitters through a transformation that changes the effect of the collection of N emitters from all acting independently to all acting in concert as one large quantum oscillator, and results in what is termed the Tavis-Cummings model.

One general result of investigations into strong coupling is the relationship between the exchange of energy between the cavity and the emitter and the loss of energy to

any dissipation mechanisms in the system [50]. As a general rule, once the exchange rate of energy between the light and matter is greater (i.e., the coupling strength is greater) than the losses due to the decay rate of the cavity (e.g., loss of photons from the cavity to the far field) or non-resonant decay rate of the emitter (e.g., loss of photons to the far field, or any non-radiative losses of energy), the system is considered to be in the strong coupling regime. In effect, the avoided crossing of the dispersion relation becomes easily visible because the linewidths resulting from any losses or damping of the excitonic and photonic coupling partners are narrow enough and the Rabi splitting between the upper and lower polaritonic branches is great enough [11]. Without these conditions, the broadened linewidths of lossy coupling partners can mask the avoided crossing when the coupling and, therefore, the Rabi splitting is too small.

These quantum models and their resultant equations about the strong coupling regime of light-matter interactions and the proper use of such equations will be brought to bear later when putting the thesis findings into the appropriate theoretical framework from the literature.

A quick literature search on applicable keywords such as “plasmon polariton coupling” turns up more than thousand papers, which of course cannot be discussed here individually. Therefore, focus will be placed on review papers of the key researchers in the area and some papers that are very recent or for other reasons relevant.

An overview of the work in the area of strong coupling between plasmons and emitters was a report [11] by two leaders in the field of light-matter interactions, Professor Törmä and Professor Barnes. Here, the areas to be recapped from the paper will not include the topic of the coupled harmonic oscillators, as it was already covered in a previous section, nor the general overview of the Kretschmann setup and appropriate general theoretical concepts, which were already presented above. What will be recapped is a description of theoretical results and experimental verification. The quantum mechanical approach to describe strong coupling will be only discussed where classical or semiclassical models are not sufficient for the phenomena observed within the experimental framework of this thesis. Points that are relevant here are: the strength of coupling is dependent on the

square root concentration of emitters; the coupling strength relies on the exchange of energy between the coupled entities to be greater than any dissipation or losses in the optical system. After that, the experiments that have already been conducted in the field will be discussed in reference to a more recent review paper [51]. Finally, those papers found to be relevant to the topic and published even more recently and not yet included in any review paper will be briefly summarized.

As presented expertly in the 2015 review by Törmä and Barnes [11], the classical description of strong coupling between SPPs and matter begins with emitters assumed to act as classical Lorentzian oscillators, in other words, the dynamics of an electron in the molecule and its polarizability. After solving the equation of motion of a harmonically bound and damped oscillator for the steady-state solution and relating it through the macroscopic polarization density to the susceptibility, the authors arrive at a dispersion relation for the SPP-emitter coupled system in their equation 27. The graph of the dispersion relation (for simplicity, damping is assumed to be zero) is redrawn and presented in Figure 2.9. The horizontal red dashed line is the absorption frequency of the emitter. The diagonal red dashed line is the SPP dispersion without coupling. The crossing point of the two red dashed lines is where the energy and momentum of the uncoupled SPP and emitter match exactly. Once the two are coupled, the avoided crossing is plainly apparent in the black solid-line solutions (the upper and lower polariton branches) to the dispersion relation and is a hallmark of coupling in such systems. The black dashed lines signal to the reader that with finite damping, the nearly horizontal solution to the dispersion relation are less well-defined far away from the crossing point just discussed. Notice that the vertical axis is depicted in terms of frequency, but could just as easily be shown in terms of wavelength of light; such a depiction will however invert the results in the graph vertically due to the inverse relationship between wavelength and angular frequency. This alternative approach to graphing will be followed in this thesis.

At the above-mentioned crossing point, the resonance point upon coupling, there is a splitting or difference in frequencies of the polariton branches that is described as normal-mode splitting in the case of the classical interpretation or the Rabi splitting in

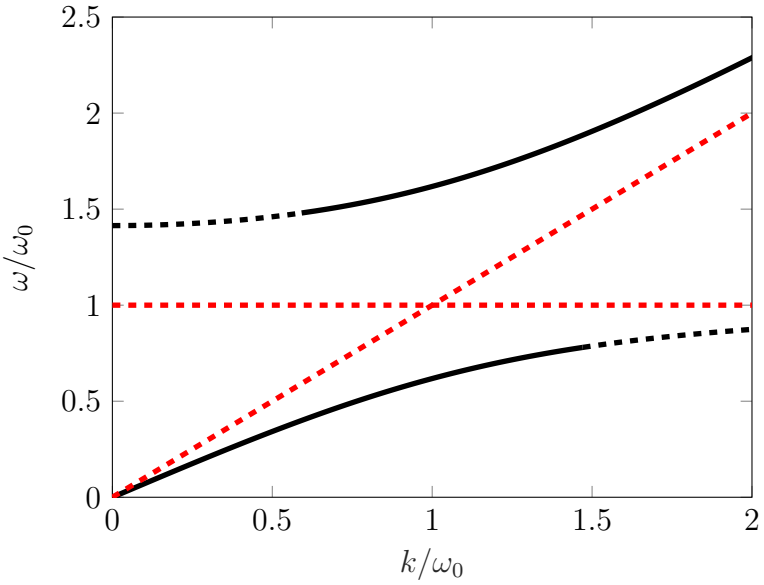

Figure 2.9: Redrawing of the dispersion relation of an SPP-emitter coupled system [11] that depicts the upper and lower polariton branches (black solid lines) defining the avoided crossing in between, together with the uncoupled emitter absorption frequency (horizontal red dashed line) and the SPP dispersion (diagonal red dashed line) whose intersection defines the so-called crossing point. Damping assumed to be nonexistent. The dashed parts of the black lines signal to the reader that in real systems with finite damping, the nearly horizontal modes are not well defined.

the fully quantum theory interpretation (not covered here in detail). The splitting value is denoted as

$$\Omega \propto \sqrt{\frac{N}{V}} \tag{2.20}$$

where N/V is the number of emitters in the volume of the mode, i.e., the concentration of emitters in the coupled systems. This same relationship applies regardless of the theoretical framework it is derived from, classical or semiclassical or fully quantum. Although there are slight differences in the proportionality constant derived for each method, the overall message is that the magnitude of splitting is a function of the emitter density, the confirmation of which in this thesis adds another piece of evidence to support the claim of (ultra)strong coupling to have been generated in the experimental

setup.

A review paper by Moilanen et al. [51] discusses important studies up to mid 2017 that involve in situ control of the coupling strength between emitters and plasmonic systems. The in situ control refers to changes to the system through external stimuli. Particular emphasis is paid in the review paper to those systems where photochromic molecules are involved and optically switched — thus, highly relevant to this work. Whereas photochromic switching of molecules form the excitonic part of the coupled systems, the plasmonic part of the systems reported on are varied from a cavity with two Ag mirrors or even a periodic hole array in a layer of Ag [52], to metallic nanoparticle arrays [53], to arrays of Al nanodisks [54], to earlier work on periodic gratings on films of Al [55] or even to disordered arrays of metal nanospheres, nanorods and nanodisks [56]–[58]. The first three studies will be described below as they are relevant to the current focus; all three studies involved reversible photoswitching of coupling.

For those studies involving photochromic molecules as the excitonic partner in coupling, the study by Schwartz et al. [52] could be considered seminal to the work presented in this thesis. Here, switching of chromophoric molecules in a traditional cavity made of sandwiching a doped dielectric layer between two Ag mirror layers was used to transition the coupling between cavity modes and the switchable molecules from the weak to the strong coupling regime. The Ag layers acting as mirrors for the cavity were 35 nm thick. The thickness of the intermediate dielectric layer of poly(methyl methacrylate) (PMMA) containing a photochromic spiropyran, although not specifically reported, was mentioned to have been adjusted to tune the empty-cavity resonance to a transmission wavelength of 560 nm, which was chosen to coincide with the absorption wavelength of the switched spiropyran at 560 nm so that coupling could take place upon switching the molecules. The Rabi splitting was reported to be 713 meV, about a third of the transition energy of the molecule at 2.2 eV, in the regime of ultrastrong coupling, defined historically [59] as the ratio of Rabi splitting to transition energy being greater than 0.2 [60]. In this thesis, a traditional cavity consisting of two Ag layers plus a dielectric layer in-between will not be used; instead, the cavity will involve two different approaches.

The cavity is either defined by the evanescent field from surface plasmon polaritons on a thin metal film adjacent to a dielectric layer or is defined by a spacer layer bounded by a Ag layer on one side but a distributed Bragg reflector on the other side.

Additionally, the Schwartz et al. [52] paper very briefly compared the results from their optical cavity mentioned above to a plasmonic structure in a second experiment. This was done in order to compare the achievable Rabi splitting magnitude for the two optical structures that were otherwise similar in setup, where only the nature of the cavity mode was fundamentally different. The plasmonic structure consisted of a dielectric layer of PMMA doped with photoswitchable molecules layered on a periodic array of holes in a 200 nm thick Ag layer. The transmission spectra of the samples were measured before and after switching the spiropyran molecules with UV light. Although their reported Figure 4 does seem to show the dispersion relation of the sample system before and after switching, it fails to impress the reader with a clear depiction of achieving strong coupling via photoswitching of molecules. Nonetheless, the Rabi splitting reported for the structure measured in transmission was 650 meV, proving to be similar in magnitude to the experiment with a traditional optical cavity of Ag mirrors. Unfortunately, the paper offers no more information on the experiment than one short paragraph and one small graph. Nonetheless, the paper, especially with regard to the plasmonic structure, can be viewed as an idea generator for the current thesis, which extends the idea of plasmon-emitter switchable coupling as follows. Although the photochromic molecule used in this thesis is in general similar in nature to that used by Schwartz et al., the cavities used to form the mode coupling partner will be altogether different in their approach: one cavity will use a Kretschmann configuration with a prism to launch surface plasmon polaritons and concomitant evanescent waves as localized modes, whereas another cavity setup will use an entirely different method with a Tamm plasmon created as modes between a Ag layer and a distributed Bragg reflector with a photochromic molecule-doped dielectric spacer layer in between.

Also reviewed by Moilanen et al. [51], Baudrion et al. [53] used a photoswitchable spiropyran doped PMMA layer as the exciton supplier with a Ag nanoparticle array

embedded within as the plasmonic part of the coupled system. Upon switching the photochromic molecules with UV light, a Rabi splitting between the hybrid modes was measured to be 294 meV, a value much less than those reported by Schwartz et al. [52] (indeed, much less than the values to be reported in this thesis), which was attributed to the lower quality factor of the dipolar resonances compared to the setups by the Ebbesen group [52]. A minor point of interest in the Baudrion et al. paper is that the backswitching was performed with thermal treatment of the dielectric layer at 40 °C for 10 min, and although backswitching was confirmed, the samples were reported to have evidence of fatigue of the polymer as the amplitude of extinction spectra was lower after thermal cycling.

As the third paper to be mentioned here from the review by Moilanen et al. [51], it will simply be said that Lin et al. [54] reported Rabi splitting up to 572 meV in samples of photochromic molecules doped in a PMMA layer coupled to hybrid plasmon-waveguide modes from Al nanodisk arrays embedded in the selfsame layer. A thorough description of the nature of the plasmon modes used by Lin et al. are beyond the scope of this thesis. Suffice it to say that the Rabi splitting of 572 meV between the hybrid plasmon-waveguide modes and the photochromic molecules is on the order of the Rabi splitting achieved in this thesis with surface plasmon polaritons on a metal layer in a Kretschmann configuration, albeit with a different type of plasmonic entity.

Other studies (without photochromic molecules) reviewed by Moilanen et al. [51] involved J-aggregates (aggregations of dye molecules [61]) as the excitonic coupling partner along with localized surface plasmon resonance modes in single dimers [62], or Al nano rod arrays [63], or arrays of holes in a Ag layer [64], or an array of nanoslits in Au [65]. In addition, prism-mediated SPPs were coupled with fluorophores [66]. Although all studies offered a window into the world of strong coupling for the author of this thesis, the discussion of those papers are beyond the scope of the focused discussion here.

Recent papers of the groups of Törmä, Ebbesen, Shegai, Antosiewicz, and Barnes do include topics involving coupling, however their work goes in directions other than that presented here. However, a very recent peer-reviewed communication of the Barnes

group is of interest, as it discusses a possibly new signature in ellipsometry for identification of strong coupling [60].

2.10 State-of-the-art Literature on Tamm Plasmon Polaritons

The existence of what would later be called Tamm plasmons was first theoretically described in 2003 [12] and experimentally confirmed in 2008 [67]. Much interest in Tamm plasmons has been shown in the literature in the last ten years. Particularly pertinent publications will be described here.

To maximize efficient Tamm plasmon polariton excitation by incident light, Kumari et al. aimed to determine the appropriate number of DBR bilayers and thickness of the top metal layer [69]. They determined that, although not linear, the greater the number of DBR bilayers, the greater the required thickness of the metal layer on top, up to a maximum of 100 nm Ag thickness where the metal's bulk character would begin to prevent incident light penetration at all. They showed that the essential requirement for the existence of Tamm plasmon polaritons is that the sum of the phases of the complex reflection coefficients from the metal-dielectric interface and the DBR-air interface must equal zero (more on this in the upcoming discussion of the paper by Auguié et al. [70]).

Specifically pertinent to this thesis, Kumari et al. [69] show that for a silver layer about 35 nm thick, the best coupling efficiency to incident light requires a DBR with very few bilayers, which informed the creation of the Tamm setups used in this thesis. In addition, the use of few bilayers has the added benefit of avoiding the creation of an effective "defect mode" in the DBR stack due to variations in the layer thicknesses from bilayer to bilayer. Such a defect mode, if present, would create an additional dip in the reflectance spectrum (as present in some samples of Kumari et al.), possibly obscuring the intended observation of strong coupling and hybrid mode splitting in the sample. With this information, the goal is to make a Tamm plasmon sample setup with very few

bilayers and a very thin metal top layer.

Auguié et al. [70] investigated with numerical simulations in an excellent paper the conditions of critical coupling of incident light to create Tamm plasmons. With the addition of a spacer layer between the top metal layer and the DBR, they show that the condition of constructive interference in the spacer layer is a round-trip phase angle change of zero in the layer, essentially the same result as required for the existence of the Tamm plasmon (no spacer layer) described above by Kumari et al. A phase change of zero through a round trip in the spacer layer results in the formation of a standing wave there; this condition characterizes the Tamm plasmon polariton, and determines its location in the spectrum. In addition, the authors also show theoretically that whether the incident light is from the metal or DBR side of the sample is irrelevant in cases where absorption of the light in the sample is not complete. Since the sample to be prepared in this thesis, as shown above, will have very few bilayers and a thin metal top layer, radiative losses will exist in the sample and 100% absorption of the light will not be possible. Therefore, irradiating the sample from the top will be sufficient for observing possible coupling in the sample between Tamm plasmon polariton modes and the switched SPO excitons.

Through calculations and experiments, Symonds et al. [38] investigate the effect on conventional Tamm plasmon structures (DBR with thin metal layer on top) of inserting a spacer layer between the metal layer and the DBR. As described above (Figure 2.6), the insertion of a spacer layer leads to a shift in the envelope of the electric field intensity towards the bottom of the DBR compared to the Tamm mode, but not as far as the Bragg mode's envelope. Symonds et al. refer to the setup with a spacer layer as creating a "super" Tamm mode (Figure 2.6 c), terminology that will be eschewed here as superfluous. In such a setup, losses associated with the metal are reduced compared to the conventional Tamm plasmon mode (Figure 2.6 b) due to the envelope being shifted further away from the metal-dielectric interface, i.e., the mode is bound less to the metal interface. With this, the electric field extends less into the metal when a spacer layer is present, with concomitant reduction in metal losses. However, the radiative losses out

the bottom of the DBR are reduced compared to the first Bragg mode (Figure 2.6 a) due to the field maximum being located further from the DBR bottom, a finding the authors support in their calculations. In effect, what they call a super Tamm mode (i.e., with the spacer layer) is something between a Tamm mode and a Bragg mode in the location of its electric field intensity envelope maximum.

It can be determined through the calculations and experimentation of Symonds et al. [38] that a quality factor improvement 5 times greater was achieved in the spacer layer setup compared to the quality factor of the conventional Tamm mode and about 2.5 times greater compared to the quality factor of the Bragg mode, which they attribute to lower losses at the metal and lower losses to radiative modes out the bottom of the DBR. With this in mind, a higher quality factor optical mode existing in the spacer layer will be used in this thesis for strong coupling experiments made possible due to the confinement of light there.

The Symonds et al. setup, although different in specifics of the DBR materials and numbers of bilayers, is instructive for the Tamm setup to be presented in this thesis. A spacer layer of PS-SPO inserted between a DBR and a top Ag layer will support a confined optical mode that can couple to the excitons of switched SPO when the Tamm mode is tuned to the exciton energy.

The theoretical investigation published by Morozov et al. [13], [71] in mid 2019 predicted that strong coupling would be possible in an organic spacer layer containing excitons inserted between a DBR and a Ag top layer. They make theoretical calculations of strong coupling (and also its effects of broadening the luminescence bandwidth of luminescing molecules), showing calculated dispersion relations with and without excitons in the spacer layer. Such strong coupling had not yet been demonstrated experimentally.

In this thesis, Tamm plasmon-molecular exciton coupling is demonstrated for the first time in the strong coupling regime. The sample will consist of a SPO doped-spacer layer inserted between a DBR and a top metal layer. Choosing the thickness of the spacer layer to place the Tamm plasmon at the same energy as the exciton transition energy will allow for energy exchange between the two entities — strong coupling can

occur.

In addition and also for the first time, the coupling in the Tamm plasmon-molecular exciton system was made switchable. This was done with the use of SPO as a photochromic molecule as the exciton formation source in the spacer layer.

CHAPTER 3

Experiments

As described in the previous chapter on the theory and background for this dissertation, the objectives of the studies at hand are to look into the coupling between excitons and surface waves, the components of a molecular plasmonic system. Before samples could be prepared, simulations would have to be performed to gain insight into the important parameters of the identities and thicknesses of the layers in the systems and into the exact prism setup to be used in the Kretschmann configuration.

3.1 MATLAB Calculations for Suitable Sample Designs

As studies were begun, MATLAB code and a central script were written[1] that included complex indices of refraction for various materials (including PS, Au, Ag, and BK7 glass), and the Fresnel equations and the function "jreftran" by Shawn Divitt [72] ("a layered thin film transmission and reflection coefficient calculator"), which was in turn based on a technical report by Pascoe [22] that involves the transfer matrix method described in the Theory section. The scripts were needed to calculate the parameters for and simulate various combinations of materials that could be used for investigating the degree of coupling between molecular excitons and SPPs in a system comprised of an SPO-loaded dielectric plus a metallic layer to host the SPPs. In addition, the prism to use for the Kretschmann configuration was chosen based on the simulations: a right

angle BK7 glass prism.

In particular, various thicknesses of both the precious metal and the dielectric were also simulated in an array of many possible combinations. Simulations were important to the success of the experiments because the sheer number of possible combinations of prism glass together with potential types and thicknesses of metal and also thicknesses of the dielectric layer precluded experimentation. In addition, the final samples exhibiting possible SPP-exciton coupling had to be measurable on a spectroscopic ellipsometer where the AOI range is limited to values from 45° to 90°.

Many combinations of materials and thicknesses do result in a dispersion relation, but often of weak intensity or at angles of incidence outside the angle limits of the instrument. With the use of the tool of MATLAB calculations, judicious choices of parameters and materials could optimize the intensity of absorptions to be measured.

Most importantly, the main condition of the experiment was set by the absorption wavelength of the MC form of SPO at about 600 nm. The metal-dielectric system had to be so devised as to bring the dispersion relation of the SPPs into a range to overlap with the absorption wavelength of the switched SPO at ~600 nm so that coupling could occur to maximum effect. The right choices of the best parameters necessary to achieve all this could be identified with the simulations. For example, the metals to be used, the thickness of any PS-SPO layers, and the materials and layer thicknesses in the DBR were all pre-determined with simulations which informed the choices and values presented in the following experimental sections.

[1]As denoted in the Theory section, Ron-Marco Friedrich wrote the majority of the MATLAB simulation code used here, and his help in such programming has been greatly appreciated.

3.2 Spectroscopic Ellipsometry: An Investigative Means

In the previous section, simulations were described that allow determining the desired parameters of the components for a molecular plasmonic system that could be used to investigate the coupling between excitons and surface waves. Here, the experimental operation needs to be described for the instrument used to measure the optical properties of the components and the overall sample systems: a spectroscopic ellipsometer.

The instrument used for the measurements was an M-2000UI Spectroscopic Ellipsometer with an EC-400 Electronics Control Module, see Figure 3.1. The light source has two lamps installed: a 30 watt D2 (sic) deuterium lamp for UV and some visible wavelengths and a 20 watt QTH lamp for IR and other visible wavelengths. The combined spectral range is 245 nm to 1690 nm. The light beam is set to strike the sample on the stage at a chosen angle between 45° and 85° from the sample normal. The sample orientation is adjusted manually for alignment of the reflection beam onto a detector by adjusting the tilt of the stage with knurled dials. The reflected beam is detected in a receiver unit, an MQD dual receiver unit in this case. The emitted light is polarized and contains both p-polarized and s-polarized light. After reflecting from or transmitting though the sample, the change in the polarization of the light delivers information from which the optical constants and layer thickness(es) can be determined. The spectroscopic ellipsometer is equipped with a sample stage in the reflection mode. When a sample is placed at the center of the stage, a vacuum assist is turned on to hold the samples securely during measurement. With the sample in place, the sample's response to light can be measured at one fixed angle, which with modeling ultimately leads to determining the n and κ values across all accessible wavelengths. The response can also be measured from 45° to 85° in steps of 0.5° for a total of 81 angles, ultimately leading to a dispersion relation across all wavelengths. The acquisition time per angle was set to 5 s.

a) b)

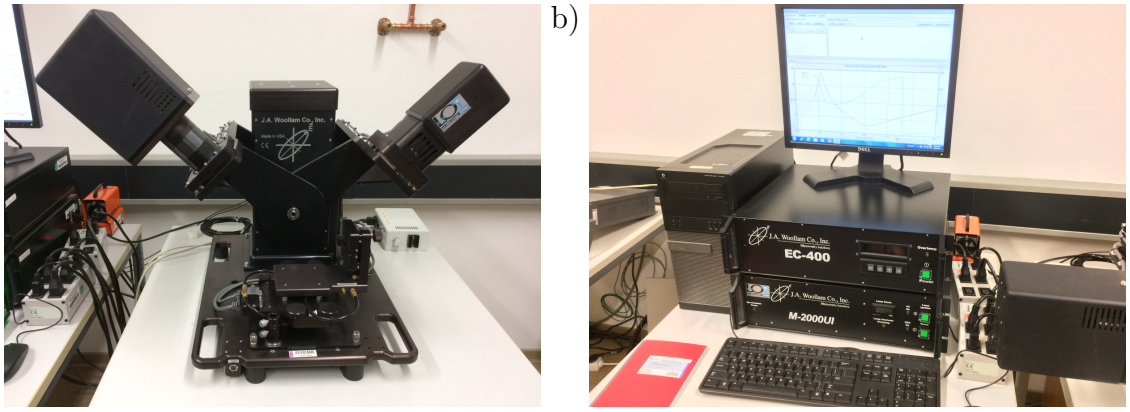

Figure 3.1: Spectroscopic ellipsometer (a) with controller and modeling software (b) used in these experiments to determine thin film layer thickness and optical constants, n and κ. From J.A. Woollam Co. Inc., Lincoln, Nebraska, USA. Shown with transmission stage installed.

When a prism is used in the Kretschmann configuration [2], [31] to allow the incident ellipsometer light to launch SPPs in the sample, measurement of the dispersion relation is slightly more complicated. The dispersion relation is still measured from 45° to 85° in steps of 0.5°, but the measurements are taken in sets of 10° from 45° to 55°, 55.5° to 65°, etc. In between sets, the stage height is adjusted to keep the beam incident on the sample. In addition, the detector itself is angle adjusted to maintain a strong signal. These additional steps are necessary due to the presence of the prism, which changes the angle at which the incident light interacts with the sample adhered to the bottom side of the prism.

Because no prism is used in the measurements of the Tamm samples, the additional task of adjusting the sample stage height and the angle of the detector are omitted. The measurement of the sample becomes a straightforward run-through of all 81 angles from 45° to 85° to measure the dispersion relation of the sample.

3.3 Investigation of Optical Constants of PS-SPO

After the explanation of the simulations that identify the necessary parameters for the molecular plasmonic system and of the operation of the instrument for measuring the properties of such systems, sample preparation can now be described.

To begin, the chromophore, as a switchable agent, is able to form excitons in the switched state, but the particular optical properties of the unswitched and switched states of SPO in a PS matrix needed to be determined. For this, samples of a polymer matrix containing the chromophore were prepared and subsequently investigated.

3.4 Preparation of Sample Series 1 for PS-SPO Optical Constants

Experiments were to be conducted with layers of SPO molecules [3]–[8], [44] hosted in a PS matrix to explore the switching behavior of SPO upon UV irradiation. The concentration of SPO in the PS matrix could be varied by changing the weight percent amount of SPO in the layer. In this way, the optical constants of the PS-SPO layer could be varied in several concentration steps from those due to 0 wt% SPO up to 100 wt% SPO. Measurements of the optical constants n and κ were to be obtained from spectroscopic ellipsometry investigation of thin film layers deposited on a reflective, bulk gold surface.

To begin, the optical constants for PS-SPO in different concentrations needed to be determined. This could be done with samples consisting of PS-SPO on a glass substrate, but the signal strength was somewhat low due to insufficient reflection from an otherwise transparent sample of PS-SPO on glass. After initial tests, the signal from the sample was increased by depositing the PS-SPO on a reflective, bulk Au layer (Figure 3.2). Au

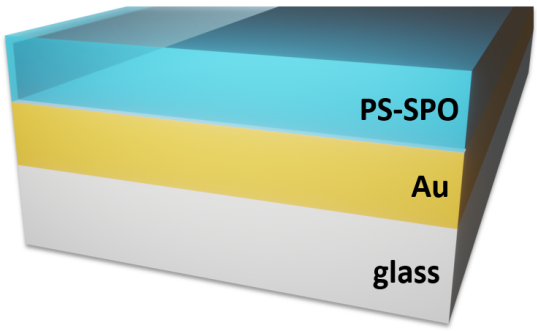

Figure 3.2: Schematic[2] of sample series 1: glass substrate (microscope slide), sputtered bulk Au layer (~150 nm), PS-SPO layer (~100-200 nm) samples for determining optical constants of varied concentrations of PS-SPO layers. Layers not depicted to scale relative to one another.

was chosen for its easy sputter deposition characteristics and relative inertness (no oxide layer formation and the attendant long-term tarnishing typical of Ag, nonetheless a metal used later in this study). The minimum thickness necessary to impart the optical constants of bulk Au were determined with simulations in the CompleteEASE software to be about 100 nm Au. In any case, the deposited bulk Au layer, at approximately 150 nm thick, was more than sufficient to ensure good reflectivity and a strong signal on the ellipsometer for determining the PS-SPO optical constants in both the unswitched and switched states. As a side note, any image charges [32], [73] created in the Au layer by polarizable molecules in the adjacent dielectric layer can be neglected because of the large film thicknesses of the dielectric layer (~100-200 nm).

To create the samples, Au was sputtered onto a glass substrate. The opaque, bulk Au layer was deposited via a Balzers SCD 050 magnetron sputtering instrument (Au target, 30 mA, 700 s, stage height 6 cm). Before PS-SPO layer deposition, the thickness of each Au layer was confirmed on the spectroscopic ellipsometer to be thick enough to have the optical constants of bulk gold.

Subsequently, a PS-SPO layer was deposited on top of the bulk Au layer via spin coating. The PS-SPO layer concentrations consisted of the following PS to SPO weight percentages: 100-0 wt%, 80-20 wt%, 60-40 wt%, 50-50 wt%, 40-60 wt%, 0-100 wt%.

[2]Schematic diagram created by Salih Veziroglu. Many thanks to him and his talents.

Appropriate relative amounts of PS (Roth, Art. No. 9151.1, molecular weight 320,000 g/mol) and SPO (1,3-Dihydro-1,3,3-trimethylspiro[2H-indole-2,3´-[3 H]phenanthr[9,10-b](1,4)oxazine] from Chemical Point, CP119980-36-8-BULK) were weighed out and dissolved in a solvent of clean toluene (Roth, >99.8% UV/IR grade, Art. No. 4445.1) for the creation of each solution. In each case, a 1 cm^2 substrate of glass with bulk gold on it was positioned at the center of the spin coater's vacuum chuck which held the sample firmly in place. To begin, a 50 µL aliquot of the chosen solution of a desired weight percent concentration was pipetted onto the still, non-rotating substrate. Spinning of the sample was commenced and accelerated for a total of 6 s to a final speed of 3000 rpm. The total spin time was 1 min, at the end of which the spinning stopped automatically. The sample was then removed from the chuck, and the determination of the layer thickness and the optical constants could then be performed via ellipsometry.

3.5 Analysis of Sample Series 1 for PS-SPO Optical Constants

For the determination of the optical constants n and κ for the PS-SPO layers on a spectroscopic ellipsometer, the thickness of a layer need not be controlled carefully but only accurately determined to permit modeling of the optical constants for the layer. From the Ψ and Δ values, the n and κ values were modeled with the instrument software according to the description in the Theory section. The modeling was performed with the accompanying instrument software, CompleteEASE (version 5.19, also Woollam [26]), after the author was trained by a representative of the manufacturer at a three-day seminar in Darmstadt, Germany.

Examples of raw Ψ and Δ data, poorly fitting model data, and excellently fitting model data are presented in the Results & Discussion section Figures 4.2 through 4.4.

The modeling of each sample's response to light was generally performed as follows. The substrate, whose material had been previously characterized in the appropriate

manner of incidence (reflection mode stage), was chosen for the model, or in the case of an opaque and bulk Au superstrate (a general term for any stacked layers superimposed on a substrate), the substrate was arbitrarily chosen to be "fused silica (Sellmeier)" since the substrate would not interact with the probing light due to the opacity of the Au layer. In the model, a layer of Au was added to the stack from the software database of materials (Au_nk3, a general oscillator model matched to Palik's Au optical constants from 140-1100 nm). The Au layer thickness was set to 150 nm, since the actual thickness need only be much thicker than 100 nm Au to achieve bulk gold optical constants. The 150 nm thickness was chosen in line with the approximate expected thickness from the 700 s sputter deposition. Since a layer of PS-SPO spin-coated onto bulk Au was transparent to the naked eye in the unswitched state, the PS-SPO layer could be initially modeled as a Cauchy layer [20], [25], [27] for transparent materials (where κ is assumed to be 0 for all wavelengths, i.e., no absorption), at least in the visible region starting at about 650 nm and into the infrared region up to at least 1000 nm. At about 600 nm, PS-SPO would absorb in the switched SPO state (the MC conformation), so the modeling could be performed at wavelengths above 650 nm without potentially involving any absorbing species present in the sample. The A and B (and rarely C) parameters of the Cauchy model could be set as fitting parameters, along with the thickness of the layer, and the software allowed to fit. Once the visual fit of the model was sufficient when compared to the data, the thickness of the layer was said to be determined and the value was fixed in the model since the thickness of the sample determined over a large range of wavelength values (~650 nm to at least 1000 nm) was sufficient. After fixing the thickness of the PS-SPO layer, the n and κ values for wavelengths below ~650 nm needed to be determined.

For the continued modeling of n an κ below ~650 nm, the Cauchy layer was parameterized into a B-spline layer with a resolution of usually 0.300 eV (or even 0.100 eV for spectra with narrower, more detailed peaks) between fitting points. A wavelength range expansion fit was used to expand the fit automatically, point by point, from the 650 nm wavelength down to the low end of the wavelength range, usually < 300 nm.

It was essential to set the increment of the wavelength range expansion fit to the same amount as the chosen resolution (again, usually 0.300 eV) by hand before the expansion fit was started. The general visual fit of the model to the recorded data was observed and the MSE value was noted. As per the manufacturer's training seminar, the visual fit was always taken as more important than any particular value of the MSE, which could be viewed as somewhat arbitrary because it always depends on the complexity of the model. Again, an example of measured data along with fits both unsatisfactory and satisfactory are shown in Results & Discussion section Figures 4.2 through 4.4..

Once the sample had been measured in the unswitched state, the next step was to switch the molecules of SPO with UV light and then remeasure the sample. The sample was exposed to the light of a UV LED (365 nm) from a fiber optic cable fitted at the end with a wand. It could be positioned above the sample slightly off center (~10°) so as not to block the incident and reflected light beam paths of the ellipsometer. Here, the exposure time for switching the SPO molecules was set to about 2 min to ensure a stable equilibrium between unswitched and switched molecules, and the UV light was left on during the brief measurement of the sample.

After the experimental values of the optical constants for layers of various PS-SPO concentrations had been modeled and determined, they were used in simulations to get a more accurate prediction of the response to light in both unswitched and switched samples prepared for the Kretschmann prism setup, to be explained next.

3.6 Investigation of SPP & SPO Coupling in Kretschmann Setup

Once the optical constants had been determined for the various concentrations of the PS-SPO layer, the next step was to make samples to be used in a Kretschmann setup [2], [31]. The setup uses a prism to allow the incident light of the ellipsometer to launch SPPs on a metal located adjacent to the prism. When the metal is proximate to a

PS-SPO layer (the dielectric layer), evanescent waves from the SPPs extend into the PS-SPO layer, thereby setting up the possibility of coupling between the SPPs and excitons of switched SPO molecules.

The use of a prism in the Kretschmann setup (Figure 3.3) is one way of launching SPPs on the surface of a metal, as described in the Theory section. The samples in such a setup require a metal of the right type and thickness to be conducive to launching SPPs with evanescent fields that extend into the dielectric layer. First, the determination of the metal to be used for the experiment and the required thickness of the metal was explored via simulations. Both Au and Ag showed in simulations to be metals that were suitable for launching SPPs with well-defined signals for measurement on the ellipsometer. Additionally, both metals could be deposited in a straightforward manner experimentally with the equipment available. In comparison to Ag, Au has the added benefit of inertness to oxidation.

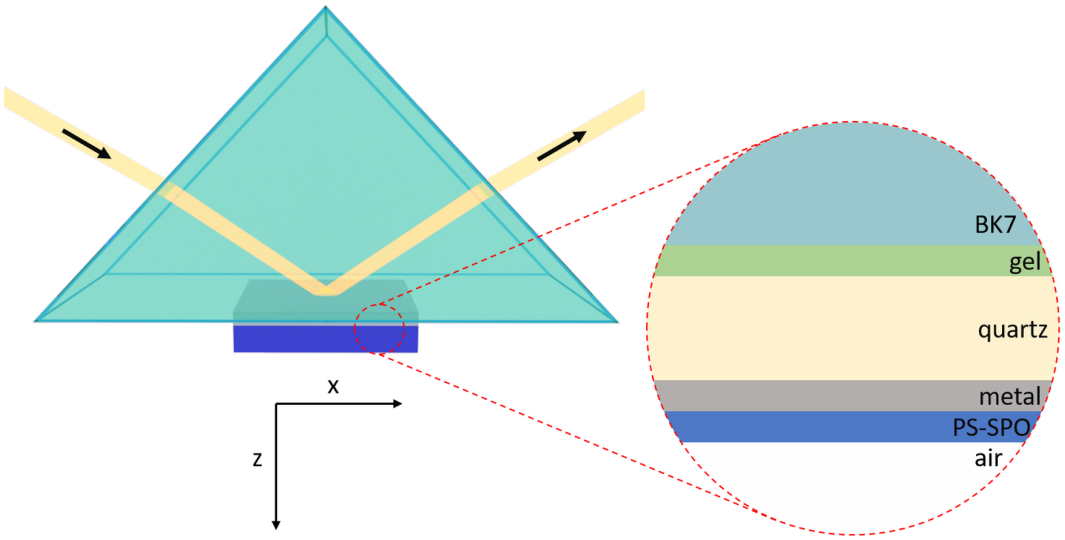

Figure 3.3: Schematic diagram[3] of Kretschmann configuration for measurement of the dispersion relation of a molecular plasmonic system. Square sample is adhered to the base of the right angle BK7 prism. Index matching gel adheres the sample to the BK7 prism and approximately matches the index of refraction of both BK7 and quartz substrate (thicknesses of layers in blow-up image not shown to scale relative to one another). Typical layer thicknesses: PS-SPO $\approx$ 40 nm, metal $\approx$ 50 nm.

As far as PS-SPO layers were concerned, the same solutions used for the previous section on determining optical constants could be used for the creation of samples for the Kretschmann setup, but this time the final thickness of the PS-SPO layer would have to be carefully controlled to achieve the thickness specified by the simulations. Quartz would be used for the substrate due to its reduced absorption in the UV region of the spectrum compared to microscope slide glass, a condition possibly necessary for later switching the SPO in the sample with a UV LED through the substrate.

3.7 Preparation of Sample Series 2: PS-SPO + Metal + Prism

To produce the samples for the Kretschmann setup [2], [31], metal on quartz substrates would first need to be made. Clean quartz squares (1 cm^2, 525 µm thick) were covered in a layer of Au or Ag in a commercial plasma-magnetron sputter chamber, a Balzers SCD 050 Sputter Coater, to the layer thickness determined with the simulations. From metal deposition rates estimated from the previous deposition of sample series 1 and additional test samples where necessary, the total deposition time for each Au or Ag layer could be calculated and programmed into the sputter coater. Once deposited, layer thicknesses for sample series 2 were verified on the Woollam spectroscopic ellipsometer with the use of CompleteEASE software [26], as had previously been done for sample series 1. In cases where the thickness was not enough, another deposition duration was calculated and the deposition conducted, followed by thickness determination on the ellipsometer.

Next, the PS-SPO solution needed to be diluted for deposition of the necessary thickness on the Au or Ag layer. PS-SPO solutions had already been prepared for sample series 1 and could be used for sample series 2, but the thickness of the layers had to be controlled carefully this time to match the requirements of the simulations. All sample layers were too thick compared to the simulation specifications, so an aliquot of

[3]Schematic diagram created together with Salih Veziroglu.

each solution was diluted with a few microliters of toluene, spin-coated on a substrate of bulk metal and the layer thickness checked on the ellipsometer. The dilution and deposition was repeated once or twice until the desired thickness from the simulation was reached for each particular PS-SPO concentration.

Deposition of the PS-SPO layer of a desired thickness could then take place. The diluted PS-SPO solutions were deposited on the finished metal layer with a commercial spin coater from Laurell as described earlier: 50 µL solution pipetted onto non-spinning samples, accelerated in 6 s up to a final 3000 rpm and spun at that angular velocity for the remainder of 1 min total time. Again, layer thickness was verified via spectroscopic ellipsometry and compared with the desired thicknesses from the simulations. With the desired and actual thicknesses in relative agreement, the finished samples could now be attached to the BK7 prism for measurements in the Kretschmann configuration.

To create the final Kretschmann configuration (Figure 3.3), the clean quartz side of a sample from series 2 was adhered to the base of an N-BK7, uncoated, right-angle prism (Thorlabs, PS911) with a thin layer of index matching gel (Thorlabs, G608N3, refractive index at 589.3 nm: 1.4646) to act both as a viscous adhesive for the sample and as a index matcher between the prism and the quartz substrate for the incident light, thereby reducing the reflective effects of the interface surfaces between the prism and the quartz substrate.

3.8 Analysis of Sample Series 2: PS-SPO + Metal + Prism

For analysis on the spectroscopic ellipsometer, the Kretschmann system (prism plus sample) could then be placed sample-side down (Figure 3.4) above an upward-facing, dimmable UV LED light (Nichia NVSU233B SMD-LED UV, 1450 mW, 365 nm), which was connected to a power supply. The prism was supported only on its perimeter by an aluminum housing having an appropriate cutout to expose the LED inside. Samples

could thus later be exposed from below to UV light to switch the SPO chromophores to the MC conformation.

First, the sample was left unswitched, i.e., unexposed to UV light, and each AOI from 45° to 85° was measured in steps of 0.5°. With this, the entire dispersion relation of the metal/PS-SPO sample without the possibility of coupling could be plotted. Switching of the SPO was performed at maximum intensity of the LED for a period of time between 20 and 30 s, a duration that had been determined in the following way: On exposure to UV light of 365 nm, in situ measurements at 57° AOI were used to monitor the splitting of the hybrid peaks due to coupling until equilibrium had been reached and the peaks no longer moved apart. This took 20 to 30 s. The minimum time necessary to reach equilibrium and stationary hybrid peaks was preferable to unnecessarily overexposing the sample to UV light, which had been seen to cause sample deterioration if left on for several minutes (Figure 3.4). Once equilibrium had been reached and the hybrid peaks no longer moved farther apart, the UV light was turned off and the entire dispersion relation was immediately measured from 45° to 85° at 0.5° steps within a total sweep time of just less than 10 min. The UV light was not kept on during the full angle sweep to prevent some peak reduction that had previously been observed, the origin of which is possibly degradation of the sample from the proximity and intensity of the UV LED.

The intensity of UV LED light used to switch the SPO conformation was kept the same from sample to sample for the various PS-SPO concentrations. The UV exposure duration, although differing slightly from sample to sample, remained within the range of 20-30 seconds total time. Exposure time was less important than reaching a point where peak movement slowed to a nearly undetectable minimum on exposure, monitored in situ at 57° AOI during UV illumination.

The concept of backswitching must be mentioned here. Once the UV light is turned off, the SPO molecules in the MC form in the sample do revert to the unswitched form at room temperature over a period of several hours, reverting most quickly just after the light has been turned off. If the backswitching were fast enough, the concentration of MC molecules, and therefore excitons, in the switched sample could decrease during

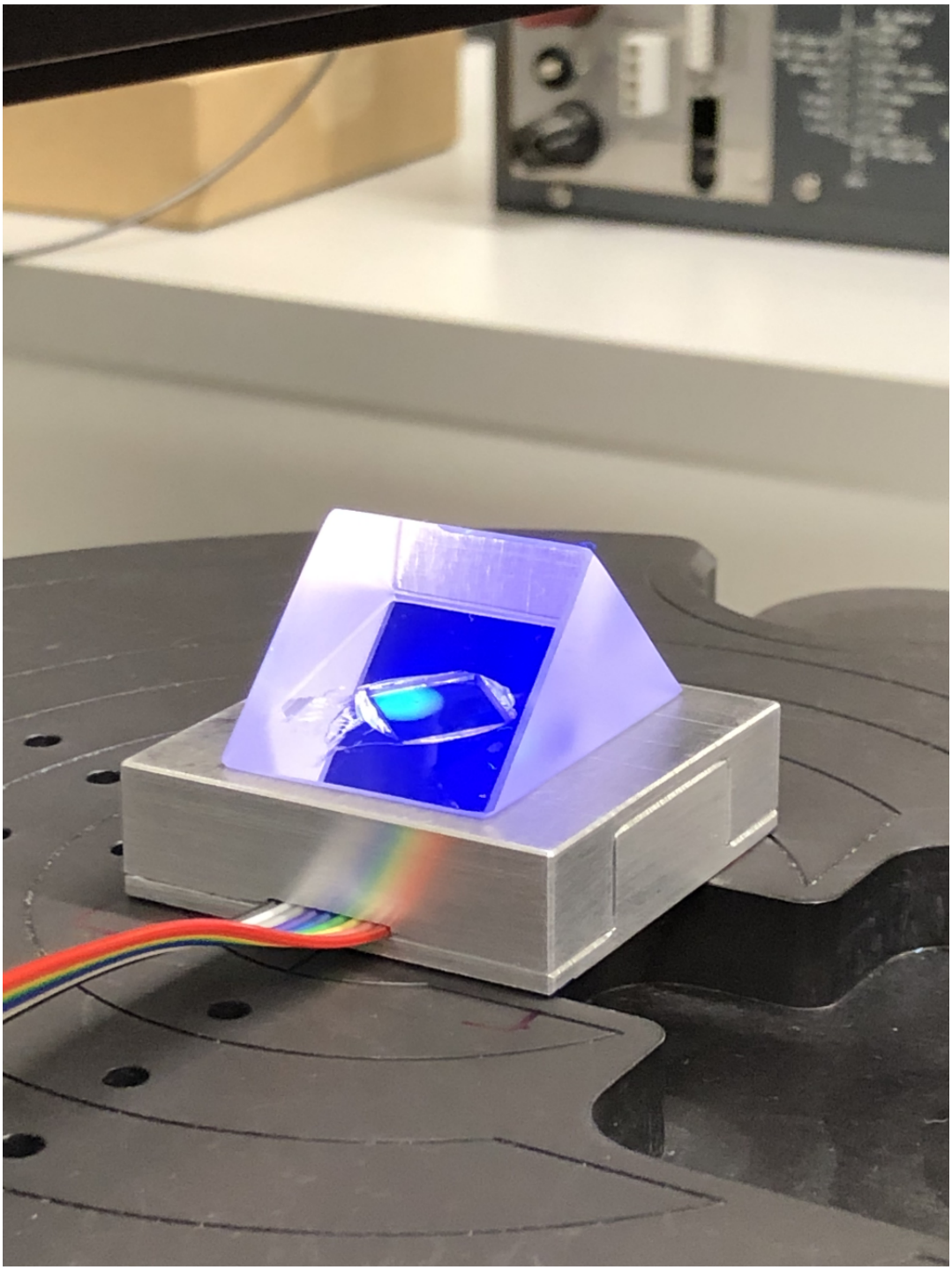

Figure 3.4: Photographed on the ellipsometer sample platform is a dimmable UV LED light stage built in-house. A square substrate was adhered with index matching gel to the bottom surface of a right-angle prism in the Kretschmann configuration. The UV light used to switch the SPO chromophores is turned on in this image. The bright blue spot is damage on the sample caused by UV overexposure while capturing the image.

the measurement of the full dispersion relation. Thus, the degree of coupling and Rabi splitting could change during the course of the measurement of all angles. In the end, the full angle sweep measurement has to be relatively fast compared to the backswitching rate of SPO.

Although some backswitching of SPO from the MC form certainly does take place during the < 10 min full angle sweep time, how comparatively fast or slow the backswitching process is quantified by a quick in situ measurement immediately after the full angle sweep. To ascertain the extent of backswitching taking place during the measurement of all angles and if it was changing the observed effects of possible coupling, the sample was measured from 45° to 85°, then immediately re-exposed to UV and only the angles from 55° to 65° were measured in about 90 seconds. This measurement could be compared to the results from the full sweep of all angles measured just moments before to determine the extent of backswitching and if it presented a problem.

3.9 Investigation of Tamm Plasmon Polariton & SPO Coupling in Tamm Setup

The Kretschmann setup discussed above provides the opportunity to investigate the coupling between surface waves (SPPs in the cases above) and excitons (SPO in the MC conformation). The use of a prism to channel the incident light into the metal + PS-SPO stack increases the incoming wavevector of the in-plane light, allowing it to launch SPPs on the metal layer. The prism, although useful for the above investigation, is not necessarily practical in any potential applications or investigative situations. The sample has to be adhered to the prism with sticky index matching gel; the overall system of prism + sample is bulky, considering that the layers of interest are on the order of tens of nanometers thick while the prism is several centimeters large; for prism re-use, the gel has to be cleaned off the fragile glass and possibly also substrates of potentially sensitive samples; measurement on the ellipsometer requires practiced, quick

and careful adjustments of the detector and stage height. All these factors detract from the easy applicability of the Kretschmann configuration for many measurements. A simpler and more straightforward investigative setup could offer benefits to the user as long as the prism is eliminated while keeping the effectiveness of potential switchable coupling between surface waves and excitons in a molecular plasmonic system. The idea of using a Tamm plasmon as the surface wave offers just such benefits without unnecessary drawbacks.

Tamm plasmon polaritons [12], [40], as described in the theory section, present an interface mode of light trapped at the boundary between a metal surface and an adjacent DBR. The standing wave formed at the interface can also be maintained when a spacer layer [38], here PS-SPO, is inserted between the opposing "mirrors". The great advantage that Tamm plasmons introduce in these studies are the ability of the right wavelengths of light incident on the sample from almost any AOI to enter and form a standing wave in the stack, regardless of the p- or s-polarization of the incident light. A prism is no longer necessary to launch surface waves, one component of the two coupling entities. Thus, the measurement setup is simplified immensely.

With Tamm plasmons forming a standing wave and SPO acting as the exciton component when switched to the MC conformation, the two components that can couple are present. The potential for coupling between the two is given as long as the components are in close proximity and the energies match. Here, the fabrication and analysis of a stack consisting of a DBR, a spacer layer, and a metal superstrate capable of supporting Tamm plasmons and incorporating switchable SPO chromophores will be described. This type of sample structure will be termed a "Tamm sample" or a "Tamm setup."

3.10 Preparation of Sample Series 3: DBR + PS-SPO + Ag

The objective was to create a 1-D distributed Bragg reflector (DBR) [35], [36], i.e., a multilayered structure, that would reflect a band of light frequencies particularly in the visible region. The structure would be made of two different dielectric materials deposited via physical vapor deposition (PVD) — specifically, RF magnetron sputter deposition [14], [47] from dielectric targets — with sufficient difference of refraction indices to produce a stopband of reflected frequencies wide enough to encompass the band of frequencies of the MC exciton. The reflection intensity of the stopband would also need to be great enough to allow easy detection of any peaks, yet the stack should require as few bilayers as possible to afford reliable and straightforward production in the laboratory despite the current lack of in situ deposition monitoring equipment as well as to avoid possible defect modes originating from stacks with many bilayers of somewhat varied thicknesses which could introduce defect ”dips” in the measured spectra (as described in Theory section). Control of the layer thickness is best done with in situ means, where constant monitoring during deposition allows the technician to stop the deposition process when the desired layer thickness is achieved. Without in situ methods, only calculations of deposition rates can be used to time the duration of deposition for each layer. Such a method of determining desired deposition duration is susceptible to any change in the deposition rate, however minor, during the deposition process, which in this case is often around 30 minutes long. Any rate deviation could ultimately lead to layers that are too thick or too thin, thereby shifting the central Bragg frequency of the desired stopband. The desired central Bragg frequency in this case was nearly 2.07 eV (around 600 nm wavelength), which was chosen due to the absorption spectrum of the switched SPO. It is in this region where coupling between the switched SPO excitons and Tamm plasmons would be observed. Deposition thicknesses of the respective TiO_2 and SiO_2 layers were 50 nm $\pm$5 nm and 120 nm $\pm$10 nm to place the

stopband appreciably over the central Bragg frequency, thus knowledge of the expected deposition rate and timing the deposition duration is mandatory. A schematic of the desired Tamm setup of a DBR stack together with a PS-SPO spacer layer and Ag on top is presented in Figure 3.5 with both simulation-determined layer identities and desired thicknesses.

Table 3.1: Design of DBR from simulations, with desired layer identities and thicknesses. Angle of incidence was chosen to be 55°. As deposition temperatures for TiO_2 are near room temperature and no heat treatment methods were employed, amorphous layers are to be expected.

Layer number	Layer material	Desired thickness [nm]
8	air	N/A
7	Ag	31
6	PS-SPO	200
5	TiO_2	50
4	SiO_2	120
3	TiO_2	50
2	SiO_2	120
1	TiO_2	50
0	glass cover slip	N/A

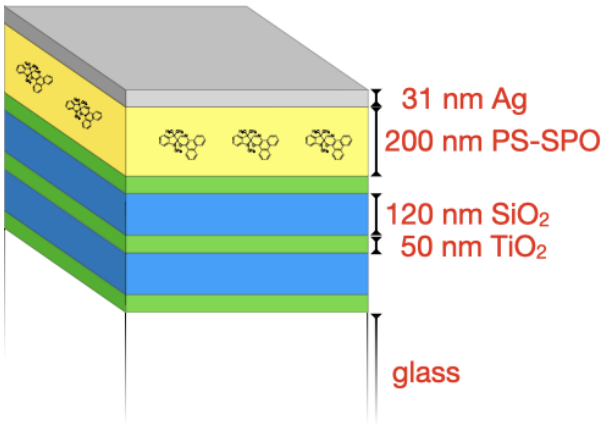

Figure 3.5: Schematic of Tamm setup. On a glass substrate, a simple DBR is deposited consisting of alternating TiO_2 and SiO_2 layers, a typical quarter-wavelength stack. Atop that is a PS-SPO layer with a Ag superstrate. Desired thicknesses from simulations are shown.

3.10.1 DBR Production

Since the deposition chambers are multi-use, the shutters and mounting pieces of the sputter deposition chamber needed to be cleaned of innumerable layers deposited over many months of operation by other researchers in order to avoid sample contamination. After extensive, electrically grounded sand blasting, the parts were reassembled and the preparation of two RF magnetron sputtering sources could be pursued.

The choice of RF magnetron sputtering was based not only on the necessity to avoid charging of the dielectric targets but also on the experience of the group engineer and the availability of equipment. RF magnetron sputtering is often used for non-conducting materials, such as the dielectrics to be used for the DBR, and prevents the buildup of charge on the dielectric target surface by alternating the polarity of the voltage, as discussed in the Theory section. In Figure 3.6, a schematic diagram is shown of the sources and sample stage setup along with a photograph of the deposition chamber itself.

The two target materials chosen for the alternating layers of the DBR were SiO_2 and TiO_2. They were chosen based on published values, respectively [74] and [75], that show the difference between the indices of refraction of the two dielectrics to be sufficient to permit a wide enough stopband for the intended purpose. The target disks were installed, one on each RF magnetron source (Figure 3.7), and measured 2.00 inches in diameter with a thickness of 0.125 inches for the newly purchased SiO_2 target (Kurt J. Lesker, reported values of 99.995% pure, part number EJTSIO2342A2, lot number GE-124 / VPU219337) and was somewhat thinner than that for the TiO_2 target, which had a minimal racetrack indicating previous use in the lab. The targets were installed with the necessary clearance of 1.5 mm between the magnetron's screw-on cap and the target surface according to the well-established relation between distance, type of working gas used and applied voltage (curve of Paschen's law); here, the working gas to be used during deposition was argon. The clearance is necessary to permit the flow of argon working gas into the chamber and to allow an electric arc to spark at the given breakdown voltage between the housing and the target mount and thus begin the

formation of the plasma.

Based on MATLAB transfer matrix method simulations[5], the DBR's layer materials and thicknesses were chosen (Table 3.1). In addition, the intended AOI for the DBR to be produced was chosen to be 55° as measured from the sample surface normal. The angle was chosen to give some flexibility for the measurement on the spectroscopic ellipsometer, which is limited to measurements between 45° and 90° with the current equipment setup.

To begin the deposition process, glass cover slips (Menzel #5, 20 x 20 cm, borosilicate glass, ~0.15 mm thick) were chosen as the substrate for deposition. Two cover slips were fixed to the sample stage with carbon tape (~2 x 2 mm) near the center of the substrate. After introducing the sample stage to the chamber load lock and pumping it down to about 10^{-6} mbar, the valve to the main chamber was opened and the sample stage moved from the load lock to the main chamber and inserted onto the stage mount. A shutter was placed over the sample stage to prevent deposition during the next steps of setting up the chamber for plasma ignition.

The first layer of the DBR could now be deposited. To ignite the plasma on the TiO_2 target, the flow of the argon working gas was increased to 200 sccm Ar and allowed to rapidly equilibrate to a chamber pressure of about 1.0 x 10^{-2} mbar. The target shutter was removed from the source by rotating the controlling arm. At that point, the RF power generator for the magnetron source was turned on for TiO_2 deposition of layer 1. To do that, the forward current was adjusted to 35 W and then the RF power switched on. The plasma ignited and glowed purplish blue. With the plasma lit, the pressure for the working gas during deposition was turned down to 100 sccm Ar, which lowered the chamber pressure to 5.4 x 10^{-3} mbar. The matching box capacitor settings were adjusted at first automatically and then manually to minimize the reflected power. The final settings were 30.5% for C_T, the tune capacitor position (tune circuit of inductor with variable capacitor in series), and 70.5% for C_L, the load capacitor position (load circuit with variable capacitor in parallel). With these settings, the reflected power was

[5]Again, Ron-Marco Friedrich wrote the majority of the MATLAB simulation code used here.

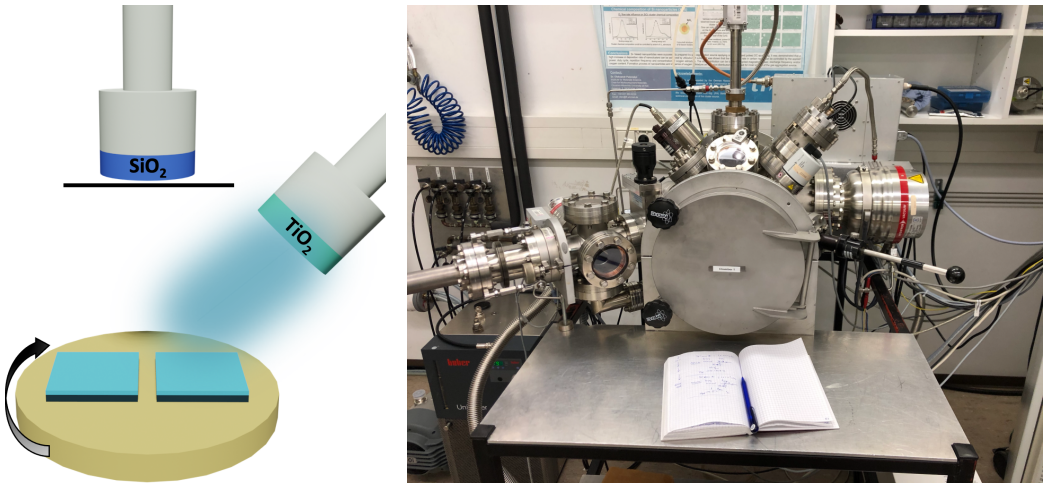

Figure 3.6: Schematic diagram[4] of sample stage with both dielectric target sources and their relative positions above the rotating sample. Photograph of deposition chamber used in these studies.

reduced to 0 W. The voltage bias was set to 154 V. The sample mount was able to rotate in order to reduce the effects of angled deposition, and the controller for the rotation was set to 7.5 V and 0.05 A with a resulting rotation speed of about 30 rpm. A thermocouple mounted in the stage was spring loaded and pressed up against the bottom side of the sample stage to measure its temperature directly. For layer 1, the stage temperature was 23.0 °C at the beginning of the run, however it must be noted that the carbon tape prevents contact between the sample stage and the sample substrate. In effect, the temperature of the sample cannot be accurately known and can only be approximated by knowing the temperature of the separated, underlying sample stage. In the case of the first layer, the temperature of the stage rose steadily to 29.2 °C during the deposition run. In any case, changes in temperature observed here on the order of ~10 °C are not relevant for the microstructure and properties of ceramics with melting temperatures far above 1000 °C, a value far above the temperatures seen here. So any temperature change experienced by the samples will not lead to any relevant change of the growth of the dielectric materials during deposition.

Based on preliminary deposition runs performed with the abovementioned settings,

[5]Schematic diagram created together with Salih Veziroglu.

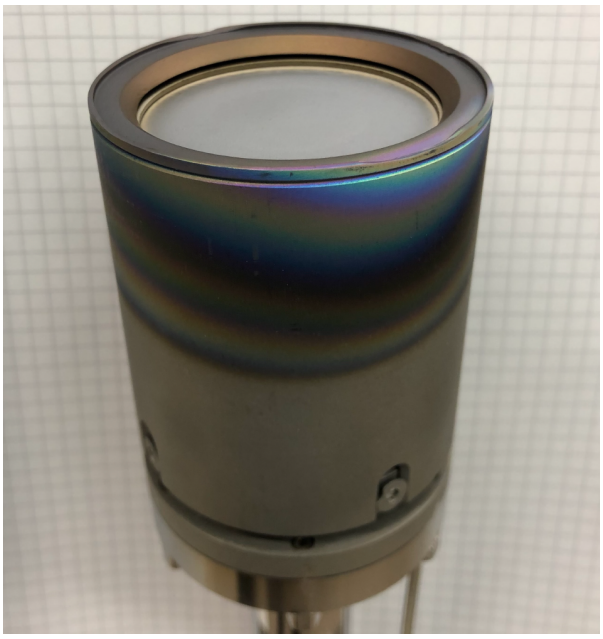

Figure 3.7: SiO_2 target with necessary clearance of 1.5 mm between outer housing and target mount (see black space above target surface) after use for several depositions. TiO_2 target was similar and is not depicted..

the deposition rate was determined to be approximately 1.6 nm/min. To achieve the desired 50 nm of TiO_2 for the first layer, a deposition time of 31 min 15 s was calculated. With stability achieved in the plasma and all settings, the shutter was retracted from above the sample substrate and the timer started. The progress of the deposition was monitored in person and found to be stable for the deposition of each layer with minimal changes in voltage bias, usually of no more than $\pm 1\,\mathrm{V}$, if at all. After deposition for a time of 31 min 15 s, the shutter was brought into place to cover the sample in the chamber and the RF power generator turned off. With that, the deposition of the layer was complete.

Once deposition had been completed, the thickness of the deposited layer needed to be determined by spectroscopic ellipsometry. The sample stage with the sample substrates (Figure 3.8) was removed from the chamber via the load lock. The samples will be referred to based on their relative positions on the sample stage as the 9 o'clock (at the left relative to the sample stage holder attachment) and 3 o'clock (at the right)

samples. There are no expected differences in the samples due to their relative positions around the center of the stage, and the names are only used to identify the samples and track them during the various steps of the deposition process.

Layers 2 through 5 were deposited in a similar fashion, however the settings for the SiO_2 layers were as follows: ignite plasma with working gas flow 240 sccm Ar; forward current 30 W; reduced gas flow 200 sccm Ar lowers chamber pressure to 1.0 x 10^{-2} mbar; matching network 38.1% for C_T and 83.2% for C_L; voltage bias 115 V; resulting deposition rate 3.0 nm/min for deposition time of 42 min. Before changing deposition material target, the power cable from the matching box was connected to the source to be used because only one RF power generator and matching network was available for use.

3.10.2 PS-SPO Deposition onto DBR

Once the DBR had been deposited and characterized on the spectroscopic ellipsometer, the next step was the deposition of a layer of PS with SPO mixed in. To deposit the desired layer thickness of PS-SPO, test experiments were performed to determine the proper deposition parameters.

First, two disposable samples of TiO_2 on glass cover slips were made to be used as substrates on which the PS-SPO solution would be spin coated. The deposition of the TiO_2 for these samples was based on the calculated rate of deposition of the first layer of the DBR. The total deposition time was 26 min 49 s with the following parameters: $P_{chamber}$ = 5.4 x 10^{-3} mbar, 35 W_f, 0 W_r, C_T 30.5, C_L 70.5, T_0 = 23.3°C, T_{end} = 28.9°C, and 155 V_{bias}. The disposable samples could now be used to test the thickness of the PS-SPO layer and tailor it with dilutions to reach a desired thickness of 200 nm, a value determined from simulations.

A PS-SPO solution needed to be made for the spin coating step. Based on previous experience with PS-SPO solutions, a 50-50 wt% PS to SPO solution was aimed for. Such a concentration could guarantee a high enough SPO content to make detection of

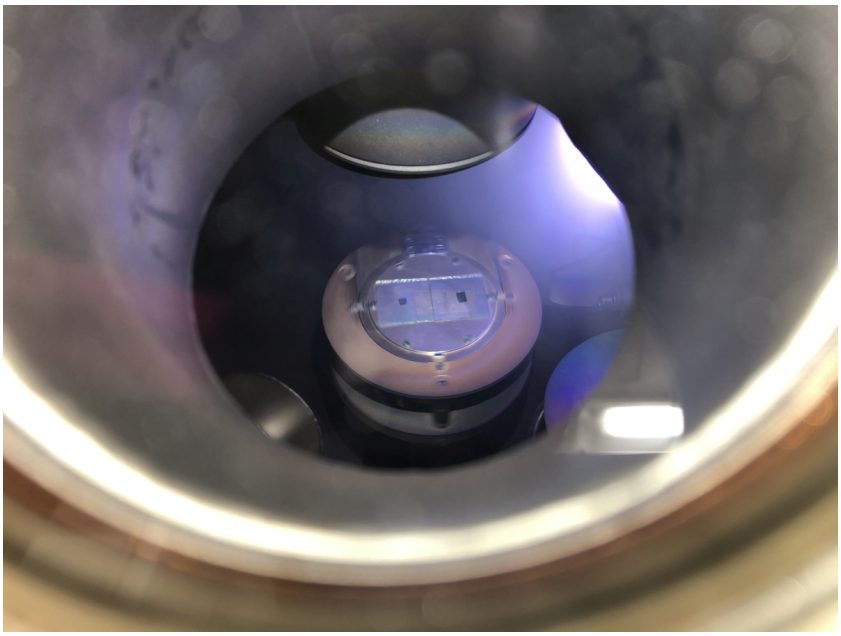

Figure 3.8: View of samples on stage through viewing window. The lit plasma of the TiO_2 target can be seen glowing top right. The SiO_2 source plus shutter can be seen top center. The black squares of carbon tape under the center of the substrates can be seen as well. The holder attachment is at the 12 o'clock position of the sample stage. Stage rotation around the stage center is clockwise.

coupling between Tamm plasmons and the MC excitons possible without the attendant aggregation of MC molecules at higher SPO concentrations seen previously by other researchers associated with the group. The PS-SPO would be diluted in toluene at a ratio of 5 wt% PS-SPO to 95 wt% toluene to permit spin-coating. Data was collected on the preparation of the PS-SPO and toluene solutions and an example can be seen in detail in the Appendix. After spin coating on TiO_2, the PS-SPO layer thickness could now be tested.

A solution named Jesse2 was spin coated onto the aforementioned disposable sample substrates in the following fashion. A 400 µL aliquot of Jesse2 (50-50 wt% PS-SPO in 95 wt% toluene solution) was first further diluted with 70 µL of neat toluene to create the solution Jesse2dil1. This diluted solution was used to pipette 250 µL onto the sample substrates. The resultant thicknesses of the PS-SPO layers for the two substrates were

247 nm and 243 nm, overshooting the desired thickness of 200 nm. To achieve a thickness for the PS-SPO photoswitchable cavity layer of 200 nm, the Jesse2 solution would be diluted with 100 µL of neat toluene instead of 70 µL. Since the objective was to achieve a layer thickness of about 200 nm, the final solution concentration was of secondary importance. Simply diluting the stock solution down to reach the desired thickness was straightforward and easy to accomplish.

The two disposable sample substrates were prepared for re-use by cleaning the just-deposited PS-SPO layer off by washing over the samples with fresh toluene (0.5 mL amounts) at least 4 times; then the substrates were placed on the spin coater, spun at 3000 rpm, and washed again 3 times with pipetted streams of 0.5 mL of toluene.

Starting with the freshly cleaned substrates, a 400 µL aliquot of Jesse2 was now diluted with 100 µL of neat toluene to create the solution Jesse2dil2. A 250 µL aliquot of this second dilution was pipetted onto the cleaned sample substrates. The resultant thicknesses for the two substrates were now 219 nm and 221 nm, overshooting the desired thickness of 200 nm slightly.

The disposable substrates were cleaned again as above and a 400 µL aliquot of Jesse2 was now diluted with 110 µL of neat toluene to create the solution Jesse2dil3. A 250 µL aliquot of this third dilution was pipetted onto the sample substrates and spun. The resultant thicknesses for the two substrates were now 214 nm and 212 nm, an acceptable deviation from the desired thickness of 200 nm. This would be the solution to be used on the previously produced DBR. Now these 2 disposable samples could be used to determine the correct parameters for the deposition of a Ag layer on top of the PS-SPO layer.

3.10.3 Ag Deposition on PS-SPO + DBR

A Balzers SCD 050 Sputter Coater chamber was used to test-deposit a silver layer on top of the PS-SPO layers of the disposable samples described above. Both disposable samples were placed in the instrument next to each other at the center of the sample

stage, which was set to a height of 6 cm. A silver target was installed. The system was pumped down to about 0.1 mbar, flushed with Ar three times, and allowed to pump down to a final pressure of approximately 0.04 mbar (the rudimentary LED display shows only approximate pressure on a logarithmic scale, here to a final value about halfway between 10^{-1} and 10^{-2} mbar). The pressure could be stabilized at the chosen value by means of a needle valve that could be set to bleed Ar into the chamber in a controlled manner. As a start, a 60 s sputter deposition time was chosen and the current was set to 30 mA. With the HV ON button, the plasma was ignited behind the shutter that prevented any deposition from taking place on the samples. The pressure increased immediately and was allowed to re-equilibrate down to the value mentioned above, and approximately 2 min were allowed to pass in order to remove the oxide layer from the surface of the Ag target and expose a fresh surface of Ag. Then the shutter was removed from the source target and the deposition timer started automatically to count down the 60 s deposition duration, at which time the sputterer shut off automatically. The chamber was flooded with air and the samples removed.

To know the Ag deposition rate, the thickness of the deposited Ag layer was determined with spectroscopic ellipsometry. One disposable sample at a time was placed on the stage in reflection mode at stage center with vacuum suction holding the substrate in place. The CompleteEASE software was used to choose the following parameters for the measurements:Three AOIs were chosen for measurement at 45°, 55°, and 65° measured from the sample surface normal. The measurement time for each AOI was 5 s. The data collected were Ψ and Δ, as described in the Theory section.

For fitting to the experimental data of Ψ and Δ, a software model composed of the following layers was constructed (from bottom to top): a cover slip substrate, a Cauchy layer for the unswitched PS-SPO layer, and a Ag layer. The cover slip reflects from both the top and bottom surfaces, but the reflections from the bottom surface complicate the modeling. As instructed by a representative of the manufacturer, J.A. Woollam, the use of cellophane tape with a translucent finish can reduce the reflections from the cover slip bottom side to a point where they become negligible. The tape was applied cleanly

by rolling it on with a thumb so as not to introduce air bubbles between the tape and glass. The tape must be translucent, i.e., frosted, so as to scatter the incident light and not reflect it cleanly into the detector. Since the polymer of the tape and the glass of the cover slip have similar indices of refraction near 1.5, applying the tape in effect acts like roughening the glass of the cover slip bottom side and causing incident light to be scattered. The difference in index of refraction between the two materials ensures very little light is reflected from their interface, enough to be negligible for the modeling.

Since the cover slip material had previously been characterized for the complex index of refraction on the ellipsometer and the PS-SPO layer thickness had already been determined after deposition, only the layer thickness and complex index of refraction for the Ag layer needed to be modeled. Upon fitting, the thicknesses of the Ag layers for the 9 o'clock and 3 o'clock samples were 12 and 13 nm, respectively, with MSE values of 15.927 and 12.241. Both samples had a very good visual fit between the measured data and the model. The deposition rate was determined to be 12 nm/min. Since the desired thickness was 31 nm (Table 3.1), an additional 95 s of Ag deposition was necessary. After completion of the additional deposition time, the thicknesses of the 2 samples were both 36 nm, an acceptable thickness. Therefore, the total deposition time for the Ag layer onto the completed DBR stack was to be 2 min 35 s.

Now all parameters for the deposition of the two layers (PS-SPO and Ag) on the DBR were known and could be used to prepare the final Tamm samples of DBR + PS-SPO + Ag. The parameters for the superstrate layers were as follows. **PS-SPO layer**: solution Jesse2dil3, 250 µL pipetted onto a stationary substrate for spin coating, accelerated for 6 s to a speed of 3000 rpm and spun for 1 min. **Ag layer**: 2 min 35 s deposition time at 30 mA current, from 2 min oxide-removed Ag target surface, ~0.04 mbar Ar atmosphere in chamber.

The two DBR samples that had previously been created were used for the deposition of the superstate consisting of a layer of PS-SPO at a desired thickness of 200 nm and a layer of Ag at a desired thickness of 31 nm (Table 3.1). After using the above-mentioned parameters for deposition of the PS-SPO layer and then the Ag layer, the

completed Tamm sample could be analyzed on the spectroscopic ellipsometer in both the unswitched and switched states.

3.11 Analysis of Sample Series 3: DBR + PS-SPO + Ag

For analysis on the spectroscopic ellipsometer, the Tamm samples (Ag on PS-SPO on DBR on glass substrate) just described could be placed on the sample stage of the spectroscopic ellipsometer, Ag side up. To switch the SPO chromophores in the PS-SPO layer, samples could be exposed from above, as with the sample series 1, to the light of a UV LED (365 nm) from a fiber optic cable fitted at the end with a wand that was positioned above the sample slightly off center (~10°) so as not to block the beam paths of incident and reflected light of the ellipsometer.

The sample was first measured in the unswitched state of the SPO. The unswitched Tamm sample was placed on the vacuum-assisted sample stage of the spectroscopic ellipsometer. As with the measurements of the Kretschmann system samples, the sample was measured at AOIs from 45° to 85° at 0.5° step intervals. Here, the total measurement time was just less than 7 minutes. Measurement was made easier with the Tamm setup because adjustments to the angle of the detector and the height of the sample stage were rendered unnecessary due to the lack of a prism, which had slightly complicated and slowed the measurement of the Kretschmann system samples.

After the unswitched SPO state of the sample had been measured across the entire dispersion relation, the SPO was to be switched to the MC form of the photochromic molecules and the full dispersion relation again measured from 45° to 85°. Switching the SPO was performed with the UV wand and the exposure time was about 40 s. The duration of UV exposure was determined here by measuring the splitting of the hybrid peaks at an AOI of 45° (not 57°, as in Kretschmann samples). The UV light was turned on and the splitting of the hybrid peaks was observed in situ. Once the peaks no longer

moved appreciably further apart and equilibrium had been more or less achieved, the UV LED was turned off and the entire dispersion relation, from 45° to 85° was measured in steps of 0.5°.

In the next chapter, the presentation of results from the experiments in this chapter will be presented: MATLAB simulations , PS-SPO investigations from ellipsometry, and both the Kretschmann and Tamm setups of switchable, interacting optical systems. The results will also be interpreted and discussed.

CHAPTER 4

Results & Discussion

4.1 Simulation Results

The simulations for this thesis were programmed[1] and run in MATLAB. See Figure 4.1 for a general impression of the coding editor workspace. Instead of showing the simulation results here, the individual results of simulations that are pertinent to the thesis are presented in the following sections next to the corresponding experimental results. This eases viewing and comparison between simulation and experimental results.

4.2 Results of Spectroscopic Ellipsometry

Spectroscopic ellipsometry [18] is used to probe the samples and elicit the dispersion relation both before and after molecule switching, thus both before and after coupling. However, the method also permits in situ observation of energy splitting during switching of the chromophores. The instrument [26] illuminates the sample simultaneously with light wavelengths from about 250-1700 nm, making measurements quick to perform. In less than 10 minutes of measurement time, an entire dispersion relation can be measured from an AOI from 45° to 85°.

To give an overview of data collected on the ellipsometer, three upcoming figures show the spectra of raw data, poorly fitted data, and excellently fitted data. The sample in question is a layer of switched PS-SPO (40 wt% SPO) on bulk Au on glass substrate.

[1] As previously noted, the MATLAB simulations conducted for this thesis were all based on code to a great extent written by a talented colleague, Ron-Marco Friedrich.

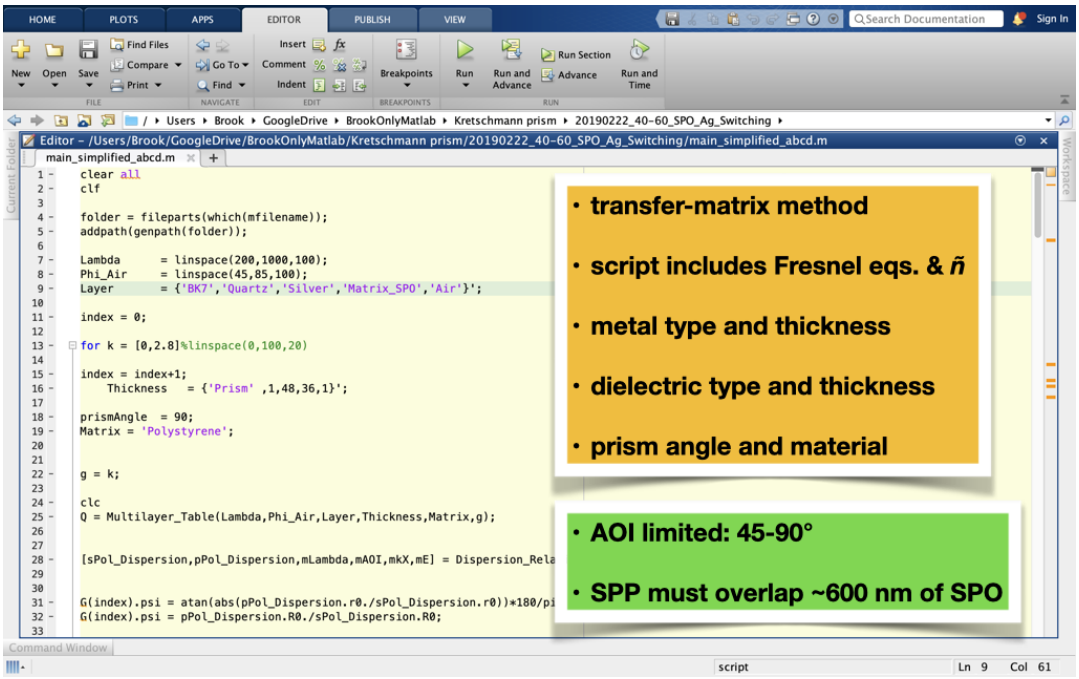

Figure 4.1: Screenshot of MATLAB programming to give a general impression of the Editor development environment and the details involved in simulations.

In Figure 4.2, the raw data is shown from 6 different angles of incidence ranging from 45° to 70° in 5° steps. Data from at least three angles is required to lend reliability to the fitting results, and at least three angles were measured in all sample data used in this thesis.

In Figure 4.3, a poorly fitted B-spline model fit to the data is shown. The resolution of the B-spline is too low (0.300 eV) to take account of all details in the data curves, and the MSE value is 53.875. The visual fit of the model data (black dashed curves) does not agree well with the raw data curves (all other colors).

Figure 4.4 shows an excellent B-spline fit to the same data as above. The resolution of the B-spline is great enough (0.100 eV) to account for all details in the data curves and results in an excellent visual fit between model data (black dashed curves) and raw data curves (all other colors). The MSE value is brought down to 18.221, a lower and better value than in the poorly fitted example.

As described in more detail in the Experiments chapter, the process of achieving a

good fit of a model-generated spectrum to the experimental data, and thus determining the optical constants and thickness of a layer, was performed as follows: first the thickness of the layer is determined by fitting in a transparent region (typically in the IR region over several hundred nanometers) with a Cauchy model layer. Once the thickness is determined and fixed, the model is parameterized with a B-spline of a set resolution (usually 0.300 eV or 0.100 eV) to fit model parameters to the experimental data in the visual and UV regions, down to < 300 nm. Much experience in modeling is of great benefit to the experimentalist in the challenge of overcoming the difficulties of developing a software model in the right way.

Upon finishing the modeling of the sample and fitting the model generated data to the experimental data by allowing the model parameters to be adjusted automatically, the n and κ values (Figure 4.5) can be calculated by the software as described in the Theory section. The quality of n and κ are determined by the modeling and fitting of Ψ and Δ.

4.3 Investigation of Optical Constants of PS-SPO

To begin investigations of the molecular plasmonic systems in these studies, the optical constants of the switchable chromophore used in these experiments, SPO, needed to be known. Samples of various concentrations of SPO in a PS matrix were made and their response to the incident light of a spectroscopic ellipsometer measured before switching in order to determine n and κ, the real and imaginary parts of the complex index of refraction, across all available wavelengths of the instrument. Afterwards, the SPO was switched by exposure to UV light, and the optical constants measured again in the same manner.

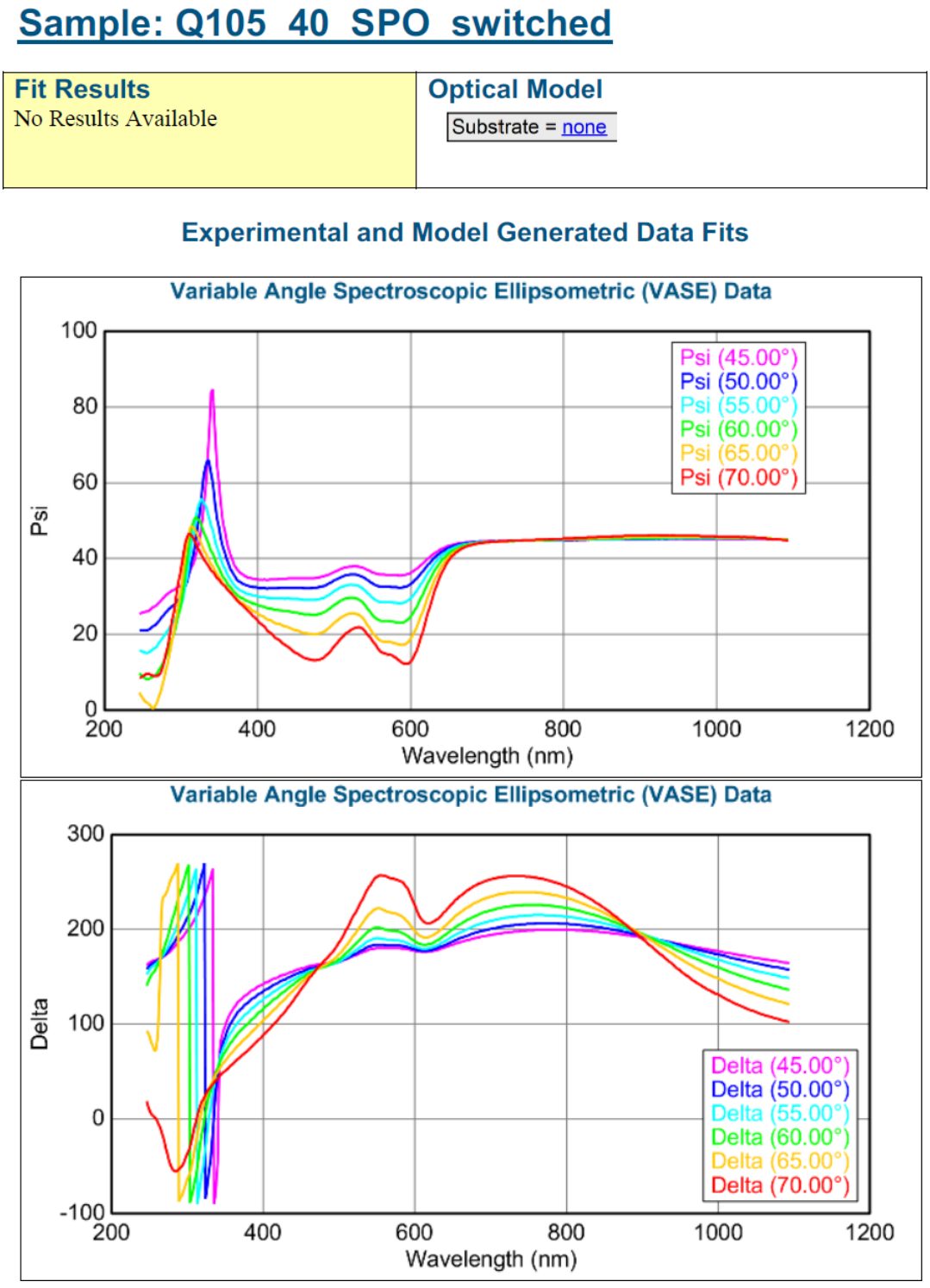

Figure 4.2: Raw, unfitted data. Representative image of Ψ and Δ measurements from different angles of incidence (legends) before modeling and fitting. Sample description: switched PS-SPO (60 wt% - 40 wt%) on bulk Au on glass substrate.

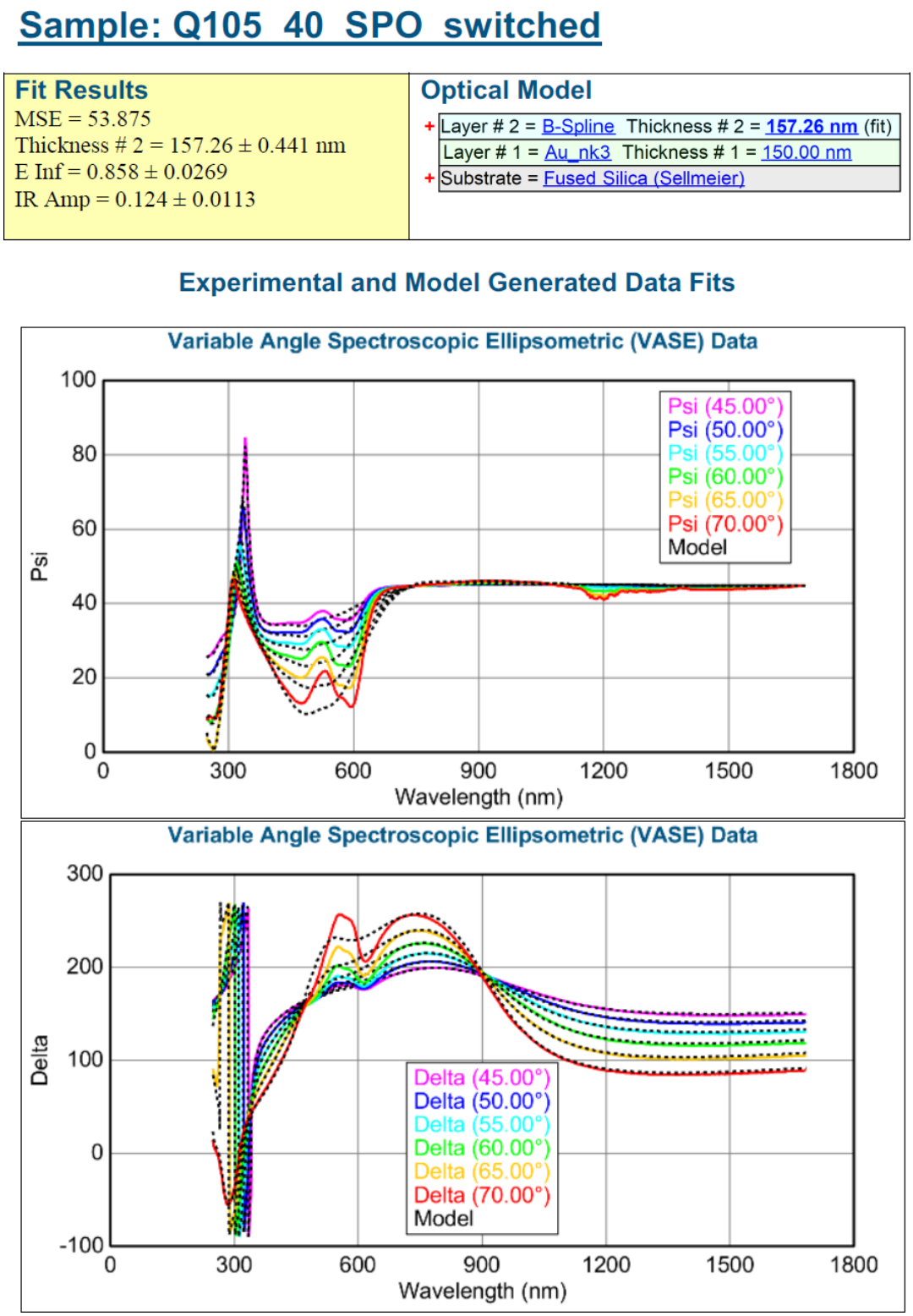

Figure 4.3: Unsatisfactory fit. Representative image of Ψ and Δ measurements from different angles of incidence (legends) after modeling and fitting with resultant MSE value of 53.875 and poor visual fit. Sample description: switched PS-SPO (60 wt% - 40 wt%) on bulk Au on glass substrate.

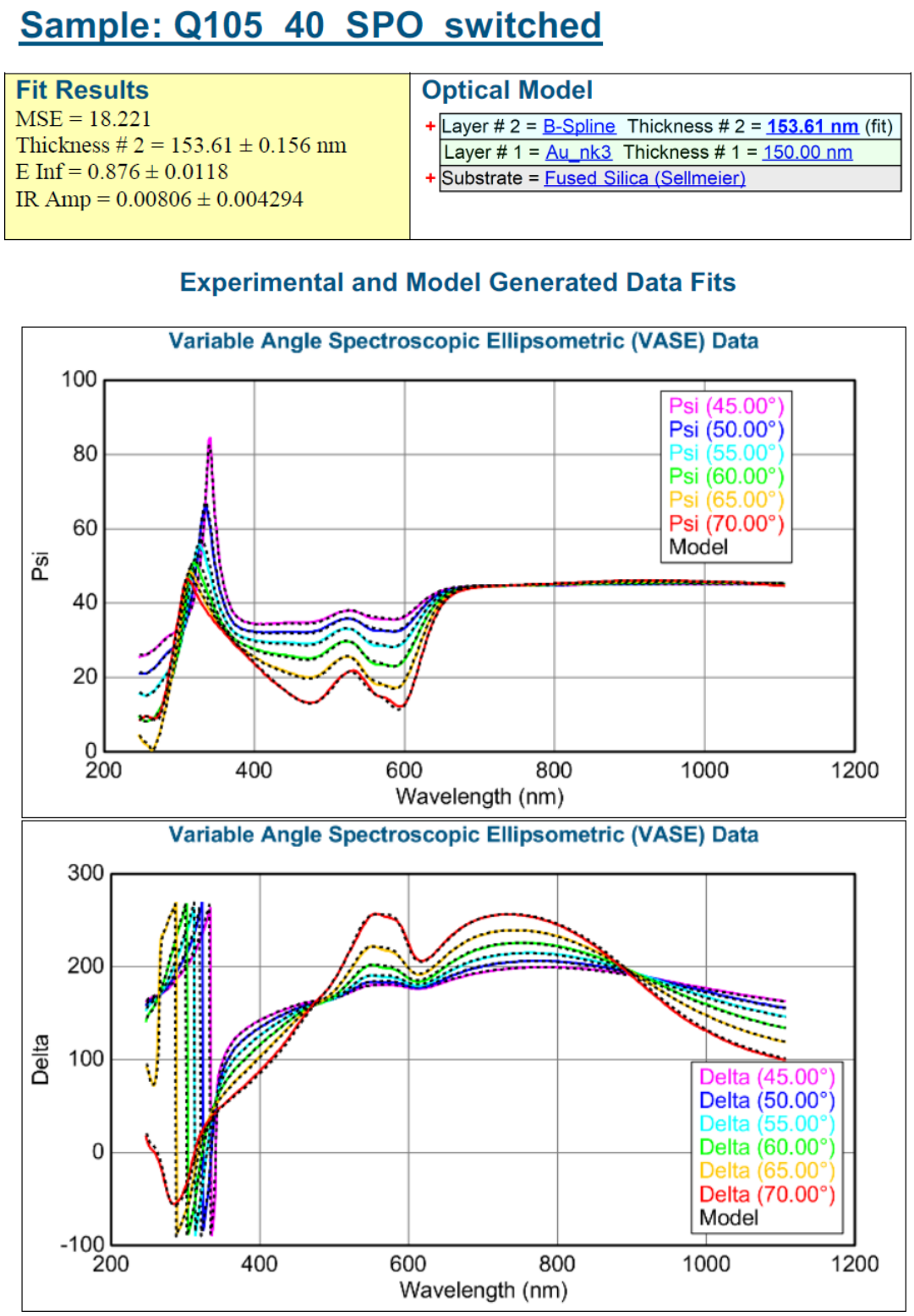

Figure 4.4: Satisfactory fit. Representative image of Ψ and Δ measurements from different angles of incidence (legends) after modeling and fitting with resultant MSE value of 18.221 and excellent visual fit. Sample description: switched PS-SPO (60 wt% - 40 wt%) on bulk Au on glass substrate.

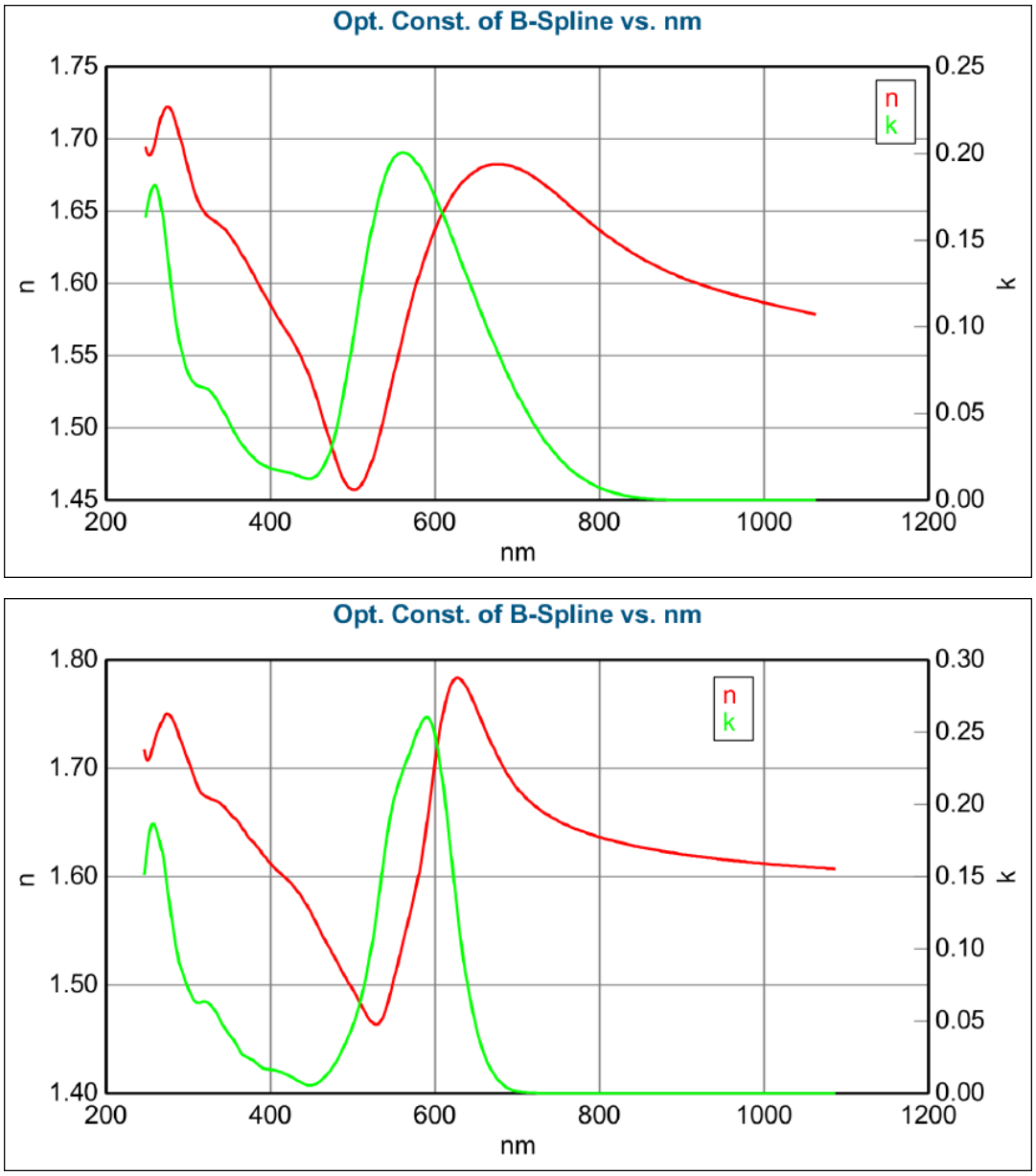

Figure 4.5: Comparison of resultant n (red) and κ (green) values for unsatisfactory fit model (top) from Figure 4.3 and those from an satisfactory fit model (bottom) from Figure 4.4. Although the n and κ values from both spectra are similar, only the values from the bottom spectrum can be considered reliable due to the visual fit and relatively low MSE value of the Ψ and Δ data in the preceding figures.

4.3.1 Results of sample series 1 for PS-SPO optical constants

In summary, layers of various concentrations of SPO in a PS matrix were made by spin coating onto bulk-Au-on-glass substrates, the gold serving to increase the reflected signal from the samples on the instrument of investigation, a spectroscopic ellipsometer. An LED with 365 nm UV light was used in these experiments to switch the SPO molecules from the leuco form to the MC form with an exposure time of 20 to 30 s. Once switched, the molecules absorb primarily in a lower energy region of the UV-Vis spectrum owing to the extended conjugation of the MC form. Before switching, the molecules absorb at around 365 nm, and after switching absorb additionally near 600 nm. Visibly, SPO also changes color upon UV exposure, from transparent before switching to deep blue after switching. In this way, switched SPO is often described by the term chromophore, a chemical species possessing color.

For the various weight percent concentrations of SPO of different samples with a PS-SPO layer on bulk Au, the optical constants, n and κ values across all wavelengths, were to be determined from data collected on the spectroscopic ellipsometer. After sample production on a spin coater and subsequent measurement on the spectroscopic ellipsometer, the thickness of the layer was accurately determined in the IR region of the spectrum and its value subsequently fixed in the model of the stack. Then the optical constants for the PS-SPO layer could be determined by fitting the model parameters to the measured data across all wavelengths of interest in the CompleteEASE software of the instrument.

The thickness of the PS-SPO layer first had to be determined accurately before the n and κ values for the layers of different SPO concentrations could be modeled. As described in detail in the Experimental section, fitting was performed at wavelengths above ~650 nm to determine the thickness of each sample's PS-SPO layer. For each weight percent concentration of the different PS-SPO layers, see Table 4.1 for the quality of the visual fit, the MSE values and the thickness of the PS-SPO layer.

Table 4.1: Thickness d determined via spectroscopic ellipsometry of PS-SPO layers of varying SPO wt% content, with description of confidence in visual fit from experienced user and software calculated mean squared error values.

Sample [wt% SPO]	Confidence in visual fit	MSE value	PS-SPO layer d [nm]
0	very good	42.152	199
20	excellent	32.164	175
40	excellent	18.221	154
50	very good	37.997	133
60	excellent	19.141	130
100	very good	38.341	90

After the thickness of the PS-SPO layer had been fixed by analysis in the IR region, fitting was expanded below ~650 nm for Ψ and Δ via a B-spline fit made of many fitting points across all wavelengths. See Figure 4.2 and Figure 4.4 for example spectra, respectively before and after fitting, of Ψ and Δ for a layer of PS-SPO (ratio of 60-40 wt%). The sample is a stack of PS-SPO (thickness: 154 nm) on bulk Au on a glass substrate.

As soon as the fit of Ψ and Δ across all wavelengths was acceptable by a visual comparison of the fit between the results of the model and the measured data, the MSE value could be made note of and the n and κ values calculated by the software for all measurable wavelengths (e.g., see Figure 4.5).

The process of determining the thickness in the IR region and subsequently replacing the Cauchy fit with a B-spline fit for wavelength below ~650 nm was performed for the samples listed in Table 4.1 above. The resulting modeled complex index of refraction, n and κ, for the PS-SPO layer — and only the PS-SPO layer — for several samples of differing SPO weight percent concentrations can be seen in Figure 4.6. The inset photos show PS-SPO both before and after switching, albeit without the underlying bulk Au layer, the absence of which makes the color change more easily visible in photographs. The findings compare well with similar published spectra available in the literature [4], [6], [76]–[78].

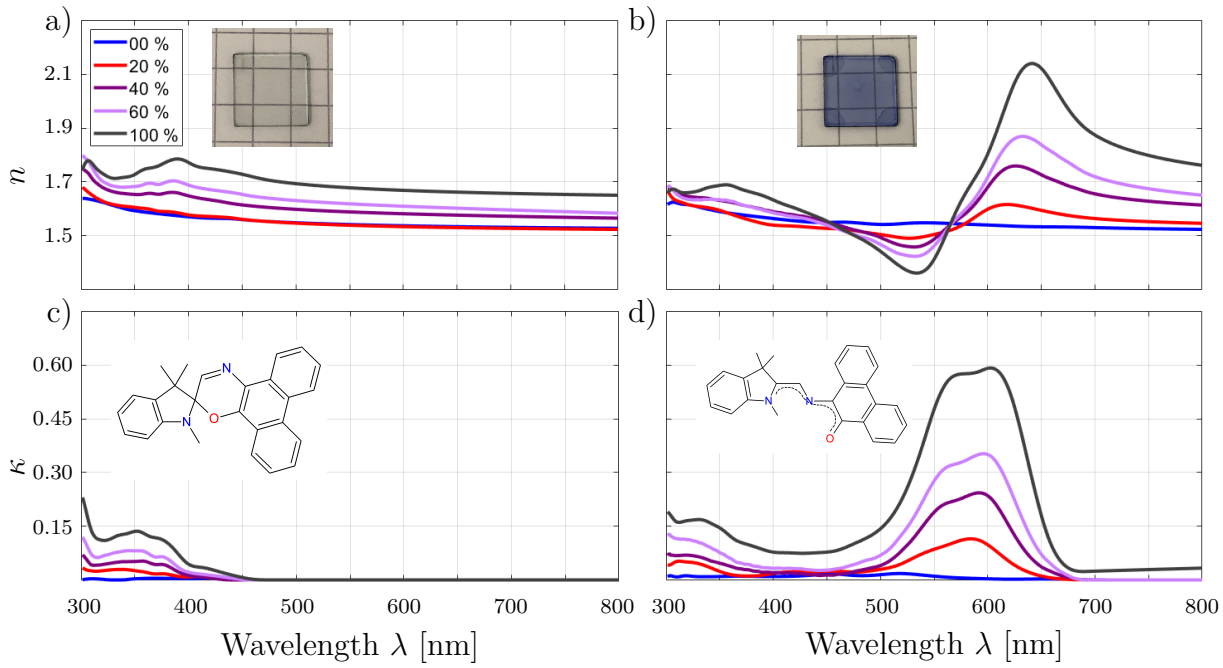

Figure 4.6: Complex index of refraction values of n (a and b) and κ (c and d) for unswitched (a and c) and switched (b and d) thin film samples of a PS matrix with differing weight percent amounts of SPO mixed in (legends). Spectra obtained from PS-SPO layers deposited on 150 nm Au base layer. SPO skeletal formulas shown. Inset photos show 1 cm^2 quartz substrates with a PS-SPO (60 wt%) layer both unswitched and switched without Au base layer to make color more visible. Darker corners result from edge effects of spin coating process; measuring at sample center makes corner effects irrelevant.

4.3.2 Discussion of sample series 1 for PS-SPO optical constants

In brief, clear evidence of the formation of new molecular oscillators resulting from the conformational change of the SPO molecules to the MC form is seen. For the unswitched molecules, normal dispersion of n across almost all wavelengths is evident in Figure 4.6 a, and the κ values show absorption around 350 nm, seen in Figure 4.6 c. Once switched, anomalous dispersion of n near 600 nm is apparent in Figure 4.6 b, and κ values in Figure 4.6 d exhibit newly present absorption of the MC conformation. It is the changes in

the dispersion relation associated with the conformational change of the SPO molecules upon UV exposure that make possible the switching of coupling between surface waves and excitons described later in this thesis.

A brief description of normal and anomalous dispersion is in order [25]. The general trend for n in the unswitched molecules is a gradual increase in n towards shorter wavelengths. This general behavior is typical for transparent dielectric media and is known as normal dispersion. It is due to absorptions certain to be present in the UV region of the spectrum, even though the resonance frequency of those absorptions may be below the range of wavelengths measurable with the spectroscopic ellipsometer used here. Shorter wavelengths are closer to UV resonance frequencies and therefore interact with the sample with greater oscillator amplitudes, a result typical of all resonance phenomena. The switched SPO molecules, however, exhibit anomalous dispersion; that is, moving towards shorter wavelengths leads to decreasing n, often dramatically so around the resonance frequency, here present near 600 nm. Anomalous dispersion is sometimes therefore also referred to as resonance dispersion. With this in mind, normal dispersion seen in a region of a spectrum goes together with anomalous dispersion at some wavelength further below that region.

In the unswitched SPO molecule, conjugation is found in two isolated moieties on either side of the spiro carbon (Figure 4.6 c). However, once switched to the MC form, the conjugation of the molecule is extended continuously across the entire molecule (Figure 4.6 d), thus leading to absorption at a longer wavelength [3]–[5], [44]. The molecule in the MC conformation can absorb light at about 600 nm, leading to the promotion of an electron. Such a molecular orbital transition can be accurately referred to as an Frenkel exciton, an excited state where the promoted electron and generated hole are in one and the same molecule. The resultant exciton will act as one partner in the system of coupled oscillators to be described later.

In a closer look at the graphs in Figure 4.6, there is a marked difference between the unswitched samples (left graphs) and the switched samples (right graphs). The extinction coefficient, κ (bottom graphs) of the samples display regions of definite ab-

sorption by the PS-SPO layer. The absorption between about 300 nm and 400 nm is attributable to the unswitched leuco form of the closed-ring molecules of SPO. Because such absorption can be seen in both the unswitched and switched samples, it is apparent that not all SPO molecules were switched to the MC, open-ringed form. In effect, an equilibrium state between the two different molecular configurations was reached by in situ measurements while switching with UV light (not shown). Here, exposure to UV light lasted about 2 minutes to ensure a stable equilibrium point was reached between switched and unswitched molecules, and exposure to UV was maintained during spectroscopic ellipsometry measurements so that no backswitching could take place during measurements for the determination of the optical constants.

The real part of the index of refraction n can be seen in the top graphs for both unswitched and switched samples. The value for the switched molecules at the right exhibit the typical line shape of a dipole oscillator. With increasing wavelength, the n value of the switched, MC form of the SPO first dips, then peaks, and finally plateaus at a slightly higher value than where it began. The dip and peak form a pair that approximately centers on the resonance frequency of the dipole oscillator, here about 600 nm in the case of SPO. The peak in the complex part of the index of refraction κ also approximately centers on that same resonance frequency. The higher n values for higher wavelengths as compared to lower wavelengths can be explained most easily by the frequencies of the light and the available molecular polarization mechanisms. Light of frequencies far below the resonance frequency of the dipole (high wavelengths) can easily spur electron polarization in the molecules, and the polarization mechanism is available to the system. But far above the resonance frequency (low wavelengths), the electrons can no longer respond to the excitation frequency and the electronic polarization mechanism of the molecules ceases to be available to the system. Since polarization in effect leads to changing the index of refraction of the material, wavelengths greater than the resonance frequency show greater values of n than wavelengths below the resonance frequency of the dipole.

Now the results from different concentrations of SPO in the PS-SPO layers should

be compared. The general trend within the unswitched n values is an increase of n across all wavelengths, in general lowest for 0 wt% SPO and greatest for 100 wt% SPO. This is to be expected: the greater the content of SPO molecules, the greater the index of refraction of the PS-SPO layer; as the SPO concentration increases from 0 wt% to 100 wt%, the index of refraction moves from that of PS to that of SPO. There is a definite increase from 20 wt% to 40 wt% to 60 wt% SPO content. The similarity and even reversing of behaviors between 0 wt% and 20 wt% can be explained by the difficulty in modeling such optical constants. Such modeling is not an exact process and some inaccuracy and variability exists in the output depending on the quality of the model fitting.

The peak in the extinction coefficient κ shows asymmetry, especially apparent in the sample of 100 wt% SPO. The source of the asymmetry can be theorized to be exciton coupling, as in Berova, et al. [79] and also Eakins, et al. [80]. Coupling between the electronic transition dipole moments of the switched chromophoric molecules with sufficient proximity and appropriate relative orientation leads to splitting of the energy associated with excitation. The result is "exciton splitting," also known as Davydov splitting, and the absorption shows asymmetry [80]. Asymmetry of the peaks due to Davydov splitting is defined as "the splitting of bands in the electronic or vibrational spectra of crystals due to the presence of more than one (interacting) equivalent molecular entity in the unit cell." The interaction of transition dipoles leads to large rotational strengths and preferred relative orientation of the molecules. When having the correct relative orientation, such allowed electronic transition dipole moments of switched SPO molecules in proximity can couple. The interaction of such degenerate, excited states leads to a splitting in the transition energies, which results in asymmetry of the resonance behavior of the composite PS-SPO. And although it is a type of coupling, it is not the coupling of interest in this thesis.

4.4 Investigation of SPP & SPO Coupling in Kretschmann Setup

With the optical constants having been determined for various weight percent concentrations of PS-SPO layers, simulations were used to determine the parameters for investigations of samples in the Kretschmann setup [2], [31]; that is, using a prism to couple light into the molecular plasmonic system and create surface waves, here as SPPs in the metal layer (see schematic in Figure 3.3 and image in Figure 3.4). With that, the conditions for coupling between surface waves and excitons of SPO are then given.

In summary, the prism in the Kretschmann configuration alters the momentum vector of the incident light from a spectroscopic ellipsometer source, thus making possible the excitation of SPPs at the metal–dielectric interface of the attached sample [2]. The dielectric is mixed with the photoswitchable chromophores of SPO, which upon exposure to UV light switch to the MC conformation and form excitons upon absorption of the energy of light with the appropriate wavelength (near 600 nm). With sufficient proximity and similar energies, the evanescent waves of the SPPs and the excitons of the switched SPO can couple and form hybrid states [11], frequencies that no longer match the natural frequencies of the independent entities. The new hybrid frequencies are distinct and separated on the frequency scale, a separation termed Rabi splitting. The degree of Rabi splitting that will be presented is in the ultrastrong regime.

For the first time in a Kretschmann setup, the off/on all-optical switching of coupling between SPPs and excitons via the use of photochromic molecules is shown. The Rabi splitting of hybrid mode peaks is even made dynamic with the use of in situ methods to observe peak movement during UV-induced molecular conformational change creating excitonic species capable of coupling.

4.4.1 Results of sample series 2: PS-SPO + Metal + Prism

In brief, samples were fabricated on a quartz substrate with a superstrate consisting of a sputtered metal layer (Ag or Au) of a thickness that was chosen based on simulations, on top of which was spin coated a dielectric layer of PS-SPO, also of a simulation-determined thickness. The sample layers were measured after deposition via spectroscopic ellipsometry, always carefully making sure that the visual fit of the model-generated data and the measured data were in good agreement. Once that condition was met, the MSE value of the fit was made note of. In Table 4.2, the values from the depositions and thickness measurements of the metal and the PS-SPO layers for two samples are reported, along with the attendant MSE values of the ellipsometer model fits.

Table 4.2: Results of sample series 2: metal deposition times, resultant thicknesses together with mean squared error values from ellipsometry; PS-SPO resultant thicknesses together with mean squared error values.

Metal	Metal depo. time [s]	Metal d [nm]	MSE	PS-SPO d [nm]	MSE
Ag	220	48	15.104	36	4.989
Au	250	49	9.706	35	9.252

The Ag/PS-SPO sample was adhered to the right-angle prism with index matching gel and the setup subsequently placed on the housing for the UV LED to bring the sample into position for spectroscopic ellipsometry measurements. Left unexposed to UV light, the dispersion relation (AOIs from 45° to 85° in 0.5° steps, for a total of 81 angles with 5 s data collection per angle) was measured. The Figure 4.7 shows the results of the measurements along with the result of the simulation.

The dispersion relations, both simulation and experiment, for SPPs at an interface of Ag and unswitched PS-SPO are shown in Figure 4.7. The typical energy vs. momentum relation of dispersion curves is shown here as incident light wavelength (energy equivalent) vs incident light angle (corresponding to the momentum equivalent k_x vector, i.e., the in-plane component). The spectroscopic ellipsometer strikes the sample simultaneously with a multitude of incident light frequencies and can scan a sample stepwise from

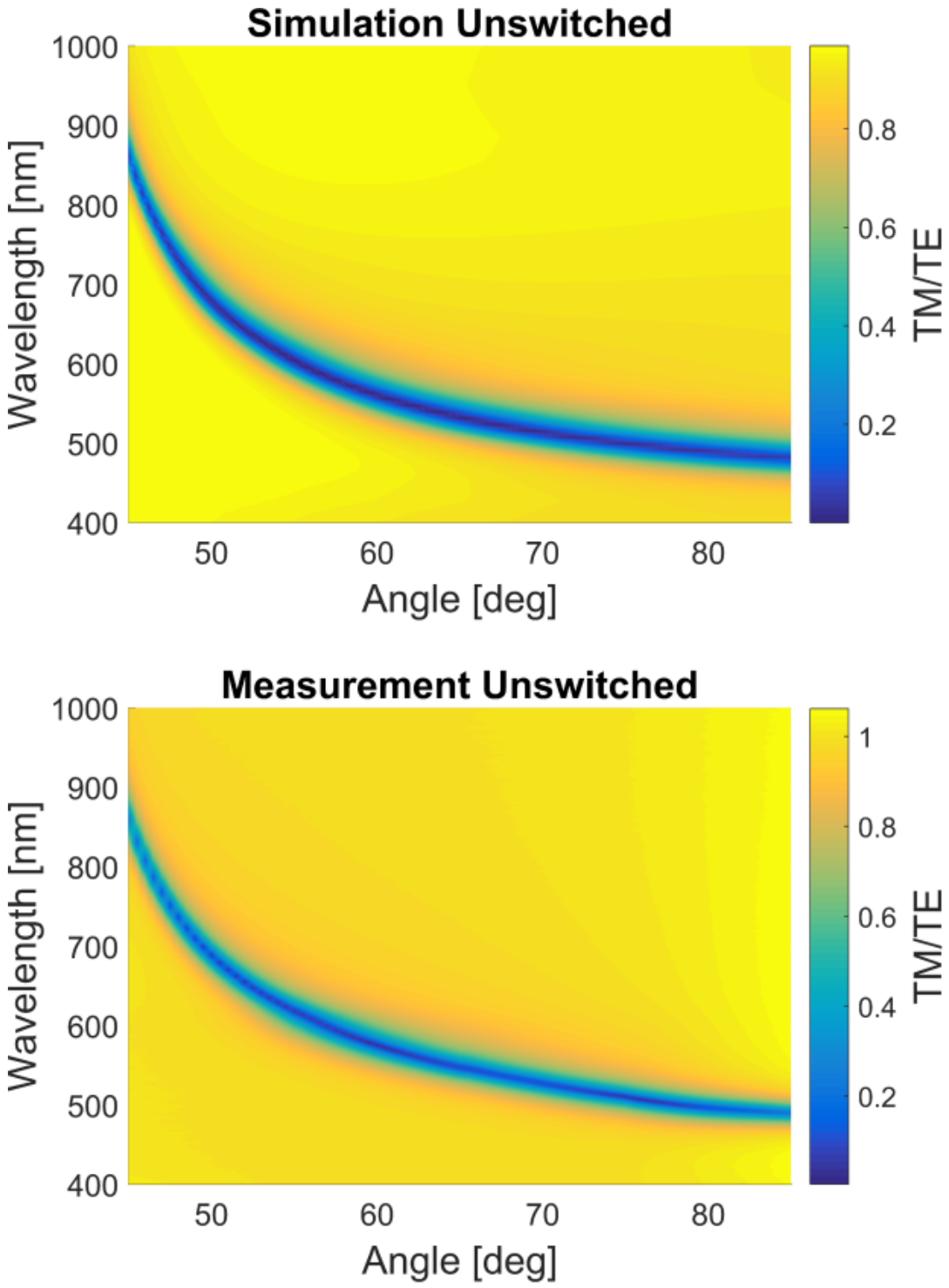

Figure 4.7: Dispersion relations for 48 nm layer of Ag covered with 36 nm layer of PS-SPO (60 wt% SPO) for top graph simulation unswitched, and bottom graph measurement unswitched. Wavelength correlates to energy of incident light and angle correlates to wavevector in plane of sample, k_x. See text for discussion of TM/TE scale. The unswitched sample shows the dispersion relation for the SPPs alone. Total measurement time from 45° to 85° is less than 10 min.

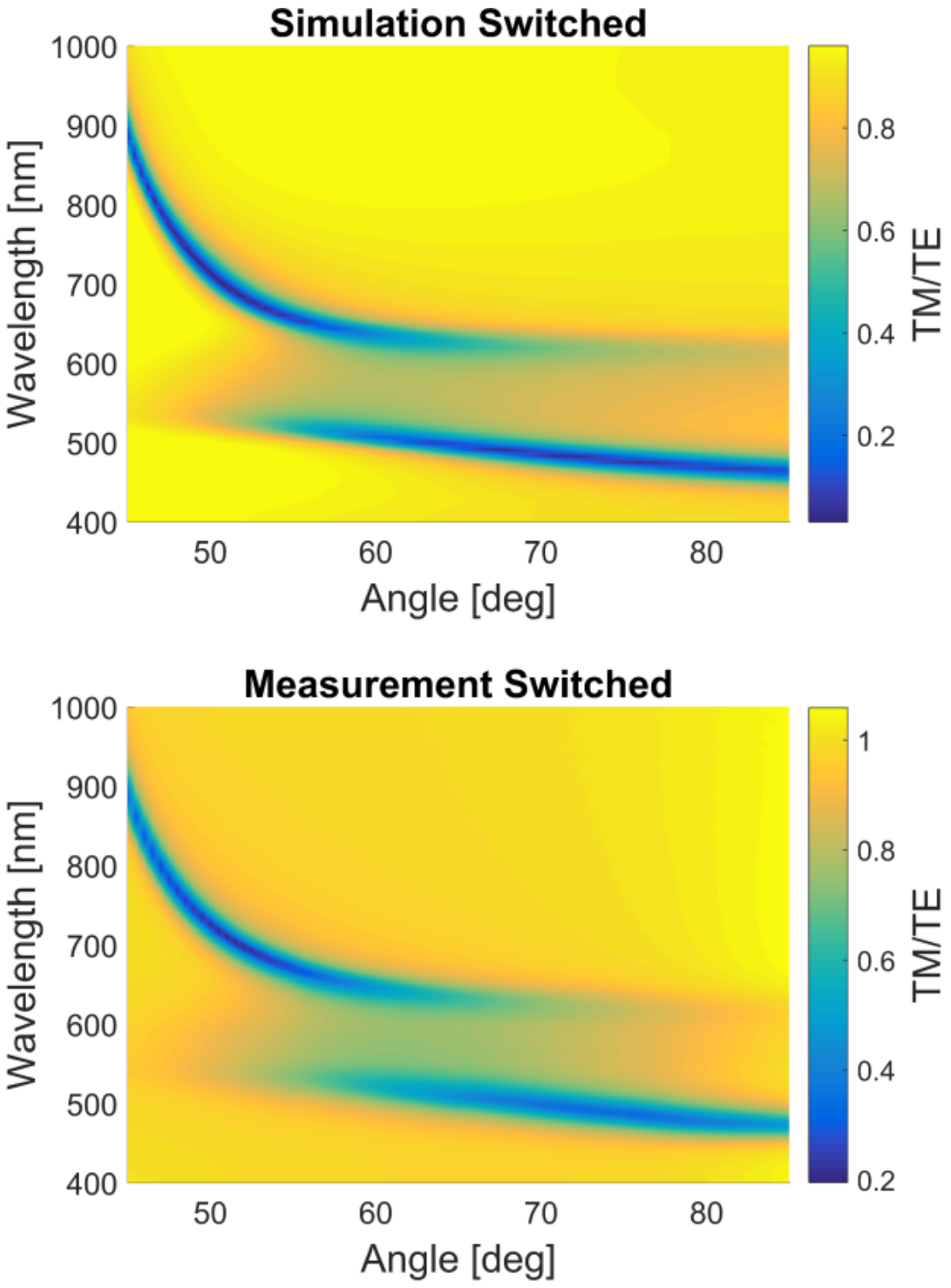

Figure 4.8: Dispersion relations for 48 nm layer of Ag covered with 36 nm layer of PS-SPO (60 wt% SPO) for top graph simulation switched, and bottom graph measurement switched. Wavelength correlates to energy of incident light and angle correlates to wavevector in plane of sample, k_x. See text for discussion of TM/TE scale. After the sample is exposed to 365 nm light for < 30 s, the switching comes into equilibrium and the avoided crossing due to coupling between SPPs and merocyanine SPO is clearly seen. Total measurement time from 45° to 85° is less than 10 min.

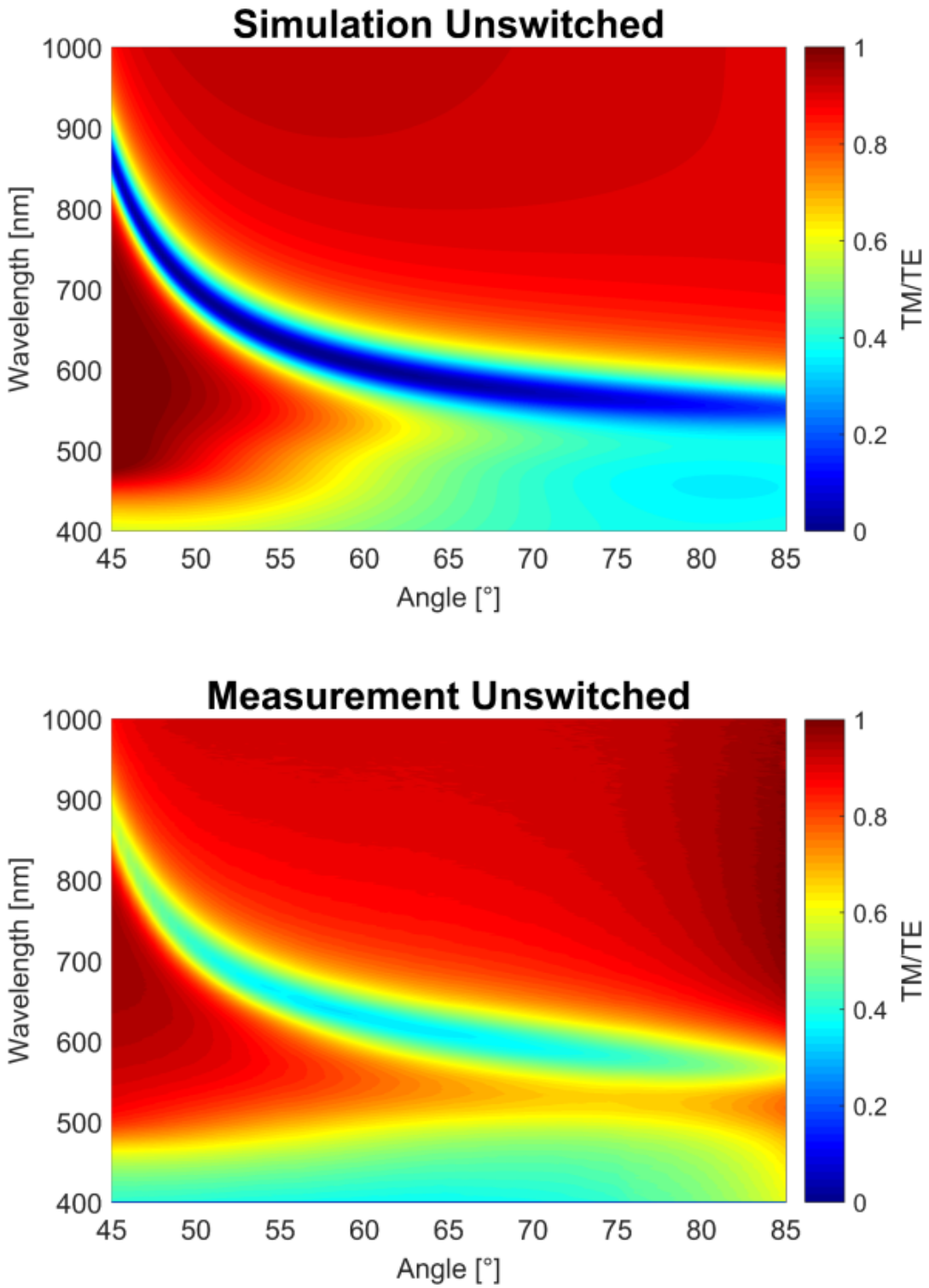

Figure 4.9: Dispersion relations for 49 nm layer of Au covered with 35 nm layer of PS-SPO (60 wt% SPO) for top graph simulation unswitched, and bottom graph measurement unswitched. Wavelength correlates to energy of incident light and angle correlates to wavevector in plane of sample, k_x. See text for discussion of TM/TE scale. Compared to similar graphs for Ag layer in previous figures, the linewidths are wider due to higher damping in Au.

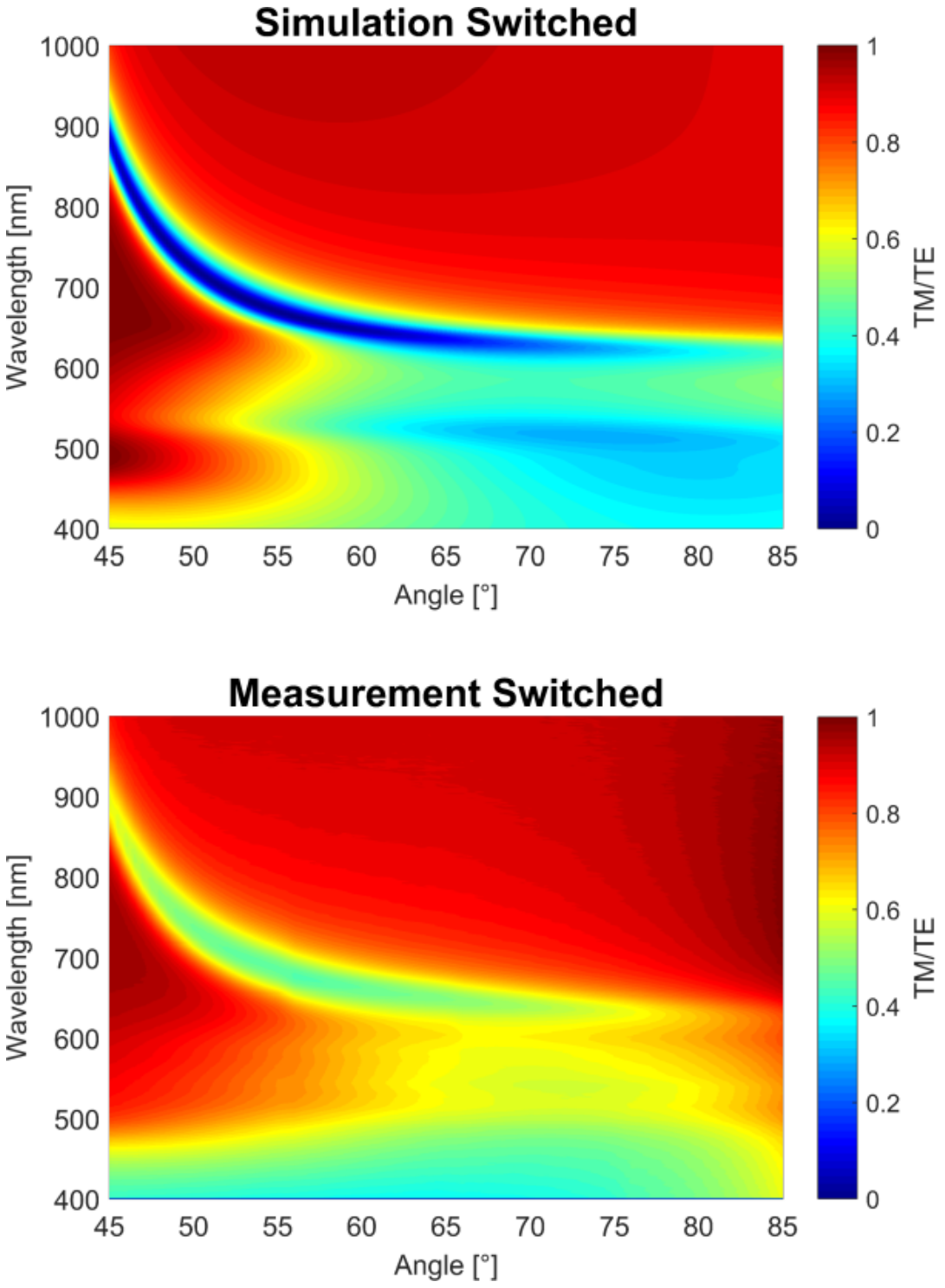

Figure 4.10: Dispersion relations for 49 nm layer of Au covered with 35 nm layer of PS-SPO (60 wt% SPO) for top graph simulation switched, and bottom graph measurement switched. See text for discussion of TM/TE scale. Compared to similar graphs for Ag layer in previous figures, the linewidths are wider due to higher damping in Au. The lower branch of the avoided crossing is obscured by the absorption of Au below 500 nm. Nonetheless, coupling is still evident. Color scheme chosen to highlight subtleties.

45° to 85° AOI, thereby altering the light momentum's k_x vector. The referenced plots display on a TM/TE scale, thus showing the absorption of incident light which launches SPPs. As previously mentioned in the Theory section, s-polarized light (TE) cannot couple to plasmons but p-polarized light (TM) can, so plotting TM/TE normalizes the data to account for the changing light intensity due to a changing incidence angle [34].

Next, the sample was exposed to UV light from the LED mounted below the sample in the metal housing (Figure 3.4) for a period of time between 20 and 30 s. During this time, the sample was observed in situ at an AOI of 57° to watch the splitting of the hybrid peaks until the peaks no longer moved apart, at which point the UV LED was turned off and the entire dispersion relation was measured from 45° to 85° in 0.5° steps in < 10 min.

With the SPO switched to the MC form, the dispersion relations, both simulation and experiment, for SPPs at an interface of Ag and PS-SPO are shown in Figure 4.8, with the same axes as in Figure 4.7 and the same TM/TE scale.

The next Kretschmann setup to be measured had the Au/PS-SPO sample adhered to the right-angle prism with index matching gel and placed on the LED housing with the UV light kept off. Measurements were taken from 45° to 85° in 0.5° steps for a total of 81 angles with 5 s data collection per angle (Figure 4.9). Subsequently, the UV light was turned on while the splitting of the hybrid modes was observed in situ at 57° AOI until movement of the peaks was no longer appreciable, about 20 to 30 s, at which point the UV light was turned off and the entire dispersion relation measured once again. As with the Ag sample, Figure 4.9 shows the results of the switched PS-SPO simulations and measurements, now with Au as the SPP-hosting metal.

4.4.2 Discussion of sample series 2: PS-SPO + Metal + Prism

To begin the discussion, the UV exposure time should be explained. The in situ measurement at 57° AOI during which the samples were exposed to UV light showed the

growing separation of two peaks over a period of time of about 20 to 30 s. At this point, the peaks slowed to an almost cessation of movement. This indicated that an equilibrium state between unswitched and switched SPO molecules had been reached at that particular UV light intensity and SPO concentration. More will be shown in this regards in an upcoming section regarding the in situ viewing of peak separation. With equilibrium reached, the UV light was turned off and the entire dispersion relation measured.

There is one point to be made about the nature of the coupling being discussed. Whereas the incident light used to excite SPPs on the interface between the metal and the dielectric can be described as coupling [2], the coupling being focused on here refers to the exchange of energy between the SPPs and the SPO molecular excitons in the adjacent dielectric layer. Indeed, the interaction of the two can be modeled as two coupled oscillators, as discussed in the Theory section.

Such coupling leads to hybrid modes [11] which differ from the natural frequency of the individual, uncoupled oscillators. Initially, the SPO is primarily in the unswitched conformation. With irradiation of UV light of 365 nm, the portion of SPO in the MC conformation increases, and these molecules have an additional absorption near 600 nm, well within range to allow spectral overlap with the SPPs of the metal, as will be discussed shortly. With SPO molecules in the MC form, SPP-exciton coupling occurs and creates hybrid modes that separate from each other. The degree of splitting of the hybrid modes is dependent on the concentration of SPO and the fraction that is switched to the MC form in the dielectric layer.

For coupling to occur, two conditions must be met [11]: The two entities for coupling must have close proximity and their dispersion relations must overlap. The first condition of proximity is given by the setup of the dielectric layer with SPO being adjacent to the metal layer. For the second condition, the overlap between the dispersion relation of the SPPs of the metal sample and the energy of exciton is fulfilled in the following way. The exciton energy of the MC form of SPO is equivalent to an incident light wavelength of just less than 600 nm regardless of the AOI of the incident light. This

is in agreement with the absorption-related κ values of the index of refraction of the PS-SPO shown in Figure 4.6 d. If the SPP of either the Ag (Figure 4.7 bottom) or the Au (Figure 4.9 bottom) Kretschmann sample is compared with the exciton energy-equivalent wavelength on the vertical axis of just less than 600 nm, overlap is obviously possible. The result is an avoided crossing, also known as an anticrossing, easily visible at values of the AOI from about 55° to about 75° in the Ag sample (Figure 4.8 bottom) and about 65° to 75° in the Au sample (Figure 4.10 bottom).

The presence of an avoided crossing is a telltale sign of coupling between two entities, as discussed in the Theory section. Obviously, coupling exists here between the MC excitonic state and the SPPs induced by incident light. The coupling can be switched from off to on by changing the conformation of the SPO molecules with UV light. All optical control of coupling has been demonstrated with the samples.

The linewidths of the dispersion relations shown are indications of the amount of damping present in a system's metal layer [11]. It is worth noting that the linewidth of the Ag sample in Figures 4.7 and 4.8 is narrower than the linewidth of Au in Figures 4.9 and 4.10. This is to be expected considering that Ag has a lower damping rate than Au, as is well known.

In the Au sample, a broader linewidth is apparent in the SPP dispersion relation of the unswitched system (Figure 4.9 bottom) in accord with the greater damping to be expected from Au. With such damping, the measured polariton branches in the switched system (Figure 4.10 bottom) also reflect the character of the dashed parts of the black lines of nearly horizontal modes from theory in Figure 2.9, which signify modes that are not well defined. Figures 4.9 bottom and 4.10 bottom also show gold's characteristic general absorption (indeed, the source of the golden color) at wavelengths below about 500 nm. In the switched system in Figure 4.10 bottom, the avoided crossing is visible, but somewhat masked by the metal's general absorption profile.

Since the samples were first exposed to UV light to switch the SPO and then the dispersion relation was measured in < 10 min while the UV light was off, the potential for backswitching of SPO (the reversion of molecules from MC to leuco form) existed.

The extent of backswitching could influence the degree of peak splitting and must be ascertained.

4.4.3 Extent of backswitching

The amount of backswitching [81] taking place during the measurement of the full dispersion relation was quantified by a quick measurement immediately after the full angle sweep. The dispersion relation from the Ag sample from Figure 4.7 was measured again from 45° to 85° after freshly switching it. Then the sample was immediately re-exposed to UV light and only the angles from 55° to 65° were measured in about 90 seconds, thus effectively minimizing the time available for backswitching. This partial measurement could be compared to the full sweep of all angles measured minutes before to determine the extent of backswitching taking place during the measurement of the full dispersion relation.

The measurements were taken with the sample from Figure 4.7 (48 nm layer of Ag covered with 36 nm layer of PS-SPO (60 wt% SPO)), the results of which were superimposed to show the extent of backswitching taking place during the full measurement. The 10° remeasurement superimposed on the full dispersion relation taken about 2 minutes before can be seen in Figure 4.11. A small amount of backswitching can be seen to have taken place during the measurement time of the entire dispersion relation, which lasted < 10 min. However, the extent of backswitching of SPO is relatively small compared to the overall degree of splitting taking place between the upper and lower polaritonic branches, the extent of which will be discussed next.

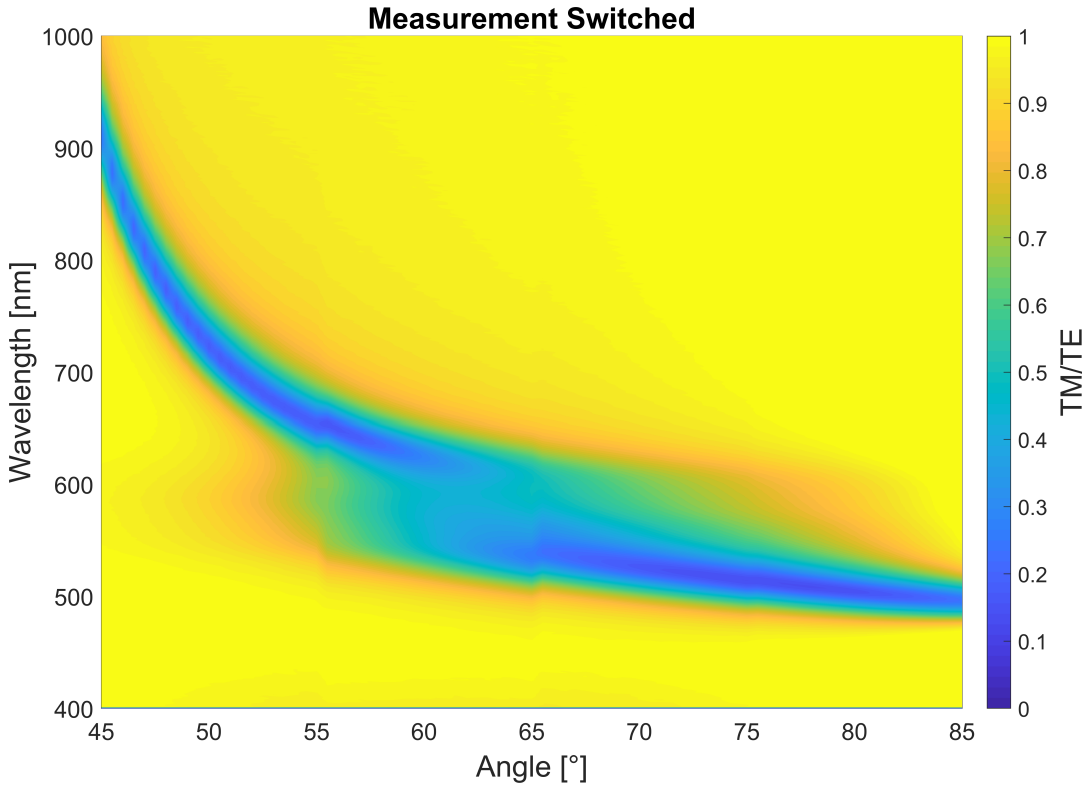

Figure 4.11: Re-using the sample from Figure 4.7 (48 nm layer of Ag covered with 36 nm layer of PS-SPO (60 wt% SPO)), immediate measurements were made from 55-65° (duration: < 100 s) after freshly switching with UV light, the results of which were superimposed on a just-remeasured full dispersion relation to show the extent of backswitching taking place during the 45-85° measurements. A small amount of backswitching can be seen to have taken place during the 45-85° measurement time, which lasted < 10 min.

4.4.4 Degree of Rabi splitting: ultrastrong regime

In addition to the linewidths of the polaritonic branches in the dispersion relations, the extent of Rabi splitting is important. The amount of splitting between the hybrid peaks at one AOI, or similarly said the degree of splitting between the upper and lower polaritonic branches, can be measured and categorizes the splitting into one strength regime of many regimes commonly denoted in the literature. The following is a discussion that analyzes the hybrid peak splitting present in the samples shown above.

As shown by Ruden and Reinecke [82] and by Reithmaier [83], mode splitting is dependent on the square root of the concentration of emitters in the system, which has its

origin in the coupling of the SPP mode to the N-count emitters (to be discussed further in upcoming section on current literature review). Modeled as interacting harmonic oscillators of the emitters and the SPPs, the solutions to the characteristic polynomial include two non-degenerate eigenstates whose frequency difference at resonance results in the splitting of the hybrid modes. The splitting increases with the square root of the N emitters. Here, the SPO concentration in the PS layer adjacent to the Ag thin film decisively determines the degree of splitting found in the hybrid modes. As can be seen in Figure 4.12, the concentration of the SPO in the PS was varied from 0 to 60 wt%. On exposure to UV light of 365 nm, in situ measurements at 57° AOI (not shown) were used to monitor the splitting until equilibrium was reached (< 30 s), whereafter the UV is turned off and the entire dispersion relation was measured from 45° to 85° at 0.5° steps with a sweep time of < 10 min. The UV light was not kept on during the angle sweep to prevent some peak reduction that had previously been observed, the origin of which is possibly degradation of the sample from the proximity and intensity of the UV LED.

As can be seen in Figure 4.12 a, the greater the SPO concentration, the greater the resultant splitting on UV exposure, in line with another study [33]. The peak positions (actually, dip positions) were determined for the 0, 30 and 60 wt% SPO samples, and the corresponding peak energy splitting calculated. Figure 4.12 b shows the calculated peak splitting in meV versus the square root of the same SPO concentration (a concentration percent axis is also shown for clarity).

First, in operando Rabi splitting of ~600 meV for the 60 wt% SPO sample in Figure 4.12 b is about 29% of the molecular transition energy of 2.1 eV (or ~14.5% when g/ω is compared, as often done in the literature, and is the ratio of the coupling strength to the resonance frequency; more later), results that put the system in the regime of ultrastrong coupling. As previously described, the ultrastrong coupling regime is defined historically [59] as the Rabi splitting being greater than 20% of the transition energy [60]. Second, a linear relationship between the splitting and square root of SPO concentration is manifest.

The 10 wt% SPO sample displays one peak around 2.025 eV, whereas the other peak

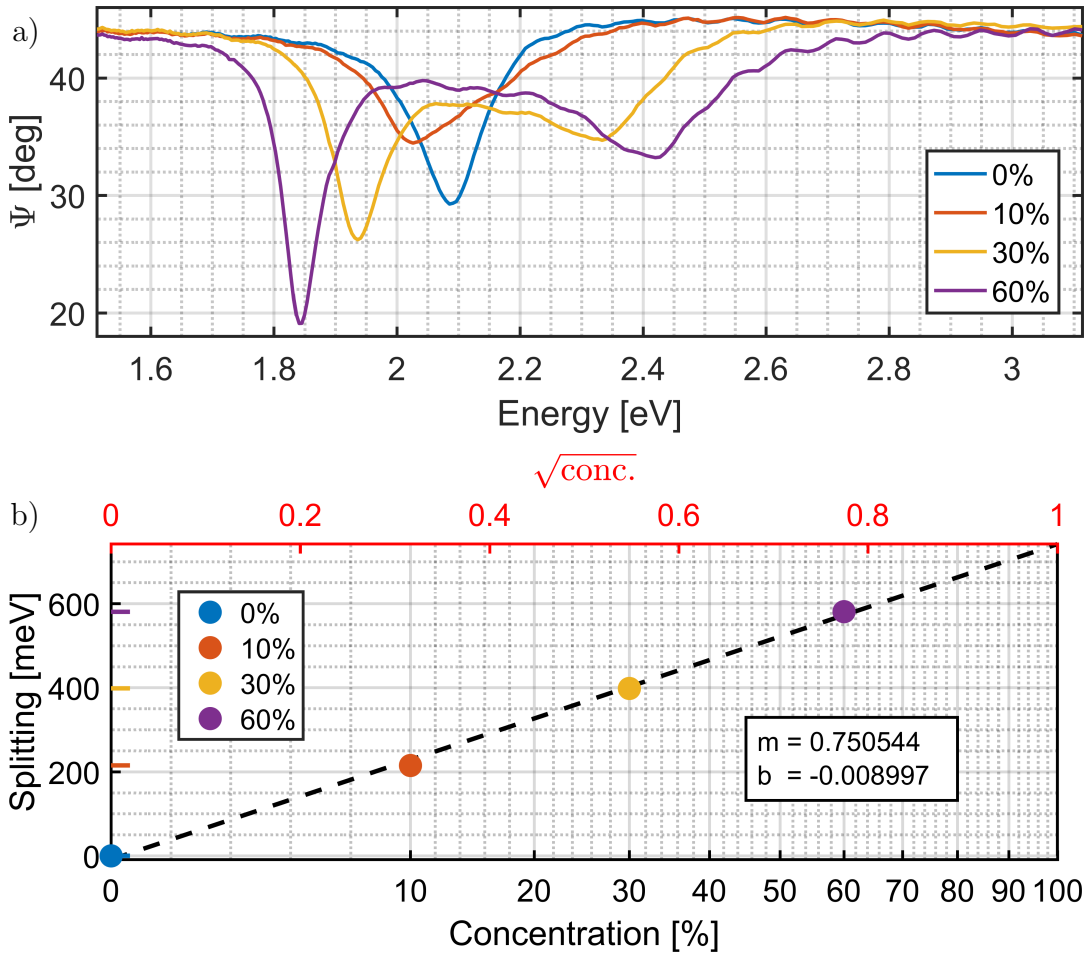

Figure 4.12: a) Spectroscopic ellipsometry measurements of Ψ (where $\tan(\Psi)$ is the magnitude of the ratio of amplitude reflection coefficients of the polarizations p and s, r_p/r_s; see Equation 2.12) versus incident light energy, corresponding to a vertical slice through Figure 4.8 at 57° AOI for the 60 wt% SPO sample. Incident light wavelengths in nm converted to energy in eV ($E = hc/\lambda \approx 1240/\lambda$). Shown are four concentrations of SPO by wt% in PS matrix (all within thickness 36 nm ± 1.5 nm) with similar Ag thickness (all within 50 nm ± 2 nm). b) From the energy difference between peaks in the top graph, the Rabi splitting in meV is shown as a function of the SPO wt% concentration and additionally as a function of the square root of the concentration, exhibiting a linear relationship with slope m and y-intercept b. See text for further discussion of 10 wt% SPO data point.

is difficult to determine. Based on the known concentration of 10 wt% SPO, the splitting was estimated from the linear relationship of the other samples and the peak estimated to be at 2.25 eV. The difficulty of accurately capturing both peaks of the 10 wt% SPO sample relate to the backswitching of the MC form of SPO. Whereas backswitching plays a negligible role in the higher SPO concentrations, in the lower 10 wt% SPO concentration the backswitching and resultant peak movement play a proportionately larger role in the overall peak splitting, as evidenced when viewing in person the sample switch back over time during in situ measurements at 57° AOI (not shown). After the UV light is turned off, the smaller peak at higher energy melds rapidly back into the single peak similar to that found in the 0 wt% SPO, rendering peak identification difficult. Faster measurement at the correct AOI instead of angle sweeping after switching could help to rectify the difficulty in future studies.

In addition to the SPO emitter molecule concentration, UV light intensity offers an additional degree of freedom for controlling the degree of peak splitting over time, as long as system degradation under UV light plays little or no role. That however was not an option with the configuration studied here, as previously mentioned, due to the degradation of samples when exposed to UV light of great intensity for longer periods of time.

4.4.5 In situ Rabi splitting with video

In addition, an in situ switching video at 57° AOI for SPO 60 wt% was recorded. Active splitting of the hybrid modes with constant exposure of the sample to UV light is seen in the video of the sample PS-SPO (60 wt% SPO) on Ag in the Kretschmann setup. Splitting begins when the single peak begins to divide and corresponds to the UV light (365 nm) being turned on. After being exposed for 16 seconds, the splitting of the peaks stabilizes as equilibrium between unswitched and switched SPO is reached. The video is sped up to make viewing more convenient. Figure 4.13 shows excerpted images from the video superimposed on each other with the appropriate timestamps mentioned in

the caption.

As can be seen in the video, the splitting can be turned on by UV light exposure. Under carefully controlled conditions of UV illumination intensity and duration, the degree of splitting will be controllable. Further investigations with suitable light sources could delve more deeply into this interesting aspect of controlling Rabi splitting dynamically. Any UV degradation of the organics involved could be tackled by consulting the multitude of photochromic molecules [84] already known to chemists.

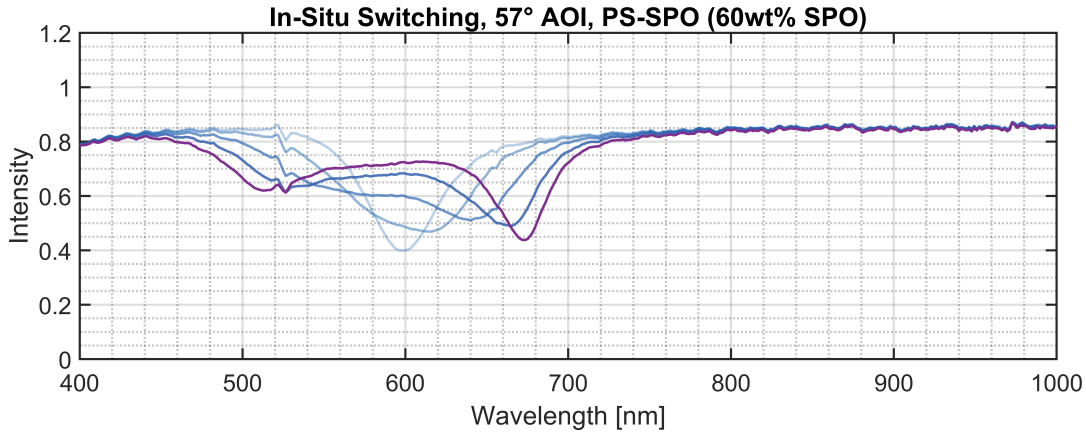

Figure 4.13: Summary image of five consecutive images from in situ video. The sample investigated was Ag/PS-SPO (40-60 wt%) in the Kretschmann configuration. The single peak splits into two hybrid peaks during exposure to UV LED light of 365 nm for a total of 16 s. The timestamps for the 5 curves are: 0 s (lightest blue, single peak), 1.10 s (next lightest), 2.21 s, 4.96 s, 16.0 s (purple curve, two hybrid peaks).

4.4.6 Time dependence of peak splitting

The following data was gleaned from the in situ video of dynamic Rabi splitting in the Kretschmann setup and shows the time-dependent nature of SPO's conformational change and resultant ultrastrong coupling. Exponential behavior was to be expected when the system is exposed to UV light and the SPO switched, and is presented here only in the interest of completeness.

In Figure 4.14, the time dependence is shown of the switched SPO concentration

and the associated degree of splitting of the hybrid modes for the results in Figure 4.8 bottom. By determining the peak positions of the hybrid modes from the video represented in Figure 4.13, the splitting strength due to coupling is shown (in red) to switch in time upon exposure to UV light (UV on at time 0). Using Figure 4.12 bottom, the percent concentration of switched SPO molecules coupled (and therefore the unswitched percentage, as plotted) can be determined and is shown (in blue). Sample was same 60 wt% SPO used in Figures 4.7 bottom and 4.8 bottom.

Given a specific SPO concentration and UV intensity, the strength of peak splitting might be chosen by a carefully controlled use of the irradiation time, a degree of freedom to be investigated in possible future studies.

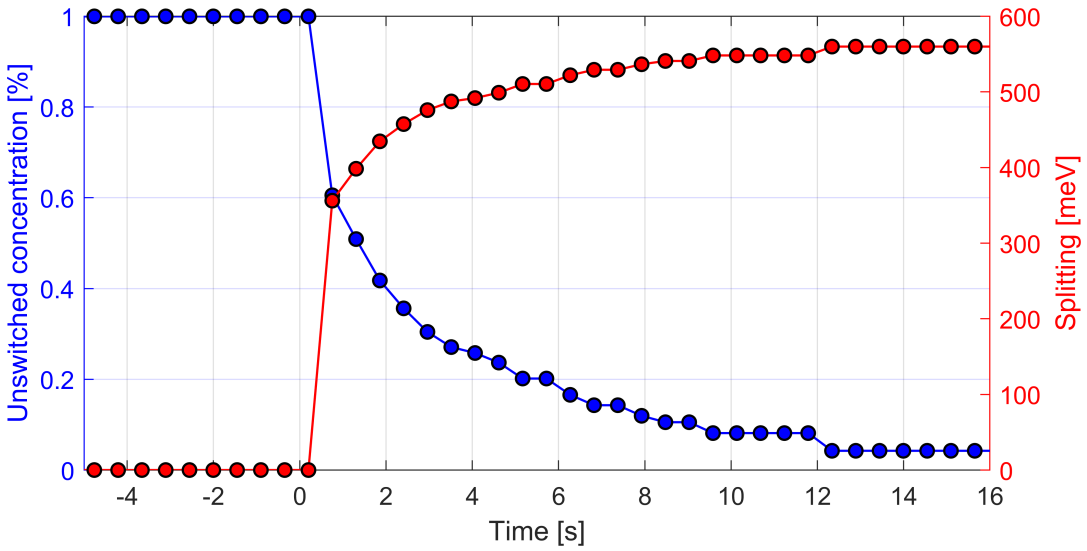

Figure 4.14: From in situ video, Rabi splitting in meV (red) and unswitched SPO percent concentration (blue) are shown to develop exponentially from time 0, when the UV light is switched on.

4.5 Investigation of Tamm Plasmon & SPO Coupling in Tamm Setup

The Kretschmann setup [2], [31] makes possible the observation of plasmon-exciton coupling [11] and the formation of an avoided crossing, as shown above. However, the disadvantage of the setup cannot be denied: the prism is bulky and fragile; the index matching gel is sticky and messy to remove; measurement is tricky and requires experience. With the introduction of a different setup to create surface waves called Tamm plasmons, the investigation of plasmon-exciton coupling and its attendant avoided crossing becomes simplified enough to consider making potential routine investigations and testing both feasible and affordable.

4.5.1 Simulations of sample series 3: DBR + PS-SPO + Ag

Simulations of a DBR (Figure 3.5) composed of TiO_2 (3 layers, each 50 nm) and SiO_2 (2 layers, each 120 nm) predict that the stack produces a reflectance of nearly 90% across the wavelengths of interest, namely around 600 nm. The great difference in published indices of refraction between thin films of TiO_2 ($n \approx 2.41$ [75]) and SiO_2 ($n \approx 1.47$ [74]) determines the width of the stopband; here, from about 450 nm to 700 nm. Although the number of bilayers determines the amount of reflectance, the difference in indices of refraction also plays a role in the reflectance. This DBR would have the advantage of very few layers to deposit and yet have a wide enough stopband and reflectance around 600 nm to make observation of possible coupling with a Tamm plasmon possible.

Figure 4.15 a shows the simulation results for the proposed DBR + PS-SPO. The AOI for incoming light is set to 55° from the surface normal, an angle acceptable for the spectroscopic ellipsometer with measurements possible between 45° and 90°.

Figure 4.15 b shows that same solid black curve for the reflectance of the DBR + PS-SPO but additionally shows a dashed black line for the reflectance of the stack once SPO is switched by exposure to UV light. Reflected light from the stack shows absorption

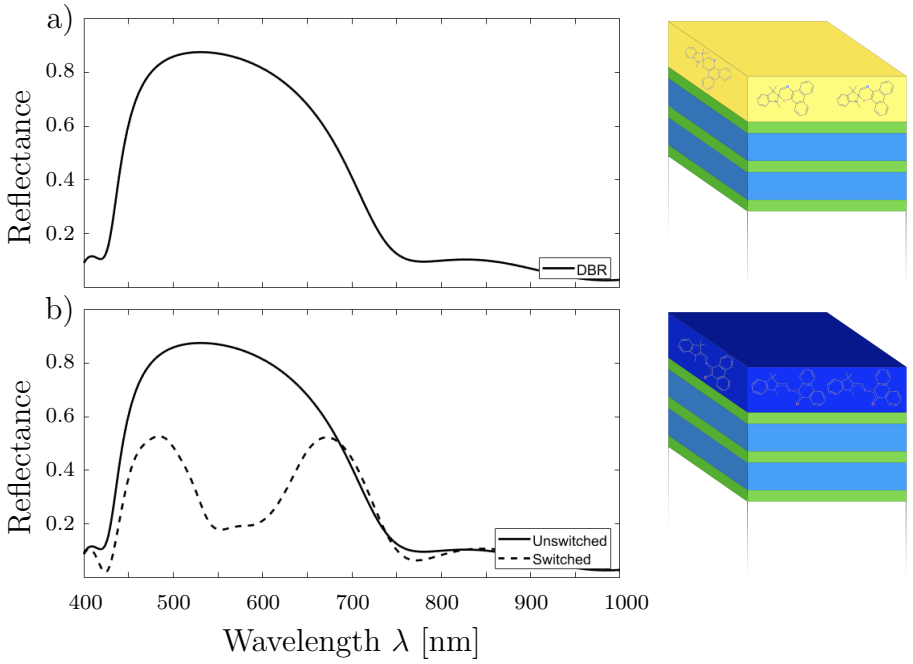

Figure 4.15: Simulation results for reflectance of incident light at AOI of 55° for DBR consisting of five layers of TiO_2 (50 nm, green) and SiO_2 (120 nm, blue) together with a PS-SPO layer. **Top**) unswitched (yellow), and **bottom**) switched (dark blue).

due to switched SPO just around 600 nm. It is interesting to note that an asymmetry of the dip is seen, just as in the κ values of the PS-SPO sample presented earlier in this chapter (Figure 4.6), and could possibly be due to exciton coupling as theorized before.

The DBR + PS-SPO stack is simulated next (Figure 4.16 a) with a top layer of a thin film of Ag (31 nm). The layer is not thick enough to be bulk and opaque, yet thin enough to reflect much of the incident light, as seen by the now higher reflectance above 700 nm. Most prominent in the graph is the blue curve with a narrow deep dip just below 600 nm: a Tamm plasmon mode. Wavelengths of light in this region match the periodicity of the PS-SPO spacer layer to form a standing wave in that layer. The envelope of the standing wave will peak and then decay in the DBR (see Figure 2.6). As a standing wave, the amplitude of these wavelengths of light experience constructive interference upon exposure to incident light. As discussed in the the Theory section, the loss channels for the Tamm plasmon mode are radiative modes at the bottom of

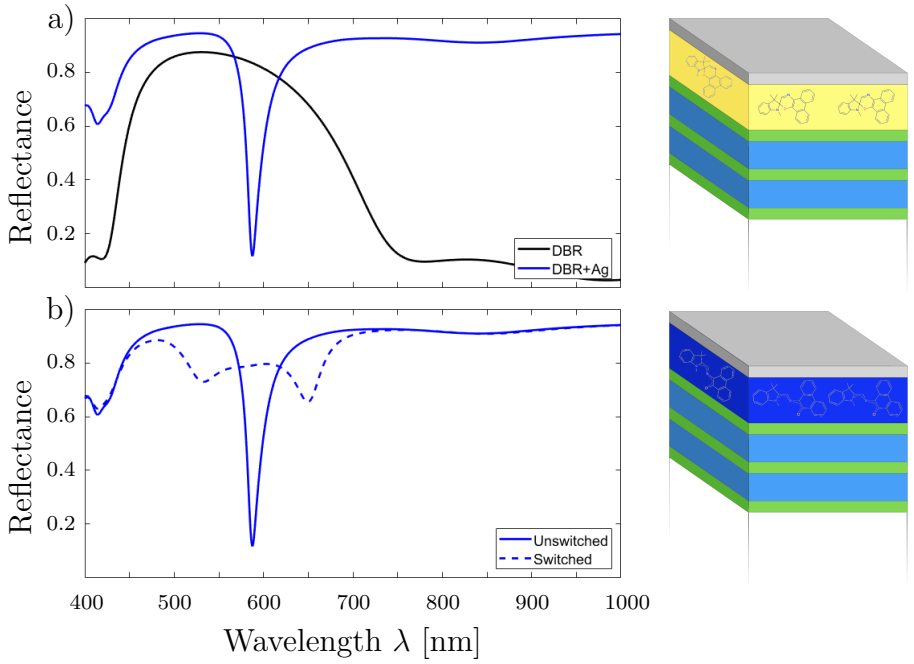

Figure 4.16: **Top**) At the AOI of 55°, the simulation reflectance of the stopband of the DBR + PS-SPO spacer layer of the sample is the solid black curve. With the addition of the Ag layer of thickness 31 nm, the reflection of the stack changes to the solid blue curve. The deep and narrow dip just below 600 nm signals a Tamm plasmon. **Bottom**) The simulated Tamm plasmon dip just below 600 nm is from the stack with unswitched SPO with AOI at 55°. Once the SPO is switched with UV light (365 nm), the dashed blue line results. Notice dips at ~530 nm and ~650 nm.

the stack, i.e., light transmits through the stack, and some losses due to the Ag layer and its imaginary part of the index of refraction. In effect, the light wavelengths of the Tamm plasmon form a resonant, standing wave in the stack and radiate out through the bottom.

In Figure 4.16 b, the simulation predicts the effect of switching the SPO to the MC form by exposing the stack to UV light of 365 nm. To be clear, one would expect absorption of the standing waves of light in the stack just below 600 nm (the Tamm plasmon explained above) to be absorbed by the now existent MC molecules (see Figure 4.6). Indeed, the dip depth is reduced, which indicates that less light is able to couple to radiative modes out the bottom of the stack and it either couples to radiative modes out

the top of the stack, i.e., gets reflected, or it is absorbed by the switched SPO. However, the appearance of dips at ~530 nm and ~650 nm are not explained by simple absorption of the Tamm plasmon modes of light.

Here, the dips are theorized to be due to coupling between the Tamm plasmon mode and MC excitons forming hybrid modes with the hallmarks of Rabi splitting and an avoided crossing in the dispersion relation.

To experimentally investigate the appearance of possible hybrid modes in the simulations, stacks of DBR + PS-SPO + Ag were produced and analyzed on the spectroscopic ellipsometer.

4.5.2 Results of sample series 3: DBR + PS-SPO + Ag

The DBR here was created in a magnetron sputtering chamber from TiO_2 and SiO_2 targets, with layers deposited to form a stopband that spanned the absorption wavelength region of switched SPO (~600 nm). Afterwards, the deposition of a PS-SPO spacer layer was done via spin coating, subsequently to be topped off by a thin film of sputtered Ag. All layer thicknesses were predefined by the simulations, and all attempts were made to build the Tamm stack to those specifications so as to achieve the goal of investigating coupling between Tamm plasmons and switchable SPO theorized from those simulations.

After the deposition of each layer, the samples were taken to the spectroscopic ellipsometer for thickness determination of the layer just completed. Each sample was measured in reflection mode on the ellipsometer and an updated model was used to determine the thickness and optical constants (complex index of refraction, $\tilde{n}$) for the just-deposited layer. Table 4.3 shows the results of the thickness and $\tilde{n}$ (real n and imaginary κ, values standardly reported at 589.3 nm, the mid-value of the sodium D line doublet), as well as the resulting MSE of the final model fit.

Once the fabrication of the samples was finished, they were measured on the spectroscopic ellipsometer from 45° to 85° at 0.5° steps (5 s measurement at each angle) without

Table 4.3: Sample series 3 results of stack layer materials, thicknesses, and associated n and κ values and mean squared error values from ellipsometer results.

Sample	Layer	Material	Thickness [nm]	n	κ	MSE
9 o'clock	7	Ag	36	0.12	3.57	17.864
9 o'clock	6	PS-SPO (50-50 wt%)	215	1.56	0	15.765
9 o'clock	5	TiO_2	56	2.09	0	29.021
9 o'clock	4	SiO_2	134	1.48	0	16.780
9 o'clock	3	TiO_2	47	2.23	0	9.985
9 o'clock	2	SiO_2	125	1.39	0	10.335
9 o'clock	1	TiO_2	55	2.18	0	1.830
3 o'clock	7	Ag	35	0.12	3.57	21.761
3 o'clock	6	PS-SPO (50-50 wt%)	212	1.54	0	18.761
3 o'clock	5	TiO_2	57	2.08	0	25.281
3 o'clock	4	SiO_2	133	1.44	0	15.941
3 o'clock	3	TiO_2	47	2.25	0	11.817
3 o'clock	2	SiO_2	125	1.40	0	10.184
3 o'clock	1	TiO_2	54	2.18	0	1.861

exposure to UV light, i.e., unswitched SPO. The total measurement time was less than 7 min. Subsequently, the sample was exposed to UV light from the LED wand above the sample and the entire dispersion relation again measured from 45° to 85°.

To give an idea of the appearance of such a sample, the images presented in Figure 4.17 top row show the DBR + PS-SPO layer in three stages: before switching, during UV exposure, and after switching with a UV wand. The attempt was made to view the sample from an AOI of 55°. In the images and in person, very little if any difference is visible to the naked eye due to switching. Additionally, the appearance of a DBR + PS-SPO + Ag is shown in Figure 4.17 bottom row before, during and after switching with a UV wand. In photos and in person, a definite difference due to UV exposure can be seen in the center of the sample, the only area of interest because the ellipsometer light only probes the sample at the center with an approximately 2 mm diameter beam and does not probe the sample near the edges where edge effects from spin coating occur.

In Figure 4.18 left, the simulation of the ideal Tamm setup aimed for here is repeated

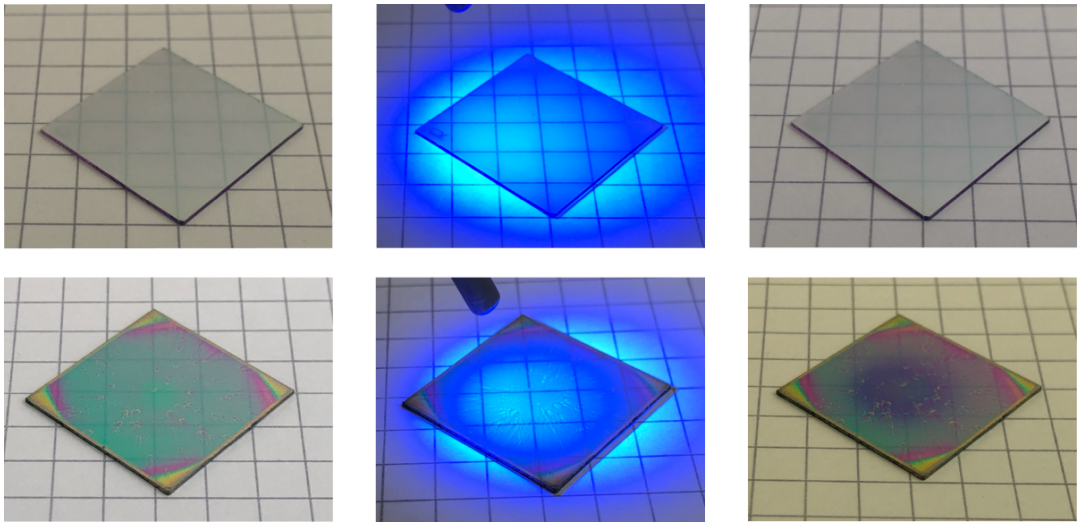

Figure 4.17: **Top row**, left to right: DBR + PS-SPO sample before switching, during UV exposure, and after switching. **Bottom row**, left to right: DBR + PS-SPO + Ag sample before switching, during UV exposure, and after switching.

(see Table 3.1 for values). To the right, the actual layer values of the Tamm setup produced in the laboratory was graphed to see how well the simulation and experimental data would concur.

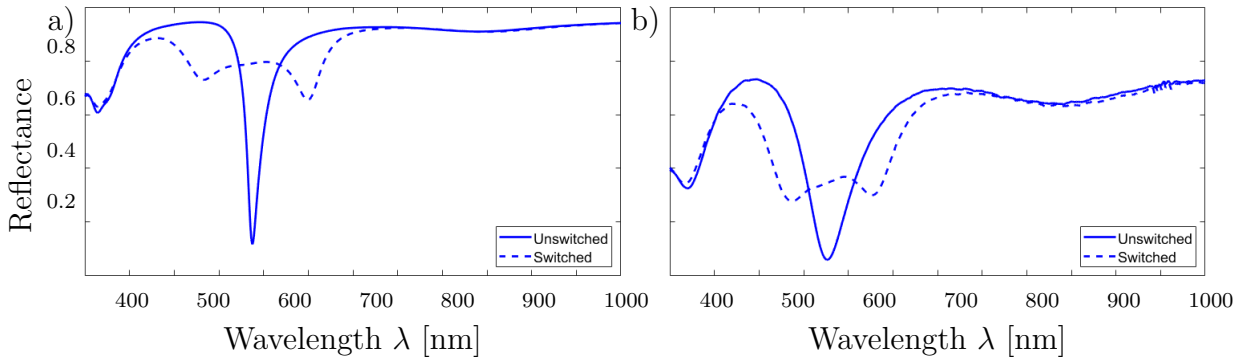

Figure 4.18: **Left**) repeat depiction of Tamm setup that was aimed for from simulation. **Right**) graph of spectrum determined from actual measured layer values of Tamm setup produced in the laboratory – to be compared respectively to Figure 4.19 (unswitched) and Figure 4.20 (switched) at 55° AOI.

4.5.3 Discussion of sample series 3: DBR + PS-SPO + Ag

Figure 4.19 shows the results of the unswitched SPO ellipsometer measurements. The scale of the graph is the intensity of the reflectance of light from the sample stack, with greatest reflectance now in dark blue. Yellow indicates the lack of reflectance, so the light couples into the stack to form a standing wave at those wavelengths. This is the Tamm plasmon mode.

Figure 4.20 shows the same sample after having been exposed to UV light of 365 nm for 40 s. The most prominent features of the graph are the appearance of two dips (bright yellow bands) at approximately 530 nm and 650 nm, along with a strip of greater reflectance between them [85]. Since the equivalent energy of the exciton is just below 600 nm, the Tamm plasmon mode before switching the SPO is split into two peaks after switching, as predicted by the simulation done at 55°. The appearance of an avoided crossing is the telltale sign of plasmon-exciton coupling [11], as seen previously in the Kretschmann configuration results. The parabolic nature of the dispersion curve seen in the Kretschmann setup is at first glance absent in the Tamm plasmon-exciton coupling seen here. However, the parabolic curve is indicated at the very lowest angles of 45° to 50°. Comparison to the early, important papers on Tamm plasmons by Sasin, et al. [67] and Symonds, et al. [86] shows that the parabolic nature of the Tamm plasmon-exciton dispersion curve is often seen at angles of incidence much less than 45°. The angles less than 45° cannot be measured on the spectroscopic ellipsometer used in these studies.

The calculated Rabi splitting at AOI 55° from peaks at ~530 nm and ~640 nm is ~400 meV.

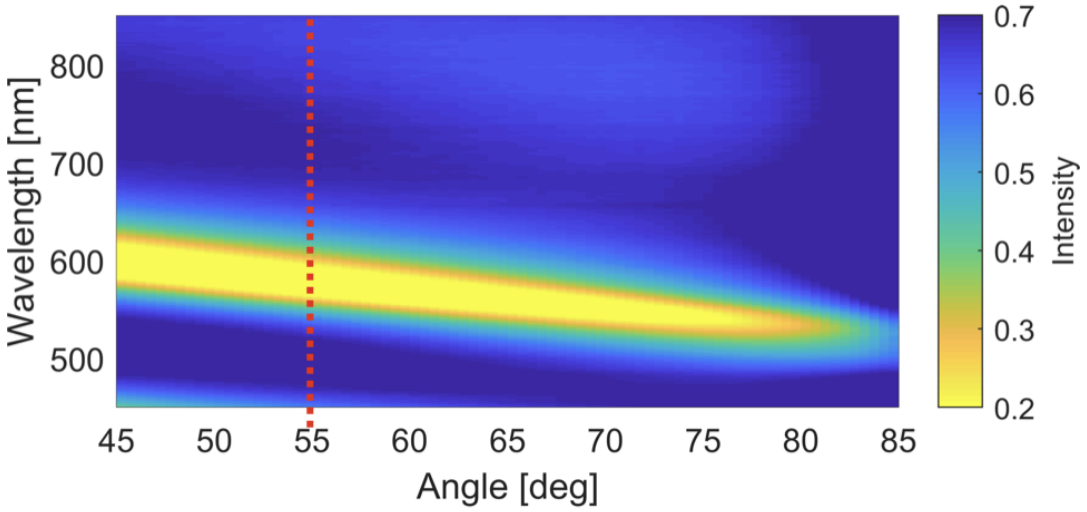

Figure 4.19: Sample of Tamm setup composed of DBR + PS-SPO + Ag measurements on spectroscopic ellipsometer with AOI from 45° to 85° with 0.5° steps (5 s measurement time per angle) prior to switching. Scale is intensity of reflectance, with yellow indicating light coupling into stack and not being reflected, i.e., Tamm plasmons. Red dashed line shows 55° AOI for comparison to spectra predicted with simulations.

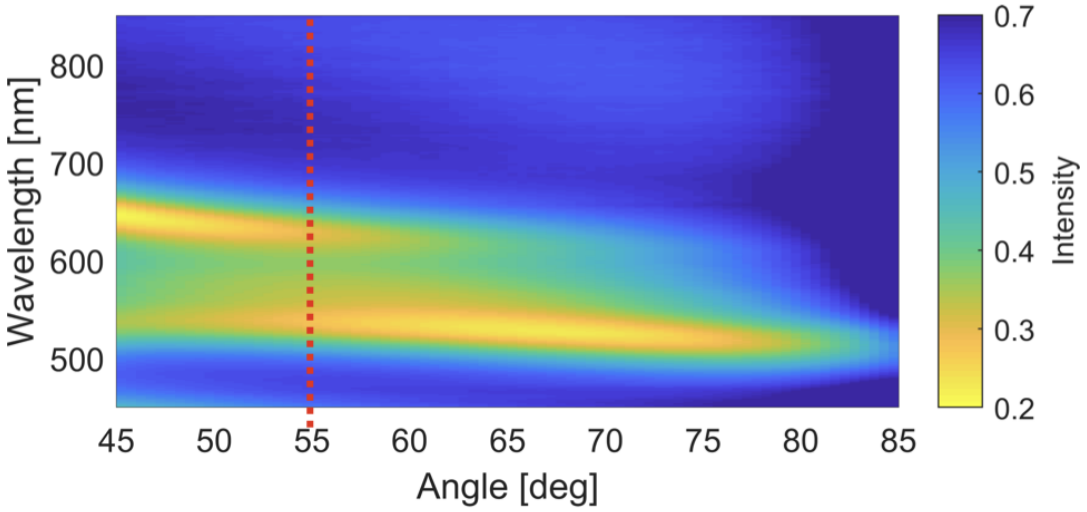

Figure 4.20: Sample of Tamm setup composed of DBR + PS-SPO + Ag measurements on spectroscopic ellipsometer with AOI from 45° to 85° with 0.5° steps (5 s measurement time per angle) after being switched with UV light (365 nm for 40 s). Same scale as in Figure 4.19 above. Red dashed line shows 55° AOI for comparison to spectra predicted with simulations. Splitting of dispersion relation into two hybrid peaks with avoided crossing at ~600 nm, the location of switched SPO exciton energy.

4.6 Relation of Findings to Literature

The experiments and results presented here belong to the spate of literature to appear in recent decades showing possible strong coupling in a myriad of experimental setups in the field of (nano-)photonics. Many of the published findings regarding strong coupling between light and matter are, of course, experimental in nature. Nonetheless, as discussed in the Theory section, theoretical underpinnings to strong coupling experimental results do exist and range from the renowned Jaynes-Cummings model (interaction of a single two-level atom with a quantized mode of an optical cavity) of cQED to the Tavis-Cummings model (extended model that includes N two-level atoms with the cavity quantized photonic mode), amongst other models. The quantum optical theoretical models and their resultant equations are often used in reports of experimental results to couch the findings in terms of established theories in the field.

Concepts from the theoretical background that are applicable to these studies include the description of the relationship between the coupling strength g and the concentration N/V of emitters in the photon-exciton coupled system. One such relationship often employed in the literature [16], [87], [88] is

$$g = \frac{1}{\hbar}\sqrt{N}\boldsymbol{\mu}\cdot\boldsymbol{E} = \mu\sqrt{\frac{\omega N}{2\hbar\epsilon\epsilon_0 V}} \tag{4.1}$$

also sometimes given as [17], [89], [90]

$$\hbar\Omega_{\mathrm{R}} = 2\hbar g = 2d\sqrt{N}\sqrt{\frac{\hbar\omega}{2\epsilon_0 V}} \tag{4.2}$$

where $\boldsymbol{\mu}$ is the dipole moment of N identical emitters, $\boldsymbol{E}$ is the cavity electric field experienced *uniformly* by the emitters, ω is the angular frequency of the light mode in the cavity, V is the mode volume for the cavity, and ϵ_0 is the vacuum permittivity; d is the transition dipole moment of the molecules and $\hbar$ is the reduced Planck constant. In Equation 4.1, the cavity material permittivity ϵ is included, whereas it is simply assumed to be unity in Equation 4.2, i.e., a vacuum cavity. Notice the relationship

$\Omega_R = 2g$ between the Rabi splitting Ω_R and the coupling constant g, meaning that the splitting between the upper and lower polariton branches at the resonance frequency is twice the value of the coupling constant.

Briefly, the equations above are derived [11], [17] by starting with the Jaynes-Cummings Hamiltonian describing a coupled system of a quantum two-level emitter, a single mode of the cavity quantized electromagnetic field, and the interaction of the two. The model is extended to N molecules to derive the Tavis-Cummings Hamiltonian (also known as the Dicke Hamiltonian), where the full analytical solution can be used, but often a limiting case is taken. In the limit of a large number of N emitters but a low number of photons to excite the emitters (i.e., low light intensities that remain within the linear regime), a transformation that maps the spin-system of the two-level emitters to bosonic systems is used, which results in a new Hamiltonian that is the quantum equivalent of the two classical coupled Harmonic oscillators described in the Theory section. However, in this quantum equivalent description, the N two-level emitters behave as a single large quantum oscillator. The hybrid eigenmode solutions of this new Hamiltonian result in the coupling factor shown in Equation 4.1 and the Rabi splitting in Equation 4.2.

As can be seen in the two equations above, the coupling strength g and the Rabi splitting Ω_R are proportional to the square root of the number of quantum emitters N per volume of the photonic mode V. These relationships and similar ones involving N/V are often quoted in the literature for strong coupling [17], [88]. Many efforts in research have been made to increase the Rabi splitting through increasing the number of emitters N or decreasing the mode volume V in various experimental setups. Plasmonics offers just such a reduction in the mode volume V due to the confinement and enhancement of the field in plasmonic structures.

In Equation 4.1, the first equality holds [17], [88] for those interactions between light and matter where the dipole approximation applies, i.e., the wavelength of the electromagnetic field is much greater than the size of the emitters, an approximation that applies to the experiments presented in this thesis. The second equality in Equation 4.1 only holds when all N emitters are aligned in the uniform electric field, a situation

not given in the Kretschmann setup outlined in this thesis where the evanescence of the electromagnetic field assures a non-uniform electric field and the emitters are not expected to be well-aligned but instead randomly oriented in the dielectric matrix. In addition, the choice for the mode volume V becomes unclear in the open cavity of a Kretschmann configuration, where one "mirror" of the metal layer and the evanescence of the SPP-generated field form the "cavity." What should be chosen as the volume for the mode? And does the Ohmic loss in the metal layer render the model unusable?

4.6.1 Questions raised in the nanophotonics community

Indeed, the question has arisen of late in the literature [88] as to what extent theoretical models based on a two-level system or a collection of two-level systems in a non-radiative cavity with low losses and only one mode can apply to real systems where a radiative cavity may have higher losses and more than one mode. Indeed, Tserkezis et al. [88] question the tendency of nanophotonics researchers who are perhaps "driven by the need to shed light on experimental findings [88]" to apply equations, including those above, in their analyses, which leads to situations where "concepts from other fields have been straightforwardly adapted and applied outside their proper context [88]." In fact, Tserkezis et al. include themselves in that pool of researchers whose papers may include such possible misapplications. They write that the impetus to address the topic of applicability of quantum concepts in strong coupling nanophotonics is "borne out of genuine concern for the credibility and esteem of our community, in an attempt to stop the spreading of misconceptions at an early stage," [88] going so far as to compare what they call a "necessary and open invitation to a fruitful discussion" to a similar debate from which "cQED already benefitted" decades ago [88]. Their attempt, and mine, is not to "discredit or undervalue" [88] any researchers, but instead strive to clarify the way forward for the field and place the research interpretations on more sound, theoretical scientific footing.

Tserkezis et al. [88] make several arguments to support their claim of questioning the application of quantum theory to many real-world experiments with different contexts. In general, definitions of the mode volume V and the number of emitters N become difficult depending on the experimental setup. Applying their general logic to the Kretschmann setup described here, the emitters in the dielectric layer are exposed to the evanescent field, albeit to different directions and magnitudes of the field with its exponential decay dependent on the distance from the metal. How should the volume mode V be defined? A simple geometric volume is a good start, but does not reflect the evanescence of the field. In addition, once the SPO is switched to the MC form, the effective index of refraction of the layer changes, effectively changing the extent of the evanescent field's reach into the dielectric layer depending on the wavelength (see Figure 4.6 b); above about 575 nm, the refractive index increases, which should decrease the extent of the evanescent field in the layer, thereby exposing fewer emitters to the field. From about 575 nm down to about 450 nm, the refractive index decreases, which should increase the extent of the evanescent field and expose more emitters in the dielectric layer to the field. With all this, how can the mode volume V be defined, and on top of that, how many emitters are being exposed, i.e., what is N?

Many theories as espoused by the Jaynes-Cummings model or the Tavis-Cummings model are certainly sound and good, as evidenced alone by their longevity in the scientific literature and usefulness in describing many different quantum systems. Nonetheless, applying these theoretical descriptions to an ever growing number of experimental setups that push the boundaries of the field of nanophotonics is also being called into question [88].

Although answering such questions is beyond the scope of the analysis here, it can be said that questions still linger in the community whether and to what extent equations developed for describing quantum two-level systems can be applied to systems with excitons acting collectively when interacting with the cavity mode(s) of hard-to-define mode volumes. With the publication of these open questions, nanophotonics researchers have the opportunity to engage in a discussion and debate that will hopefully bring

advancement to this field of scientific inquiry and description.

But not all hope is lost in the quest for support through theory. The Kretschmann setup experimental findings presented here can yet be placed on sound theoretical foundations. A completely quantum description of photon-emitter coupling between emitters and propagating surface plasmons on two-dimensional metal surfaces has been published. With this, the findings still reflect the square root N/V proportionality relationship for the Rabi splitting, albeit without the difficulties of defining N and V, as Tserkezis et al. [88] pointed out.

4.6.2 An ab initio theoretical foundation for the Kretschmann experiments

Even with the cloud of aforementioned concerns about the proper application of theory to experiment, there is still a silver lining to be found. As far as the coupling of surface plasmon polaritons to emitters is concerned, we need not rely only on the Equations 4.1 and 4.2 and their attendant questions of applicability. An ab initio quantum formalism has been derived [91], [92] for just such an experiment as presented here in the prism-involved coupling of SPPs on Ag to SPO excitons in an adjacent dielectric layer. The first-principles derivation presented by the authors places the phenomenon of strong coupling between SPPs and quantum emitters on a sound theoretical foundation, thus eliminating the above-mentioned concerns. In the end, the theory presented by the authors maintains the conclusion that the coupling strength is proportional to square root N/V; thus, the switchable SPP-exciton coupling data and interpretation reported here remain supported by theory, albeit on more solid theoretical grounds.

In brief, the theoretical sample mimics the samples depicted in Figure 3.3, with a dielectric layer doped with N quantum emitters on top of a metallic thin film. Each of the quantum emitters, assumed to have discrete electronic levels with a large separation between them and only one possible transition at the frequency of excitation, are represented by a quantum two-level system. Placed near a metal thin film, the quantum

emitters have three decay channels: SPP excitation considered the coherent channel, and far-field radiation of photons and losses to Joule heating in the metal as dissipation mechanisms. The ensemble of quantum emitters is distributed homogeneously in the dielectric layer.

A general Hamiltonian for coherent interaction between quantum emitters and two dimensional SPPs on a Ag layer is first written and then simplified with the assumptions of the low excitation regime (i.e., no non-linear effects from intense fields), homogeneous and disordered arrangements of quantum emitters in the layer (i.e., no preferred molecule orientation), and a collective mode of the N quantum emitters (i.e., collective excitation in terms of bosonic operators instead of quantum emitter raising and lowering operators) where each excitation is weighted by the strength of its coupling to the SPPs depending on the distance of the quantum emitters relative to the plane of the metal thin film. With the simplified Hamiltonian, the coherent coupling between N emitters (now treated as an ensemble) and the SPPs is treated in an ab initio quantum manner. From this derivation, the coupling constant g is able to be determined without fitting parameters and solely from first principles.

The coupling constant g includes the dipolar interaction of a given quantum emitter and the quantized SPP field. In addition, g takes into account the decay length of SPP evanescent field in the dielectric layer with increasing distance from the metal thin film. The coupling strength g does not take into account propagation losses of the SPPs, but instead includes the effective length of the SPP modes. Because the magnitude of g depends on the orientation of the quantum emitters with respect to the metal plane, an isotropic average of two limiting cases (parallel and perpendicular orientations) is taken.

In the end, g depends not only on the thickness of the dielectric layer but also on the decay of the evanescent field with distance measured normal to the metal layer (therefore, also dependent on the local dielectric environment). The two dependencies lead to a maximum value of g at a distance from the metal surface of a few hundred nanometers, beyond which the evanescent field is negligible and any emitters present would experience no coupling.

The authors [91], [92] also investigate the losses associated with the quantum emitter ensemble and the SPP mode by considering the decay lifetimes of the SPP mode and the quantum emitters, even incorporating vibrorotational degrees of freedom of quantum emitter molecules. Whereby the details of the derivation are beyond the scope of the current discussion, it need be said that for the SPP in-plane momentum that matches that of the quantum emitter excitation (the crossing point referred to in Figure 2.9) where maximum coupling will occur gives a general solution for the Rabi splitting Ω_{R} as

$$\Omega_R \propto \sqrt{g^2 - (\gamma_D + \gamma_\Phi - \gamma_a)^2} \tag{4.3}$$

where g is the coupling constant, γ_D is the decay rate of the collective ensemble of N quantum emitters, γ_Φ is the dephasing rate of the organic molecules' vibrorotational states (temperature dependent), and γ_a is the decay rate of the SPP mode. As long as the exchange rate of energy between the SPPs and the emitter ensemble is greater than the dissipation in the loss channels described by the decay rates, the value of the Rabi splitting is real-valued and defined by the authors to be in the strong coupling regime. Imaginary values of Ω_{R} would be interpreted as belonging to the weak coupling regime.

For an idea of the orders of magnitude of the decay rates, the authors [91], [92] note that whereas $\gamma_\Phi \approx 40$ meV for room temperature organic molecules used in many strong coupling experiments and $\gamma_\Phi \gg \gamma_D$, γ_a is true for the decay rates they used, it is the molecular vibrorotatory degrees of freedom and their associated dephasing that acts as the strongest loss mechanism for coherent coupling between SPPs and quantum emitters.

As in the case of all three descriptions of the coupling constant from classical, semi-classical and quantum descriptions of SPP strong coupling, the coupling constant is found to be

$$g \propto \sqrt{\frac{N}{V}} \tag{4.4}$$

with N/V the number of emitters in the dielectric layer per geometric volume of the layer.

It must be noted that the general relationship between coupling strength and emitter concentration is maintained in this final result even with the added complexity of the theoretical model and its inclusion of the exponential decay of the SPPs evanescent field in the dielectric, the emitters acting collectively, and the vibrorotational states of organic molecules. As the coupling constant scales with the square root of the emitter concentration, so does the Rabi splitting Ω_{R}.

With this ab initio derivation of the coupling constant, the experimental results of the Kretschmann setup presented in this thesis stand on solid theoretical footing.

A discussion of literature results on strong coupling in switchable plasmon-exciton systems was presented in Section 2.9, making possible a comparison with results of Rabi splitting achieved here. Schwartz et al. [52] reported Rabi splitting in a traditional two-mirror cavity with a PMMA sandwiched layer doped with photochromic spiropyran molecules to be 713 meV, which is about **32%** of the transition energy of the molecular resonance of 2.2 eV —clearly a case of ultrastrong coupling [59], [60]. Schwartz et al. briefly report in the same paper [52] that coupling between surface plasmons in a hole array in a 200 nm thick Ag layer covered with the same PMMA-spiropyran dielectric layer as in the traditional cavity achieved a value of 650 meV, which equates to about **30%** of the transition energy of the same molecular resonance as above. Baudrion et al. [53] reported Rabi splitting of 294 meV between plasmon resonance modes of an array of Ag nanoparticles covered with a layer of PMMA doped with a spiropyran with a transition energy equivalent to 2.18 eV. The Rabi splitting to transition energy ratio is about **13%**, much lower than Schwartz et al. and theorized to be due to the lower quality factor of the dipolar resonances. Lin et al. [54] reported 572 meV Rabi splitting in a coupled system of hybrid plasmon-waveguide modes from Al nanodisk arrays embedded in a PMMA layer doped with spiropyran photochromic molecules with a molecular transition energy of 2.18 eV, which results in a ratio of about **26%** —in the ultrastrong coupling regime [59], [60]. The Rabi splitting reported in this thesis of ~600 meV for the 60 wt% SPO sample

in Figure 4.12 b is about **29%** of the molecular transition energy of 2.1 eV, well into the regime of ultrastrong coupling. Although the specific photochromic molecule used for the excitonic coupling partner differs in these studies and certainly the nature of the photonic coupling partner varies (e.g., cavity mode; localized surface plasmon modes of metallic nanoparticle arrays; surface plasmon polaritons excited in a Kretschmann configuration in this thesis), the Rabi splitting-transition energy ratio achieved in this thesis of **29%** in the Kretschmann setup can compare well with the best values reported in the literature for switchable plasmon-exciton coupling.

If one compares the Rabi splitting achieved in the Tamm setup of this thesis, a ratio of ~400 meV to the transition energy of 2.1 eV is **19%**, just shy of the definition of the onset of the ultrastrong coupling regime [59], [60].

4.6.3 An ab initio theoretical foundation for the Tamm setup experiments

The experimental findings of the Tamm plasmon-exciton coupling are, as yet, not described by a consolidated theory, aside from predictions made by Morozov et al. [13]. As sometimes happens, the bounds of experimental research regarding the strong coupling regime of light-matter interactions surpasses the current reach of complete theoretical descriptions. Whereas the aspects of quantum emitters, DBRs, and Tamm plasmons themselves are described in the literature, a comprehensive theoretical description of such Tamm plasmon-exciton strong coupling has yet to be published. In the spirit of the topic of strong coupling, the author of this dissertation would like to take this opportunity to emit a call out to theoreticians in the field to fill this literature cavity with a supporting theory mode of their own.

CHAPTER 5

Summary

Interaction between light and matter can be fascinating and colorful, like rainbows in the sky, reflections from sunlight striking thin oil slicks on the surface of water, or the striking iridescence of some butterfly wings [1]. But in general, light-matter interactions are complex to explain. The present work focuses on the interaction of surface plasmons (collective excitations of the electron system) in metals and excitons (coupled electron-hole pairs) in switchable molecules.

Thin film samples were prepared with standard techniques such as magnetron sputtering and spin coating. All samples were computer simulated via the transfer matrix method [19]–[22] before production in order to determine what setups and layer thicknesses and materials would lead to interactions between plasmons and excitons.

The excitons in the optical systems used here came from the merocyanine conformation of a spirooxazine (SPO), a photochromic molecule [3]–[5], [44] whose use was inspired by involvement in the Collaborative Research Center 677 "Function by Switching." The molecules are reversibly photoswitchable chromophores that are more polarizable in the merocyanine conformation. UV light determines the fraction of switched photochromic molecules: the more molecules in the switched conformation, the greater the degree of energy splitting between hybrid modes (so-called Rabi splitting) when coupled to the SPPs.

By using such excitons and two different types of surface waves — surface plasmon polaritons [2] and the somewhat recently investigated Tamm plasmons [12], [13], [40] — the coupling was switched and observed in two ways: a Kretschmann configuration and a Tamm plasmon setup.

Measurements were done using spectroscopic ellipsometry [18], [26], which not only

permits rapid measurement of the dispersion relation with an avoided crossing of the resultant non-radiative modes when switched, but also in situ observation of Rabi splitting during UV exposure; a video of such splitting, represented here with a summary image with five curves at different points in time with their respective timestamps, was presented and shows the newly observed molecular conformation-induced photoswitchable splitting.

In the first approach, surface waves of surface plasmon polaritons excited at a metal-polystyrene interface on a prism in a Kretschmann configuration [2], [31] couple to excitons of the merocyanine conformation of spirooxazine dye dispersed in the polystyrene matrix, resulting in the formation of hybrid modes [11] and their attendant Rabi splitting. The degree of splitting depends on the concentration of switched dye molecules, in turn controllable by the degree of UV exposure. By employing spectroscopic ellipsometry and a Kretschmann configuration, it was shown that strong coupling, sizeable shifts in frequency response in comparison to the magnitude of the eigenmodes themselves, is possible between SPPs at a precious metal-dielectric interface and molecular excitons in the selfsame dielectric layer. The optical response and the strong transition dipole of the switched chromophore lead to such strong splitting in the coupled system.

Besides the molecule concentration and the UV light intensity, the duration of UV exposure could thus in the future be used as a degree of freedom in controlling the extent of coupling in plasmonic systems.

It is the incorporation of photoswitchable chromophores in a coupled system that makes a high contrast Rabi switch possible. Splitting of the resultant hybrid modes in the Kretschmann configuration was shown to be nearly 600 meV for a 60 wt% SPO in polystyrene thin film sample and attests to the ultrastrong coupling regime described in the literature [59], [60]. For the surface waves, surface plasmon polaritons on both Ag and Au films were used, with Ag showing the best splitting results due to its relatively low damping and concomitant narrow linewidths.

In the second approach, surface waves in the form of Tamm plasmons [12], [13], [40] were excited in a prism-less and compact system composed of a spacer layer with SPO

molecules sandwiched between two types of mirrors: a thin film of Ag and a distributed Bragg reflector. With exposure to incident white light, the standing waves of Tamm plasmons in the optical system were shown to couple with SPO in the switched form by clear evidence of an avoided crossing after switching the photochromic molecules with UV light. Rabi splitting of about 400 meV is reported and is nearly in the ultrastrong coupling regime [59], [60]. Again, the coupling was shown to be switchable.

It could be shown that the coupling between surface waves and molecular excitons can be controlled like a switch, off and on. The coupling is switchable by changing with UV exposure the concentration of molecular chromophores in a more highly polarizable conformation. The off/on switching of the coupling between surface waves and molecular excitons presented here offers the ability to change a physical property of an optical system remotely and on demand. Optically turning Rabi splitting on or off leads to high contrast changes in reflection and absorption at certain wavelengths in the dispersion relation of the optical system as a whole.

In conclusion, by using a sophisticated experimental and sample setup, the light-matter interaction phenomenon of strong coupling was made switchable by making the excitonic mode available through the conformational change of a photochromic molecule for the first time in a prism-mediated Kretschmann setup for surface plasmon polaritons, and then in a first-ever coupling of Tamm plasmon polaritons and molecular excitons in a setup that was also made switchable. Understanding and controlling light-matter interactions have taken a small step forward.

CHAPTER 6

Outlook

In the present thesis, strong surface plasmon polariton coupling with excitons of switched photochromic molecules has been observed for the first time in a Kretschmann setup and in a Tamm plasmon setup. Based on accumulated experience, the following experimental improvement, a look into details and extensions to other materials are suggested here.

For experimental improvement, it can be seen in Figure 4.12 that for low SPO concentrations, splitting identification is difficult as the smaller peak at higher energy melds rapidly back into the single peak, rendering peak identification difficult. Faster measurements at the correct angle of incidence instead of angle sweeping after switching could help to rectify this difficulty.

Generally, the Tamm plasmon-emitter coupling setup used in this thesis offers the possibility of a straightforward tool that can be used to investigate light-matter coupling, switchable or not. Further and systematic studies using the Tamm setup are warranted.

Investigations with suitable light sources for molecule switching could delve more deeply into the interesting aspect of controlling Rabi splitting dynamically by varying the switching light in intensity, duration, or even through the use of light pulsing. Although many molecules would eventually degrade upon extended UV exposure, alternative molecules in combination with the light experiments suggested above could prove fruitful. Looking for other photochromic molecules could also be relevant with respect to reduced switching times.

With this thesis, the prospects of manipulating plasmon-exciton coupling at the molecular level has the added ability to transition coupling off and on. Promising research and even applications in areas such as optical amplification and chemical reaction manipulation [16] have a new method of control: a switch. In those circumstances where

switching speed is not of supreme importance but instead must simply be available, the work shown here offers potential applicability. If chemical species generation can be manipulated one way with a switch off and another way with a switch on, one system offers two potential outcomes for applications.

As discussed, questions have been raised in the nanophotonics community whether and to what extent equations developed for describing quantum two-level systems can be applied to systems with excitons acting collectively when interacting with the cavity mode(s) of a hard-to-define mode volume and number of emitters. As the experimental research forges ahead with developing new and interesting combinations of light-matter coupling, answering such theoretical questions is sure to be an active area full of opportunity for further research.

As a final suggestion initiated by a review [93], the systematic investigation of polaritons in van der Waals materials is suggested. Aside from the collective oscillations of electrons in metals that give rise to surface plasmon polaritons presented in this thesis, the authors write that van der Waals materials give rise to many different types of polaritonic modes "with the highest degree of confinement among all known materials." Examples of such materials include graphene (plasmon polaritons), topological insulators (phonon polaritons), FeSe- and Cu-based superconductors (Cooper-pair polaritons), and magnetic resonances (magnon polaritons). The promise of a great degree of confinement together with the authors' affirmation that such systems are electrically tunable offers the clever researcher additional tools to explore strong coupling between light and matter. Although much research has certainly been conducted in this area to date, the opportunities afforded by the many van der Waals materials available could hold undiscovered and rich areas of research into light-matter coupling.

Abbreviations

Abbreviation	Definition
AOI	angle of incidence
cQED	cavity quantum electrodynamics
MC	merocyanine, an SPO conformational form
MSE	mean squared error
PMMA	poly(methyl methacrylate)
PS	polystyrene
PS-SPO	polystyrene plus admixture of SPO
SPO	chromophore involved in study*
SPP	surface plasmon polariton

* 1,3-Dihydro-1,3,3-trimethylspiro [2H-indole-2,3 -[3H]phenanthr[9,10-b](1,4)oxazine]

,

Appendix

Example calculation for preparation of PS-SPO solution for dielectric layers.

solution NAME:	**Jesse2**	
desired wt% SPO in the PS-SPO	50	wt%
wt% PS in the PS-SPO	50	wt%
Weight of PS pellets		
measured mass of PS in pellet form	0.2692	g
calculated mass of SPO to weigh out	0.2692	g
Weight of SPO		
measured mass of SPO weighed out	0.2688	g
total mass of PS-SPO	0.5380	g
calculated % of PS	50.04	wt%
calculated % of SPO	49.96	wt%
determine mass of toluene to add to PS-SPO mixture		
desired weight percent PS-SPO in toluene	5	wt%
resultant desired mass fraction of PS-SPO in toluene	0.05	
calculated mass of toluene needed	10.222	g
given density of toluene	0.867	g/mL
volume of toluene to add to PS-SPO mixture		
calculated toluene to add volumetrically	11.79	mL
afterwards, weigh amount of toluene actually added		
measured mass of toluene added	10.2192	g
actual fraction of PS-SPO in toluene	0.050013015	
Final weight percent PS-SPO in toluene	**5.00**	**wt%**

References

[1] K. Nassau, *The Physics and Chemistry of Color: The Fifteen Causes of Color*, series Wiley Series in Pure and Applied Optics. John Wiley and Sons, Inc., 1983, ISBN: 0-471-86776-4 (cited on pages 1, 2, 115).

[2] S. Maier, *Plasmonics: Fundamentals and Applications*. Springer, 2007, ISBN: 9780387331508. DOI: 10.1007/0-387-37825-1 (cited on pages 2, 3, 5, 9, 13–15, 42, 47, 49, 82, 89, 98, 115, 116).

[3] V. A. Lokshin, A. Samat, and A. V. Metelitsa, "Spirooxazines: Synthesis, structure, spectral and photochromic properties," *Russ. Chem. Rev.*, volume 071, pages 893–916, 011 November 2002, ISSN: 0036-021X. DOI: 10.1070/RC2002v071n11ABEH000763 (cited on pages 2, 5, 24, 43, 79, 115).

[4] G. Favaro, F. Masetti, U. Mazzucato, G. Ottavi, P. Allegrini, and V. Malatesta, "Photochromism, thermochromism and solvatochromism of some spiro[indolinoxazine]-photomerocyanine systems: Effects of structure and solvent," *J. Chem. Soc., Faraday Trans.*, volume 90, pages 333–338, 2 1994. DOI: 10.1039/FT9949000333 (cited on pages 2, 5, 24, 43, 77, 79, 115).

[5] J. C. Crano and R. J. Guglielmetti, "Organic photochromic and thermochromic compounds," *Eds JC Crano, RJ Guglielmetti, New York: Kluwer …*, volume 1, page 495, 1999, ISSN: 0-306-45882-9. DOI: 10.1007/b115590 (cited on pages 2, 5, 24, 43, 79, 115).

[6] M. K. Hedayati, M. Javaheri, A. U. Zillohu, H. J. El-Khozondar, M. S. Bawa'aneh, A. Lavrinenko, F. Faupel, and M. Elbahri, "Photo-driven super absorber as an active metamaterial with a tunable molecular-plasmonic coupling," *Advanced Op-*

tical Materials, volume 2, pages 705–710, 8 August 2014, ISSN: 21951071. DOI: 10.1002/adom.201400105 (cited on pages 2, 3, 43, 77).

[7] M. Jamali, M. K. Hedayati, B. Mozooni, M. Javaherirahim, R. Abdelaziz, A. U. Zillohu, and M. Elbahri, "Photoresponsive transparent conductive metal with a photobleaching nose," *Advanced Materials*, volume 23, pages 4243–4247, 37 2011, ISSN: 09359648. DOI: 10.1002/adma.201102353 (cited on pages 3, 43).

[8] M. Elbahri, A. U. Zillohu, B. Gothe, M. K. Hedayati, R. Abdelaziz, H. J. El-Khozondar, M. Bawa'aneh, M. Abdelaziz, A. Lavrinenko, S. Zhukovsky, and S. Homaeigohar, "Photoswitchable molecular dipole antennas with tailored coherent coupling in glassy composite," *Light: Science and Applications*, volume 4, e316, 7 2015, ISSN: 2047-7538. DOI: 10.1038/lsa.2015.89 (cited on pages 3, 43).

[9] M. K. Hedayati, A. U. Zillohu, T. Strunskus, F. Faupel, and M. Elbahri, "Plasmonic tunable metamaterial absorber as ultraviolet protection film," *Applied Physics Letters*, volume 104, number 4, pages 11–16, 2014, ISSN: 00036951. DOI: 10.1063/1.4863202 (cited on page 3).

[10] M. K. Hedayati, S. Fahr, C. Etrich, F. Faupel, C. Rockstuhl, and M. Elbahri, "The hybrid concept for realization of an ultra-thin plasmonic metamaterial antireflection coating and plasmonic rainbow," *Nanoscale*, volume 6, number 11, pages 6037–6045, 2014, ISSN: 20403372. DOI: 10.1039/c4nr00087k (cited on page 3).

[11] P. Törmä and W. L. Barnes, "Strong coupling between surface plasmon polaritons and emitters: A review," *Reports on Progress in Physics*, volume 78, 1 May 2015, ISSN: 00344885. DOI: 10.1088/0034-4885/78/1/013901 (cited on pages 3–5, 22–24, 28–31, 82, 89, 90, 98, 104, 107, 116).

[12] J. A. Gaspar-Armenta and F. Villa, "Photonic surface-wave excitation: Photonic crystal–metal interface," *Journal of the Optical Society of America B*, volume 20, pages 2349–2354, 11 2003, ISSN: 0740-3224. DOI: 10.1364/josab.20.002349 (cited on pages 3, 5, 13, 20, 35, 54, 115, 116).

[13] K. M. Morozov, A. V. Belonovskii, K. A. Ivanov, E. I. Girshova, and M. A. Kaliteevski, "Interaction of a tamm plasmon and exciton in an organic material in the strong coupling mode," *Semiconductors*, volume 53, pages 1314–1317, 10 October 2019, ISSN: 10906479. DOI: 10.1134/S1063782619100142 (cited on pages 3, 5, 13, 37, 114–116).

[14] D. L. Smith, *Thin-film deposition : principles and practice*, International ed. New York : McGraw-Hill, 1995, ISBN: 978-0-07-113913-7 (cited on pages 3, 4, 26, 55).

[15] K. Norrman, A. Ghanbari-Siahkali, and N. B. Larsen, "6 studies of spin-coated polymer films," *Annual Reports Section "C" (Physical Chemistry)*, volume 101, pages 174–201, October 2005 2005, ISSN: 0260-1826. DOI: 10.1039/b408857n (cited on pages 3, 27).

[16] E. Cao, W. Lin, M. Sun, W. Liang, and Y. Song, "Exciton-plasmon coupling interactions: From principle to applications," *Nanophotonics*, volume 7, pages 145–167, 1 2018, ISSN: 21928614. DOI: 10.1515/nanoph-2017-0059 (cited on pages 4, 106, 119).

[17] M. Hertzog, M. Wang, J. Mony, and K. Börjesson, "Strong light-matter interactions: A new direction within chemistry," *Chemical Society Reviews*, volume 48, pages 937–961, 3 2019, ISSN: 14604744. DOI: 10.1039/c8cs00193f (cited on pages 4, 23, 28, 106, 107).

[18] H. Fujiwara, *Spectroscopic Ellipsometry Principles and Applications*. John Wiley and Sons, Ltd, 2007, ISBN: 9780470016084. DOI: 10.1002/9780470060193 (cited on pages 5–7, 9–11, 69, 115).

[19] E. Hecht and A. Zając, *Optics*, 3rd, series Addison-Wesley world student series. Addison-Wesley, 1998, ISBN: 0201838877 (cited on pages 5, 8, 115).

[20] M. Born, E. Wolf, A. B. Bhatia, P. C. Clemmow, D. Gabor, A. R. Stokes, A. M. Taylor, P. A. Wayman, and W. L. Wilcock, *Principles of Optics: Electromagnetic Theory of Propagation, Interference and Diffraction of Light*, 7th edition. Cam-

bridge University Press, 1999. DOI: 10.1017/CBO9781139644181 (cited on pages 5, 8, 11, 46, 115).

[21] H. Macleod, *Thin-Film Optical Filters*, series Series in Optics and Optoelectronics. CRC Press, 2017, ISBN: 9781351982245 (cited on pages 5, 8, 115).

[22] K. J. Pascoe, "Reflectivity and transmissivity through layered, lossy media: A user-friendly approach," 2001. [Online]. Available: https://apps.dtic.mil/sti/citations/ADA389099 (cited on pages 5, 8, 39, 115).

[23] G. D. Scholes and G. Rumbles, "Excitons in nanoscale systems," *Nature Materials*, volume 5, number 9, pages 683–696, 2006, ISSN: 14764660. DOI: 10.1038/nmat1710 (cited on pages 5, 13).

[24] J. D. Joannopoulos, S. G. Johnson, J. N. Winn, and R. D. Meade, *Photonic Crystals: Molding the Flow of Light (Second Edition)*. Princeton University Press, 2011, ISBN: 9781400828241 (cited on pages 5, 13, 16, 18).

[25] M. Fox, *Optical Properties of Solids*, series Oxford Master Series in Physics. OUP Oxford, 2010, ISBN: 9780199573363 (cited on pages 7, 11, 12, 22, 46, 79).

[26] J. A. W. C. Inc, "Completeease™ data analysis manual," pages 1–207, 2011 (cited on pages 10–12, 45, 49, 69, 115).

[27] O. Stenzel, *The Physics of Thin Film Optical Spectra: An Introduction*, series Springer Series in Surface Sciences. Springer International Publishing, 2015, ISBN: 9783319216027 (cited on pages 11, 46).

[28] C. J. Bardeen, "The structure and dynamics of molecular excitons," *Annual Review of Physical Chemistry*, volume 65, number 1, pages 127–148, 2014. DOI: 10.1146/annurev-physchem-040513-103654 (cited on page 13).

[29] W. L. Barnes, "Surface plasmon-polariton length scales: A route to sub-wavelength optics," *Journal of Optics A: Pure and Applied Optics*, volume 8, 4 2006, ISSN: 14644258. DOI: 10.1088/1464-4258/8/4/S06 (cited on page 14).

[30] M. Großmann, A. Klick, C. Lemke, J. Falke, M. Black, J. Fiutowski, A. J. Goszczak, E. Sobolewska, A. U. Zillohu, M. K. Hedayati, H. G. Rubahn, F. Faupel, M. Elbahri, and M. Bauer, "Light-triggered control of plasmonic refraction and group delay by photochromic molecular switches," *ACS Photonics*, volume 2, pages 1327–1332, 9 2015, ISSN: 23304022. DOI: 10.1021/acsphotonics.5b00315 (cited on page 14).

[31] E. Kretschmann and H. Raether, "Radiative decay of nonradiative plasmons excited by light," *Z. Naturforsch. A*, volume 23, pages 2135–2136, November 1968, ISSN: 1094-4087. DOI: 10.1515/zna-1968-1247 (cited on pages 15, 42, 47, 49, 82, 98, 116).

[32] T. Maurer, P. M. Adam, and G. Lévêque, "Coupling between plasmonic films and nanostructures: From basics to applications," *Nanophotonics*, volume 4, pages 363–382, 3 2015, ISSN: 21928614. DOI: 10.1515/nanoph-2014-0015 (cited on pages 15, 44).

[33] S. Balci, C. Kocabas, S. Ates, E. Karademir, O. Salihoglu, and A. Aydinli, "Tuning surface plasmon-exciton coupling via thickness dependent plasmon damping," *Physical Review B - Condensed Matter and Materials Physics*, volume 86, page 235 402, 23 December 2012, ISSN: 10980121. DOI: 10.1103/PhysRevB.86.235402 (cited on pages 15, 93).

[34] M. Ives, T. M. Autry, S. T. Cundiff, and G. Nardin, "Direct imaging of surface plasmon polariton dispersion in gold and silver thin films," *Journal of the Optical Society of America B*, volume 33, pages C17–C21, 7 2016, ISSN: 0740-3224. DOI: 10.1364/JOSAB.33.000C17 (cited on pages 16, 88).

[35] G. von Freymann, V. Kitaev, B. V. Lotsch, and G. A. Ozin, "Bottom-up assembly of photonic crystals," *Chem. Soc. Rev.*, volume 42, pages 2528–2554, 2013, ISSN: 1460-4744. DOI: 10.1039/c2cs35309a (cited on pages 16, 55).

[36] H. Shen, Z. Wang, Y. Wu, and B. Yang, "One dimensional photonic crystals: Fabrication, responsiveness and emerging applications in 3d construction," *RSC Adv.*,

volume 6, pages 4505–4520, 2016, ISSN: 2046-2069. DOI: 10.1039/C5RA21373H (cited on pages 16, 55).

[37] R. Gross and A. Marx, *Festkoerperphysik*, series De Gruyter Studium. De Gruyter, 2018, ISBN: 9783110558227 (cited on pages 16, 18).

[38] C. Symonds, S. Azzini, G. Lheureux, A. Piednoir, J. M. Benoit, A. Lemaitre, P. Senellart, and J. Bellessa, "High quality factor confined tamm modes," *Scientific Reports*, volume 7, page 3859, 1 December 2017, ISSN: 2045-2322. DOI: 10.1038/s41598-017-04227-1 (cited on pages 20, 21, 36, 37, 54).

[39] A. V. Kavokin, I. A. Shelykh, and G. Malpuech, "Lossless interface modes at the boundary between two periodic dielectric structures," *Physical Review B - Condensed Matter and Materials Physics*, volume 72, page 233 102, 23 December 2005, ISSN: 10980121. DOI: 10.1103/PhysRevB.72.233102 (cited on page 20).

[40] M. Kaliteevski, I. Iorsh, S. Brand, R. A. Abram, J. M. Chamberlain, A. V. Kavokin, and I. A. Shelykh, "Tamm plasmon-polaritons: Possible electromagnetic states at the interface of a metal and a dielectric bragg mirror," *Physical Review B - Condensed Matter and Materials Physics*, volume 76, page 165 415, 16 October 2007, ISSN: 10980121. DOI: 10.1103/PhysRevB.76.165415 (cited on pages 20, 54, 115, 116).

[41] L. Novotny, "Strong coupling, energy splitting, and level crossings: A classical perspective," *American Journal of Physics*, volume 78, pages 1199–1202, 11 November 2010, ISSN: 0002-9505. DOI: 10.1119/1.3471177 (cited on page 22).

[42] Y. S. Joe, A. M. Satanin, and C. S. Kim, "Classical analogy of fano resonances," *Physica Scripta*, volume 74, page 259, 2 2006, ISSN: 1402-4896. DOI: 10.1088/0031-8949/74/2/020 (cited on page 22).

[43] G. Such, R. a. Evans, L. H. Yee, and T. P. Davis, "Factors influencing photochromism of spiro-compounds within polymeric matrices," *Journal of Macromolecular Science, Part C: Polymer Reviews*, volume 43, number 4, pages 547–579, 2003, ISSN: 1532-1797. DOI: 10.1081/MC-120025978 (cited on page 24).

[44] H. Dürr and H. Bouas-Laurent, *Photochromism: Molecules and Systems*. Elsevier Science, 2003, ISBN: 9780080538839 (cited on pages 24, 25, 43, 79, 115).

[45] H. Xia, K. Xie, and G. Zou, "Advances in spiropyrans/spirooxazines and applications based on fluorescence resonance energy transfer (fret) with fluorescent materials," *Molecules*, volume 22, 12 2017, ISSN: 14203049. DOI: 10.3390/molecules22122236 (cited on pages 24, 25).

[46] H. Tian and J. Zhang, *Photochromic Materials: Preparation, Properties and Applications*. Wiley, 2016, ISBN: 9783527683727 (cited on pages 24, 25).

[47] M. Ohring, *Materials Science of Thin Films*. Elsevier Science, 2002, ISBN: 9780125249751 (cited on pages 26, 27, 55).

[48] G. S. Agarwal, *Quantum Optics*. Cambridge University Press, 2012, ISBN: 9781139035170. DOI: 10.1017/CBO9781139035170 (cited on page 28).

[49] G. Grynberg, A. Aspect, C. Fabre, and C. Cohen-Tannoudji, *Introduction to Quantum Optics: From the Semi-classical Approach to Quantized Light*. Cambridge University Press, 2010. DOI: 10.1017/CBO9780511778261 (cited on page 28).

[50] J. R. Tischler, M. S. Bradley, Q. Zhang, T. Atay, A. Nurmikko, and V. Bulović, "Solid state cavity QED: Strong coupling in organic thin films," *Organic Electronics: physics, materials, applications*, volume 8, pages 94–113, 2-3 2007, ISSN: 15661199. DOI: 10.1016/j.orgel.2007.01.008 (cited on page 29).

[51] A. J. Moilanen, T. K. Hakala, and P. Törmä, "Active control of surface plasmon–emitter strong coupling," *ACS Photonics*, volume 5, number 1, pages 54–64, 2018, ISSN: 2330-4022. DOI: 10.1021/acsphotonics.7b00655 (cited on pages 30, 32–34).

[52] T. Schwartz, J. A. Hutchison, C. Genet, and T. W. Ebbesen, "Reversible switching of ultrastrong light-molecule coupling," *Physical Review Letters*, volume 106, page 196 405, 19 May 2011, ISSN: 0031-9007. DOI: 10.1103/PhysRevLett.106.196405 (cited on pages 32–34, 113).

[53] A. L. Baudrion, A. Perron, A. Veltri, A. Bouhelier, P. M. Adam, and R. Bachelot, "Reversible strong coupling in silver nanoparticle arrays using photochromic molecules," *Nano Letters*, volume 13, pages 282–286, 1 January 2013, ISSN: 15306984. DOI: 10.1021/nl3040948 (cited on pages 32, 33, 113).

[54] L. Lin, M. Wang, X. Wei, X. Peng, C. Xie, and Y. Zheng, "Photoswitchable Rabi splitting in hybrid plasmon–waveguide modes," *Nano Letters*, volume 16, pages 7655–7663, 12 December 2016, ISSN: 1530-6984. DOI: 10.1021/acs.nanolett.6b03702 (cited on pages 32, 34, 113).

[55] R. A. Pala, K. T. Shimizu, N. A. Melosh, and M. L. Brongersma, "A nonvolatile plasmonic switch employing photochromic molecules," *Nano Letters*, volume 8, number 5, pages 1506–1510, 2008. DOI: 10.1021/nl0808839 (cited on page 32).

[56] H. Nishi, T. Asahi, and S. Kobatake, "Light-controllable surface plasmon resonance absorption of gold nanoparticles covered with photochromic diarylethene polymers," *Journal of Physical Chemistry C*, volume 113, pages 17 359–17 366, 40 2009, ISSN: 19327447. DOI: 10.1021/jp906371k (cited on page 32).

[57] T. Ming, L. Zhao, M. Xiao, and J. Wang, "Resonance-coupling-based plasmonic switches," *Small*, volume 6, pages 2514–2519, 22 November 2010, ISSN: 16136810. DOI: 10.1002/smll.201000920 (cited on page 32).

[58] Y. B. Zheng, B. Kiraly, S. Cheunkar, T. J. Huang, and P. S. Weiss, "Incident-angle-modulated molecular plasmonic switches: A case of weak exciton-plasmon coupling," *Nano Letters*, volume 11, pages 2061–2065, 5 2011. DOI: 10.1021/nl200524b (cited on page 32).

[59] A. F. Kockum, A. Miranowicz, S. D. Liberato, S. Savasta, and F. Nori, "Ultrastrong coupling between light and matter," *Nature Reviews Physics*, volume 1, pages 19–40, January 2019, ISSN: 2522-5820. DOI: 10.1038/s42254-018-0006-2 (cited on pages 32, 93, 113, 114, 116, 117).

[60] P. A. Thomas, W. J. Tan, H. A. Fernandez, and W. L. Barnes, "A new signature for strong light-matter coupling using spectroscopic ellipsometry," *Nano Letters*, null, Jul. 2020, ISSN: 1530-6984. DOI: 10.1021/acs.nanolett.0c01963 (cited on pages 32, 35, 93, 113, 114, 116, 117).

[61] F. Würthner, T. E. Kaiser, and C. R. Saha-Möller, "J-aggregates: From serendipitous discovery to supramolecular engineering of functional dye materials," *Angewandte Chemie - International Edition*, volume 50, pages 3376–3410, 15 2011, ISSN: 14337851. DOI: 10.1002/anie.201002307 (cited on page 34).

[62] A. E. Schlather, N. Large, A. S. Urban, P. Nordlander, and N. J. Halas, "Near-field mediated plexcitonic coupling and giant rabi splitting in individual metallic dimers," *Nano Letters*, volume 13, pages 3281–3286, 7 2013, ISSN: 15306984. DOI: 10.1021/nl4014887 (cited on page 34).

[63] E. Eizner, O. Avayu, R. Ditcovski, and T. Ellenbogen, "Aluminum nanoantenna complexes for strong coupling between excitons and localized surface plasmons," *Nano Letters*, volume 15, pages 6215–6221, 9 2015, ISSN: 15306992. DOI: 10.1021/acs.nanolett.5b02584 (cited on page 34).

[64] K. Zhang, T.-Y. Chen, W.-B. Shi, C.-Y. Li, R.-H. Fan, Q.-J. Wang, R.-W. Peng, and M. Wang, "Polarization-dependent strong coupling between surface plasmon polaritons and excitons in an organic-dye-doped nanostructure," *Optics Letters*, volume 42, pages 2834–2837, 14 Jul. 2017, ISSN: 0146-9592. DOI: 10.1364/ol.42.002834 (cited on page 34).

[65] P. Vasa, R. Pomraenke, G. Cirmi, E. D. Re, W. Wang, S. Schwieger, D. Leipold, E. Runge, G. Cerullo, and C. Lienau, "Ultrafast manipulation of strong coupling in metal-molecular aggregate hybrid nanostructures," *ACS Nano*, volume 4, pages 7559–7565, 12 December 2010, ISSN: 19360851. DOI: 10.1021/nn101973p (cited on page 34).

[66] S. Baieva, O. Hakamaa, G. Groenhof, T. T. Heikkila, and J. J. Toppari, "Dynamics of strongly coupled modes between surface plasmon polaritons and photoactive

molecules: The effect of the stokes shift," *ACS Photonics*, volume 4, pages 28–37, 1 2017, ISSN: 23304022. DOI: 10.1021/acsphotonics.6b00482 (cited on page 34).

[67] M. E. Sasin, R. P. Seisyan, M. A. Kalitteevski, S. Brand, R. A. Abram, J. M. Chamberlain, A. Y. Egorov, A. P. Vasil'Ev, V. S. Mikhrin, and A. V. Kavokin, "Tamm plasmon polaritons: Slow and spatially compact light," *Applied Physics Letters*, volume 92, page 251 112, 25 2008, ISSN: 00036951. DOI: 10.1063/1.2952486 (cited on pages 35, 104).

[68] M. E. Sasin, R. P. Seisyan, M. A. Kaliteevski, S. Brand, R. A. Abram, J. M. Chamberlain, I. V. Iorsh, I. A. Shelykh, A. Y. Egorov, A. P. Vasil'ev, V. S. Mikhrin, and A. V. Kavokin, "Tamm plasmon-polaritons: First experimental observation," *Superlattices and Microstructures*, volume 47, pages 44–49, 1 2010, ISSN: 07496036. DOI: 10.1016/j.spmi.2009.09.003.

[69] A. Kumari, S. Kumar, M. K. Shukla, G. Kumar, P. S. Maji, R. Vijaya, and R. Das, "Coupling to Tamm-plasmon-polaritons: Dependence on structural parameters," *Journal of Physics D: Applied Physics*, volume 51, page 255 103, 25 2018, ISSN: 13616463. DOI: 10.1088/1361-6463/aac474 (cited on page 35).

[70] B. Auguié, A. Bruchhausen, and A. Fainstein, "Critical coupling to Tamm plasmons," *Journal of Optics*, volume 17, page 35 003, 3 February 2015, ISSN: 20408986. DOI: 10.1088/2040-8978/17/3/035003 (cited on pages 35, 36).

[71] K. M. Morozov, A. V. Belonovskii, E. I. Girshova, K. A. Ivanov, and M. A. Kaliteevski, "Properties of a tamm-plasmon-based microcavity with metal intracavity layers and an organic active region," *Semiconductors*, volume 54, pages 350–354, 3 March 2020, ISSN: 10906479. DOI: 10.1134/S106378262003015X (cited on page 37).

[72] S. Divitt. (2017). "Jreftran - a layered thin film transmission and reflection coefficient calculator." version Retrieved August 3, 2017, [Online]. Available: https://www.mathworks.com/matlabcentral/fileexchange/50923-jreftran-a-

layered-thin-film-transmission-and-reflection-coefficient-calculator (cited on page 39).

[73] I. L. Geada, H. Ramezani-Dakhel, T. Jamil, M. Sulpizi, and H. Heinz, "Insight into induced charges at metal surfaces and biointerfaces using a polarizable Lennard-Jones potential," *Nature Communications*, volume 9, 1 December 2018, ISSN: 20411723. DOI: 10.1038/s41467-018-03137-8 (cited on page 44).

[74] L. V. R.-d. Marcos, J. I. Larruquert, J. A. Mendez, and J. A. Aznarez, "Self-consistent optical constants of SiO2 and Ta2O5 films," *Opt. Mater. Express*, volume 6, number 11, pages 3622–3637, November 2016. DOI: 10.1364/OME.6.003622 (cited on pages 57, 98).

[75] T. Siefke, S. Kroker, K. Pfeiffer, O. Puffky, K. Dietrich, D. Franta, I. Ohlídal, A. Szeghalmi, E.-B. Kley, and A. Tünnermann, "Materials pushing the application limits of wire grid polarizers further into the deep ultraviolet spectral range," *Advanced Optical Materials*, volume 4, number 11, pages 1780–1786, 2016. DOI: 10.1002/adom.201600250 (cited on pages 57, 98).

[76] M. Larkowska, M. Wuebbenhorst, and S. Kucharski, "Spirooxazine photoisomerization and relaxation in polymer matrices," *International Journal of Polymer Science*, volume 2011, pages 1–6, 2011, ISSN: 1687-9422. DOI: 10.1155/2011/627195 (cited on page 77).

[77] S. Kucharski and E. Ortyl, "Refractive index modulation in the films containing single and dual chromophore system," pages 555–560, 7-8 2006. DOI: 10.14314/polimery.2006.555 (cited on page 77).

[78] P. Uznanski, C. Amiens, B. Donnadieu, Y. Coppel, and B. Chaudret, "Oxidation of photochromic spirooxazines by coinage metal cations. part i. reaction with AgNO3: Formation and characterisation of silver particles," *New Journal of Chemistry*, volume 25, pages 1486–1494, 12 2001, ISSN: 11440546. DOI: 10.1039/b105446p (cited on page 77).

[79] N. Berova, L. D. Bari, and G. Pescitelli, "Application of electronic circular dichroism in configurational and conformational analysis of organic compounds," *Chemical Society Reviews*, volume 36, pages 914–931, 6 2007, ISSN: 03060012. DOI: 10.1039/b515476f (cited on page 81).

[80] G. L. Eakins, M. W. Cooper, N. N. Gerasimchuk, T. J. Phillips, B. E. Breyfogle, and C. J. Stearman, "Structural influences impacting the role of the 9-ylidene bond in the electronic tuning of structures built upon 9-fluorenylidene scaffolds," *Canadian Journal of Chemistry*, volume 91, pages 1059–1071, 11 2013, ISSN: 0008-4042. DOI: 10.1139/cjc-2013-0074 (cited on page 81).

[81] J. Bonefacino, M.-L. V. Tse, C.-F. J. Pun, X. Cheng, W. K. E. Chan, A. Boersma, and H.-Y. Tam, "Characterization of spirooxazine and spiropyran hosted in poly(methyl methacrylate) for germicidal uv source indicator application," *Optics and Photonics Journal*, volume 03, pages 11–16, 07 2013, ISSN: 2160-8881. DOI: 10.4236/opj.2013.37A002 (cited on page 91).

[82] S. Rudin and T. L. Reinecke, "Oscillator model for vacuum Rabi splitting in microcavities," *Physical Review B - Condensed Matter and Materials Physics*, volume 59, pages 10 227–10 233, 15 1999, ISSN: 1550235X. DOI: 10.1103/PhysRevB.59.10227 (cited on page 92).

[83] J. P. Reithmaier, "Strong exciton-photon coupling in semiconductor quantum dot systems," *Semiconductor Science and Technology*, volume 23, 12 2008, ISSN: 02681242. DOI: 10.1088/0268-1242/23/12/123001 (cited on page 92).

[84] D. Bléger and S. Hecht, "Visible-light-activated molecular switches," *Angewandte Chemie - International Edition*, volume 54, pages 11 338–11 349, 39 2015, ISSN: 15213773. DOI: 10.1002/anie.201500628 (cited on page 96).

[85] A. Golombek, M. Balasubrahmaniyam, M. Kaeek, K. Hadar, and T. Schwartz, "Collective Rayleigh scattering from molecular ensembles under strong coupling," *Journal of Physical Chemistry Letters*, volume 11, pages 3803–3808, 10 May 2020, ISSN: 19487185. DOI: 10.1021/acs.jpclett.0c01012 (cited on page 104).

[86] C. Symonds, A. Lemàtre, E. Homeyer, J. C. Plenet, and J. Bellessa, "Emission of Tamm plasmon/exciton polaritons," *Applied Physics Letters*, volume 95, page 151 114, 15 2009, ISSN: 00036951. DOI: 10.1063/1.3251073 (cited on page 104).

[87] H. Bahsoun, T. Chervy, A. Thomas, K. Börjesson, M. Hertzog, J. George, E. Devaux, C. Genet, J. A. Hutchison, and T. W. Ebbesen, "Electronic light-matter strong coupling in nanofluidic Fabry-Pérot cavities," *ACS Photonics*, volume 5, pages 225–232, 1 January 2018, ISSN: 23304022. DOI: 10.1021/acsphotonics.7b00679 (cited on page 106).

[88] C. Tserkezis, A. I. Fernandez-Dominguez, P. A. D. Gonçalves, F. Todisco, J. D. Cox, K. Busch, N. Stenger, S. I. Bozhevolnyi, N. A. Mortensen, and C. Wolff, "On the applicability of quantum-optical concepts in strong-coupling nanophotonics," *Reports on Progress in Physics*, volume 83, number 8, page 082 401, Jul. 2020, ISSN: 0034-4885. DOI: 10.1088/1361-6633/aba348 (cited on pages 106–110).

[89] H. Wang, H. Y. Wang, H. B. Sun, A. Cerea, A. Toma, F. D. Angelis, X. Jin, L. Razzari, D. Cojoc, D. Catone, F. Huang, and R. P. Zaccaria, "Dynamics of strongly coupled hybrid states by transient absorption spectroscopy," *Advanced Functional Materials*, volume 28, page 1 801 761, 48 November 2018, ISSN: 16163028. DOI: 10.1002/adfm.201801761 (cited on page 106).

[90] T. W. Ebbesen, "Hybrid light-matter states in a molecular and material science perspective," *Accounts of Chemical Research*, volume 49, pages 2403–2412, 11 November 2016, ISSN: 15204898. DOI: 10.1021/acs.accounts.6b00295 (cited on page 106).

[91] A. González-Tudela, P. A. Huidobro, L. Martín-Moreno, C. Tejedor, and F. J. García-Vidal, "Theory of strong coupling between quantum emitters and propagating surface plasmons," *Physical Review Letters*, volume 110, page 126 801, 12 March 2013, ISSN: 00319007. DOI: 10.1103/PhysRevLett.110.126801 (cited on pages 110, 112).

[92] ——, "Supplementary material: Theory of the strong coupling between quantum emitters and propagating surface plasmons," *Physical Review Letters*, volume 110, page 126 801, 12 March 2013, ISSN: 00319007. DOI: 10.1103/PhysRevLett.110.126801 (cited on pages 110, 112).

[93] D. N. Basov, M. M. Fogler, and F. J. G. de Abajo, "Polaritons in van der Waals materials," *Science*, volume 354, aag19921–aag19928, 6309 October 2016, ISSN: 0036-8075. DOI: 10.1126/science.aag1992 (cited on page 120).

Acknowledgements

I would like to give many thanks to my Doktorvater, Prof. Franz Faupel, first of all for giving me the opportunity to work and study in his group. He always supported me by opening doors to opportunities to pursue not only research but also my passion for teaching, for example, in Solid State Physics exercise classes and asking me to fill in for him in the lecture during his occasional absence. He let me participate and profit from his interesting professional network of international scientists and good reputation. Many thanks to you, Franz.

To Prof. Mady Elbahri goes thanks for kicking off the project involving light-matter interactions many years ago, which paved the road for my involvement in an area of scientific inquiry where my passion and interests lie: the science of light. In addition, he lifted a paper co-written by me to new levels and through his graft to a wider scientific view improved its reach. Many thanks.

The work in this thesis was performed as part of the Collaborative Research Center 677, Function by Switching, in project C01, funded by the German Research Foundation (auf Deutsch: Sonderforschungsbereich 677, Funktion durch Schalten, Projekt C01, Förderung durch die Deutsche Forschungsgemeinschaft), and thanks goes to them for funding this project.

To Ron-Marco Friedrich, whose coding skills approach “native speaker” talents, goes thanks for training me in the ways of MATLAB and his incisive approach to scientific inquiry. Through discussions scientific and otherwise, I gained a loyal friend and got to know a curious-minded individual, a mindset we share. True friendship is rare. Thank you.

I am grateful to have worked with Prof. Klaus Rätzke, whose help and guidance

in improving my academic writing skills and scientific approach came from a place of knowledge and experience and with a large and welcome dose of humor. Thanks for your brain-challenging and heart-lifting support, Klaus.

Thanks go to Dipl.-Ing. Stefan Rehders, whose great technical skills and thorough knowledge in engineering made my experiments even possible, whose assistance was there at all times when I needed it. Thanks also for your caring and kind words, and shared laughter.

To Salih Veziroglu goes a debt of gratitude for helping me with technical drawings, for always having a friendly face, and for all your patience in our office. Thanks, Salih.

I thank Dr. Thomas Strunskus not only for his professional opinion in chemistry questions and his navigational talents in administrative questions, but also his light-hearted sense of humor.

To Malte Großmann, I send a friendly thanks for literature suggestions, scientific discussions at many a CRC meeting, and showing me his very interesting research into surface plasmon polaritons. Thanks for that, Malte.

In addition, I want to thank Prof. Michael Bauer of the Department of Physics at Kiel University for his critical reading of and feedback on a scientific paper, for allowing me to see the very interesting research work going on in his group, and for discussions at CRC events.

And to Prof. Cenk Aktas, I want to pay my thanks for his scientific advice, his positivity, his light-hearted attitude, and his friendly office humor. Thank you, Cenk, for the many discussions.

And to the rest of the Faupel group, especially Sieglinde Kastaun, the CRC members and anyone who I may have forgotten, thank you very much for your camaraderie and help in science and this adventure.

To my family and friends, thank you for the encouragement, words of wisdom, and support.

And to my parents who have given me unconditional love, a wonderful childhood, steadfast values, and an appreciation for knowledge, hard work, and education, I give

thanks and love for the direction you set me off on in life. What I owe you is beyond evaluation.

And to my loving husband, I want to give my greatest thanks. You have stood by me in all manner, with steady support, resourcefulness, grace and love. It was my dream to study again, and only with you was it possible. Thank you for everything. Mer.

E F A K U L T
S-UNIVERSITÄT ZU K
T K I E L